UNIVERSITA' DEGLI STUDI DI PAVIA

FACOLTA' DI INGEGNERIA
DIPARTIMENTO DI INGEGNERIA INDUSTRIALE E DELL'INFORMAZIONE

DOTTORATO DI RICERCA IN BIOINGEGNERIA E BIOINFORMATICA
XXXI CICLO - 2018

DYNAMIC ENERGY BUDGET BASED MODELS OF TUMOR-IN-HOST GROWTH INHIBITION AND CACHEXIA ONSET IN PRE-CLINICAL SETTING

PhD Thesis by

ELENA MARIA TOSCA

Advisor:
Prof. Paolo Magni

PhD Program Chair:
Prof. Riccardo Bellazzi

Gutta cavat lapidem
non vi sed saepe cadendo

To my parents

Abstract (English)

The anticancer drug development process is characterized by the highest attrition rates in the clinical setting, primarily due to adverse efficacy and safety results. Preclinical animal models, characterized by a questionable predictive value of the effects to be expected in human patients, and an inadequate predictive paradigm of preclinical to clinical translation, lacking of quantitative reasoning, may be likely causes of this. Pharmacometric models, able to extract, synthesize and quantitatively integrate preclinical information, could support the transfer of the preclinical results to the clinical setting.

Within the paradigm of the Model-Informed Drug Discovery and Development (a quantitative framework for prediction and extrapolation focused on knowledge and inference generated from integrated models of candidate drugs, mechanism and disease level data and aimed at improving the quality, efficiency and cost effectiveness of decision-making), my thesis deals with the development, implementation and analysis of new mathematical modeling approaches to exploit data routinely generated in the preclinical phases of anticancer drug development process. In all the described research activities it can be recognized the importance of PK/PD modeling in better charac-

terizing, understanding and predicting PK/PD behaviour of oncology agents.

The focus of this work is a mathematical modeling of interactions between tumor and host organism during anticancer drug treatments in preclinical experiments. To this aim, a tumor-in-host modeling approach is proposed on the basis of a set of tumor-host interaction rules taken from the Dynamic Energy Budget (DEB) theory. This approach, suitably adapted to several experimental contexts, is able to integrate the different aspects characterizing the *in vivo* tumor growth studies: the drug cytotoxic or cytostatic activity on the tumor, the potentially onset of cachexia due to the treatment, the effect of the tumor on the host (cancer-related cachexia and/or anorexia) and, viceversa, the influence of the host condition on tumor dynamics.

In particular, a tumor-in-host DEB-based model describing the cachexia onset and tumor growth inhibition (TGI) after the administration of cell-killing agents to laboratory animals has been developed, mathematically analysed and, subsequently, applied on a etoposide experiment in Wistar rats. The cytostatic anticancer effect of angiogenesis inhibitors in xenograft mice has also been modeled within the tumor-in-host DEB-based framework. This DEB-TGI anti-angiogenic model has proved to be extremely useful to describe and understand the complexities of an hypoxia-triggered resistance to bevacizumab. Finally, starting from the previous developed TGI models, a tumor-in-host approach to analyse combination experiments and assess possible drug-drug interaction between anti-angiogenic and chemotherapeutic agents is proposed.

Abstract (Italian)

Il processo di sviluppo di un nuovo farmaco oncologico é caratterizzato da un elevatissimo numero di fallimenti, principalmente dovuti alla scarsa efficacia o eccessiva tossicitá riscontrata durante le fasi di sperimentazione clinica. Tra le possibili cause di questo fenomeno vi sono l'utilizzo di modelli animali poco rappresentativi delle condizioni osservabili in soggetti oncologici e la mancanza di un paradigma di traslazione dal contesto preclinico a quello clinico sufficientemente predittivo. L'utilizzo di modelli farmacometrici, capaci di estrapolare, sintetizzare e integrare quantitativamente le informazioni raccolte durante la sperimentazione preclinica, puó essere un promettente tentativo di rispondere a queste problematiche.

Inserendosi nell'ambito dell'uso della modellistica matematica a supporto del processo di sviluppo di nuovi farmaci antitumorali, questa tesi si concentra sulla costruzione, implementazione ed analisi di nuovi approcci matematici per l'analisi di dati sperimentali tradizionalmente ottenuti durante le fasi di sviluppo preclinico.

Focus specifico di questo lavoro é la modellizzazione delle interazioni tra tumore e organismo ospitante durante la somministrazione di trattamenti antitumorali resa possibile dall'utilizzo di un set di leggi di

bilancio energetico fornite dalla Dynamic Energy Budget (DEB) theory. L'approccio proposto, opportunatamente declinato in diversi contesti sperimetali, é capace di tenere simultaneamente in considerazione i differenti aspetti che caratterizzano gli studi di crescita tumorale *in vivo*: l'effetto citotossico o citostatico della terapia antitumorale sulle cellule tumorali, l'eventuale insorgere di fenomeni di cachexia come conseguenza del trattamento o del tumore stesso infine, l'influenza che la condizione dell'organismo ha sulla crescita tumorale.

Piú nel dettaglio, é stato sviluppato ed analizzato dal punto di vista matematico un modello di interazione tumore-organismo capace di descrivere sia l'effetto inibitorio sulla crescita tumorale di un trattamento citotossico, sia il suo effetto tossico sull'organismo ospitante. Tale modello é stato, in particolare, adottato per analizzare dati sperimentali circa l'effetto del farmaco etoposide su ratti Wistar. É stato inoltre sviluppato un secondo modello, sempre basato sulle interazioni energetiche di tumore e orgamismo, per descrivere l'effetto citostatico di un trattamento anti-angiogenico. L'approccio meccanicistico alla base del modello proposto ha permesso di tenere in considerazioni l'insorgere di fenomeni di resistenza mediata dalla condizione di ipossia tumorale in seguito a trattamenti prolungati di bevacizumab. Infine, utilizzando i modelli di inibizione di crescita tumorale precedentemente sviluppati, é stato proposto un nuovo approccio per analizzare esperimenti di combinazione e riconoscere eventuali interazioni tra farmaci anti-angiogenici e chemioterapici.

List of Abbreviations

ADME Absorption, Distribution, Metabolism, Excretion

AIC Akaike's Information Criterion

AUC Area Under the Curve

BIC Bayesian Information Criterion

BQL Below the Quantification Limit

BVZ Bevacizumab

BWL Body Weight Loss

CV Coefficient of Variation

DEB Dynamic Energy Budget

DDMoRe Drug Disease Model Resources

EGF Epidermal Growth Factor

EGFR Epidermal Growth Factor Receptor

EMA European Medicines Agency

EFPIA European Federation of Pharmaceutical Industries and Associations

ECACC European Collection of Cell Cultures

ER Extended Release

FDA Food and Drug Administration

FIH First-In-Human

GOF Goodness Of Fit

IMI Innovative Medicines Initiative

i.p. Intra-Peritoneal

i.v. Intravenous

IVIVC In Vivo - In Vitro Correlation

IVIVC P-ring IVIVC Progesterone ring

MID3 Model-Informed Drug Discovery and Development

M&S Modeling and Simulation

NLME Non Liner Mixef Effect

NME New Molecular Entitities

NMS Nerviano Medical Sciences

npde Normalised Prediction Distribution Errors

ODE Ordinary Differential Equation

o.s. Orally

PD Pharmacodynamic

PE Prediction Errors

PK Pharmacokinetic

PLK1 Polo-Like Kinase 1

PTGCs Predicted Tumor Growth Curves

PVRs Progesterone Vaginal Rings

R&D Research and Development

s.c. subcutaneously

TGD Tumor Growth Delay

TGI Tumor Growth Inhibition

VEGF Vascular Endothelial Growth Factor

VPC Visual Predictive Check

W256 Walker-256

Contents

List of Figures

List of Tables

Chapter 1

Introduction

In the past decades, the pharmaceutical industry has seen the increasing application of Modeling and Simulation (M&S) in the drug Research and Development (R&D) process. This shift from empiric to Model-Informed Drug Discovery and Development (MID3) has received also the support of the regulatory authorities that identified the adoption of mathematical and statical approaches as a strategic solution to the productivity crisis of the pharmaceutical R&D [1, 2].

Indeed, developing and bringing a new drug to the market is an extremely long and expensive process, characterized by high attrition rates. The reasons why drug compounds undergo attrition have changed over time [3, 4]. Even if, in the early ninety, adverse Pharmacokinetic (PK) and bioavailability results were the most relevant causes of drug failures, from 2000 the impact of these factors had significantly reduced shifting the temporal attrition profiles to the later clinical stages. Nowadays, the high failure rates are primarily due to inadequate efficacy and/or safety in phases II and III, and this is the most important determinant of overall drug development cost [5, 6, 7, 8]. Interestingly, a significant cost reduction (even larger than

50%) could be achieved by a shift in attrition from Phase III to Phase II [9]. In particular, lack of efficacy contributes more significantly into these therapeutic area, as oncology, in which preclinical animal models seem to be less efficient of predicting what happen in human patients. This finding demonstrates the need to develop a more predictive paradigm of preclinical to clinical translation [3].

This thesis deals with the development and application of a new modeling approach for better exploiting data routinely generated in the preclinical phase of anticancer drug development process. In particular, different mathematical models that, based to the Dynamic Energy Budget (DEB) theory, are able to describe and predict the inhibition of the tumor-in-host growth and the cachexia onset are presented here and evaluated on experimental data of xenograft rodents.

1.1 Drug Discovery and Development

Drug research and development is a long, complicated and expensive process, that is aimed at taking the path from understanding a disease to bringing a safe and effective new treatment to patients. Each drug has to be effective in achieving the defined therapeutic target as well as appropriately described in terms of side effects, dosage form, facility of administration and costs. Recent studies report that the cost of bringing a new drug to the market exceeds $2500 million [10] with an average duration of about 13 years [3]. Therefore, pharmaceutical companies are continuously involved in the optimization of this process, predicting in advance compounds with high probability of failure, while making the development of the most promising candidate drugs faster and more effective.

As shown in Fig. 1.1, the drug development process, from basic discovery to commercialization, can be divided in several phases [11].

The discovery phase is composed by different steps. After a suf-

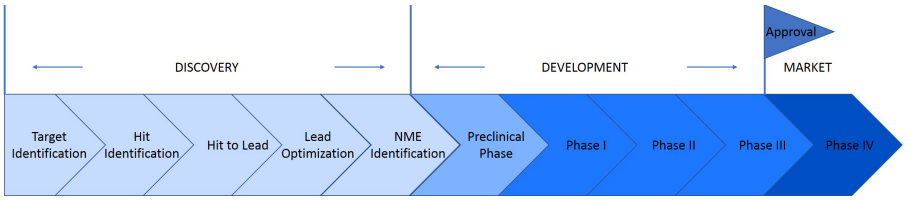

Figure 1.1: Drug discovery and development process.

ficient understanding of the considered disease and of the causes underlying the pathological condition, a molecular target (receptor, enzyme, protein or hormone) which is biomedical relevant, i.e. associated with a therapeutic response, is identified and selected (Target identification). Molecules showing affinity for the target, called hits, are searched within a huge number of compounds, both collected in commercially available chemical libraries or synthesized by the drug companies themselves. The aim is to find a few promising molecules (hits), that, acting on the selected target, may alter the disease progression and become a drug. Preliminary test are performed in living cells or via computational models to assess Absorption, Distribution, Metabolism, Excretion (ADME) and toxicological properties of each hit (Hit to Lead). The leads that survive the initial screening are, then, optimized or structurally modified to make them more effective and safe (Lead optimization). Identified one or more optimized compounds, further *in vitro* and *in vivo* tests are carried out to assess pharmaceutical and PK properties, such as solubility, permeability, metabolic stability and affinity for plasma proteins.

Optimized leads, having all the appropriate required properties on the basis of *in vitro* and/or *in silico* assays (New Molecular Entities (NME)), are, then, evaluated *in vivo* in relevant animal models for a formal characterization of the pharmaco-toxicological profiles preceding the clinical phase (Preclinical Phase). These compounds are administered to a small number of animals (usually rodents and/or

other animal species, like dogs and rabbits) to assess their *in vivo* PK, Pharmacodynamic (PD) and safety and to identify the conditions (in terms of exposure and duration of the exposure), that achieve the best compromise between pharmacological and toxicological effects. The main objective of this research phase is to insure that the subsequent study in humans will be performed without risk for the participants; therefore it is aiming to characterize formally safety and tolerability and their relationship with the systemic exposure to the drug.

The preclinical phase is followed by the clinical development. The First-In-Human (FIH) studies (Phase I) are safety designed (in terms of starting and maximal achievable doses) and a small number of subjects (healthy volunteers or, in cases such as for oncology drugs, patients) are usually enrolled. The objective is the evaluation of the safety, ADME and preliminary PD properties with a particular interest for dose-response or exposure-response relationships in human and, therefore, for the safe dose range. In these studies conducted on patients, also preliminary information about efficay can be gathered. Afterwards, in Phase II trials the candidate drug effectiveness is assessed in about few dozens to few hundreds of patients. Possible short-term side effects and risks associated with the drug are analyzed and the optimal dosing regimens are identified to be tested in the confirmatory Phase III trials. In the last step of the clinical phase, Phase III, the drug candidate is studied in a larger number (from hundreds to thousands) of patients to generate data to demonstrate the superiority of the candidate drug compared to the current standard of care. Additional safety data are collected to allow a better definition of the risk/benefit balance. Variability of the PK can also be studied in the target patient population.

Even after approval and its launch on the market (Phase IV), the research on a new medicine continues and the entire population assuming it is monitored (pharmaco-vigilance) to evaluate the long-term safety and the effectiveness on special subgroups of patients.

As previously described, PK and PK/PD evaluations are performed along the whole drug discovery-development continuum to elicit knowledge on the new drug and streamline its clinical evaluation. The discovered knowledge can be used to synthesize new data or new knowledge, or to supplement existing data in a learn-confirm paradigm [12].

1.2 Modeling and Simulation (M&S) to support drug R&D

Modeling and Simulation (M&S) are widely applied to core business activities across a broad range of industries. Despite a relatively late adoption, the pharmaceutical industry continues to grow its utilization of M&S across a diverse range of applications. The greater spread of M&S led to the M&S joint workshop of the European Medicines Agency (EMA)/ European Federation of Pharmaceutical Industries and Associations (EFPIA) that, in 2011, assembled scientists from the pharmaceutical industry, academia and regulatory authorities to consider the (then) current and future role of M&S in drug development and regulatory assessment [2, 13, 14, 15, 16]. On that occasion, the term Model Informed Drug Discovery and Development (MID3) has been introduced to define a "quantitative framework for prediction and extrapolation, centered on knowledge and inference generated from integrated models of compound, mechanism and disease level data and aimed at improving the quality, efficiency and cost effectiveness of decision making".

The concepts underpin MID3 are not new. In the 1992, Peck et al. stressed the importance of integrating PK, PD and toxicokinetic principles in drug development [17]. Afterwards, in the 1997, Sheiner introducing the learn-confirm paradigm, emphasized the importance of adopting model-based methods [18].

The need for MID3 application has been popularized by industry analysts and well recognized by many others as a solution to the productivity decline [19, 20, 11, 21]. In addition, these approaches were identified as a strategic component for the Critical Path Initiative of the Food and Drug Administration (FDA) [1] and the current Innovative Medicines Initiative (IMI), particularly the Drug Disease Model Resources (DDMoRe). Moreover, various summaries have confirmed the MID3 value to improve R&D efficiency reducing the budget for the experimental trials and increasing the success rates [22, 23, 24, 25].

MID3 covers the whole spectrum of the drug development process viewed as an iteration of learning and confirming activities [18] that contribute to increase the knowledge of the NME, the biological systems, the targeted medical indication, as well as molecules within a therapeutic class [20]. This learn-confirm paradigm is the central tenet of the MID3 approach that can be summarized into the following steps: knowledge gathering, model construction and simulation (Fig. 1.2). The first one is the collection of all the available information: assumptions, prior information and experimental data obtained from biology, toxicology, ADME and efficacy studies. Starting from the available knowledge, models are built and validated with the aim of capturing the causal relationship between disease state, prognostic factors, drug characteristics, safety and efficacy outcomes from virtual studies. Finally, the developed models can be used to simulate outcomes helping to answer questions about dose selection and study design and to represent dose-response and time-response behaviour. It is implicit that this quantitative framework is iterative in nature: inconsistencies between predictions and subsequent observations trigger further model development or assumption refinement and, potentially, new studies to be designed and performed; any new modification introduced into the framework can be, then, evaluated, "confirmed", or at least assessed in terms of their impact on the resultant inferences.

The value of MID3 approaches in enabling model-informed decision-

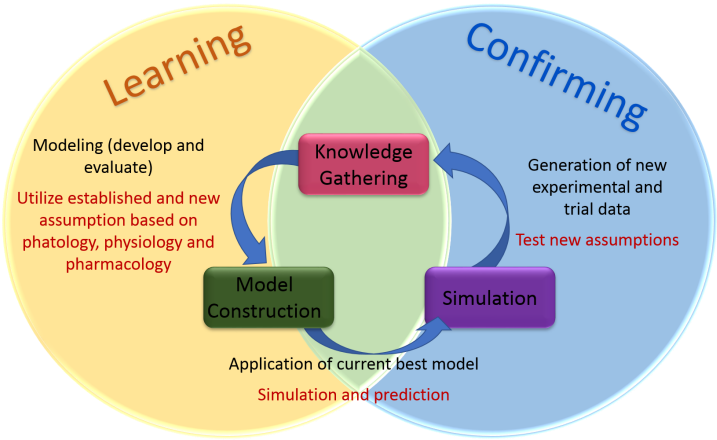

Figure 1.2: Model-Informed Drug Discovery and Development (MID3) paradigm.

making is evidenced by the variety of application across drug discovery, development, commercialization, and life-cycle management.

In the early discovery, MID3 can contribute to the target identification and validation through *in silico* approaches that integrate experimental data from multiple sources, increasing, thus, the confidence in the role of the target in the disease or in the mechanistic understanding of target modulation.

Model-informed approaches can enable the quantitative assessment of PK, desired (PD) and undesired (safety) effects of novel compounds to support the preclinical selection of drug candidates for the subsequent clinical development based on increased confidence in the projected efficacious dose and regimen before the FIH dose.

In the characterization and prediction of human ADME and PK variability multiple modeling approaches can be applied. These methods help to identify significant covariates that determine expected exposure and the possible need for dose adjustment in specific subpopulations. Further, the use of In Vivo - In Vitro Correlation (IVIVC)

models can avoid bioequivalence studies in specific situations defined in the FDA guidelines for scale-up and post-approval changes (see Appendix A for an example of IVIVC model).

Model-informed study design optimization is, also, applicable to increase the efficiency and reduce costs of trials during different phases of drug discovery and development.

Characterization of benefit and risk is an ongoing process that occurs all along the compound development path. MID3 approaches can be used to predict clinical outcome measures based on modeling of preclinical and early clinical data, to optimize a dosing strategy, estimate a therapeutic window by integrating related safety and efficacy endpoints, provide de-risking alternative development approaches, and support the selection of optimal candidate compounds.

Further relevant applications concern the selection of appropriate doses and schedules which provide optimal treatment benefit for the majority of patients during the later clinical trials, as well as the definition of label recommendations including the cases of drug combinations and special population (e.g., pedriatic, renally or hepatically impaired, elderly, obese, subgroups) during the approval phase.

In summary, the wide variety of the previously presented applications exemplifies how MID3 can be applied across R&D to increase the confidence in the compound, mechanism or disease rationales; provide support to internal go/no-go decisions, dose finding, dose adjustments for patient subgroups; support labelling, benefit-risk, and increasing confidence in next-stage investment.

1.3 MID3 applied to oncology

Over the past decade, a large number of novel anticancer drugs have been developed and many are now used into routine clinical practice. However, the discovery of new anticancer drugs remains a highly

challenging endeavour. The attrition rates clearly reflect the level of loss of candidate drugs during their preclinical and clinical development: less than 5% of NME evaluated in FIH studies are able to enter the market [3]. The likelihood of approval for oncology drugs is lower than for those in any other disease area [8]. Numerous solutions have been proposed to tackle the issue of attrition in the oncology field by many authors; one of these consists in the optimization of the *in vivo* preclinical experiments performed to select promising compounds based on a suitable antitumor activity and a manageable tolerability profile and to anticipate with good accuracy the systemic exposure or the dose that will provide initial signs of efficacy [26, 27].

1.3.1 *In Vivo* Tumor Growth Experiments: the xenograft models

The development of murine models for human cancer studies dates back to the late 1940s [28]. These animal models are used both to investigate factors involved in tumor transformation, invasion and metastasis, and to examine response to anticancer therapy. Xenografts of human tumors are the most popular preclinical models used to evaluate the anticancer activity of new compounds [29, 30, 31, 32]. Despite discussions about their predictive power for the actual human response to the treatment [30, 27], xenograft models still play a major role in cancer drug development due to their high ability in predicting clinical efficacy combined with relative easy and low cost implementation [33, 34].

During these experiments, fragments of about 20-30 mg of tumor, coming from human cell lines, are implanted subcutaneously (s.c.) in immunodeficient rodents (mice or rats). When the animals show a palpable tumor mass of approximately 100-200 mm^3 (in general one week after the inoculation), they are selected, randomized and divided

in two or more groups each including several individuals. After the randomization the experiment starts: some groups are treated with a vehicle (control groups), others with anticancer compounds (treated groups) following predefined protocols. All the animals (controls and treateds) are usually clinically evaluated daily and weighted usually twice a week. Tumor dimensions (length and width (mm)) are measured by calliper, typically from once a day to every 4 days, and tumor mass (mg) calculated as:

$$weight = \rho_{tr} \frac{length \cdot width^2}{2} \tag{1.1}$$

approximating tumor shape with the ellipsoid generated by the rotation of a semi-ellipse around its larger axis (length) and assuming unit density ($\rho_{tr} = 1\ mg/mm^3$).

Drug administrations can differ for dosages, duration of treatment, schedule (number and time of administrations), way of administration (Intravenous (i.v.) or Intra-Peritoneal (i.p.)) and administration profile (bolus or infusion).

To compare the anticancer activity of different compounds or of different dosages/schedules of the same compound, the distances between the different tumor weight profiles at specific weight (Tumor Growth Delay (TGD)) or time (Tumor Growth Inhibition (TGI)) are measured. Unfortunately, these efficacy metrics can depend on experimental conditions and, thus, a certain number of experiments have to be performed to obtain a valuable estimate of the drug activity. In addition, the extrapolation to human of these results is difficult. For this reason, an approach based on mathematical modeling is necessary to obtain experiment-independent model parameters which can be quantitatively linked with clinically relevant endpoints [33].

1.3.2 Current mathematical models of *in vivo* Tumor Growth Inhibition

Pharmacometric models represent one of the most comprehensive tools for summarizing and integrating information obtained in the often sparse, limited and not-optimally designed experiments performed in the early phases of oncology drug discovery [35]. In particular, several PK-PD models have been proposed to describe TGI observed during xenograft experiments after both single agent and combination therapies. Hereafter, some of the mathematical approaches published in the recent literature are introduced while several reviews are available for a more comprehensive picture on this topic [35, 36, 33, 37, 38, 39].

One of the currently most popular PK-PD TGI models is the model proposed by Simeoni et al., also called cell distribution model [40]. It describes the unperturbed tumor growth in the control group through an exponential phase followed by a linear one. In the perturbed tumor growth model (treated animals), it is assumed that, due to the drug cytotoxic effect, a fraction of cancer cells becomes not-proliferating and enter a transit compartmental system that leads to cell death. Drug activity on tumor growth is proportional to both drug concentration and weight of proliferating cells, via the constant, k_2 that represents the drug antitumor potency. The separation between tumor and drug-related parameters introduced by this model is a likely factor of its success. Moreover, a significant correlation has been found between this potency parameter and the systemic exposures of ten marketed drugs administered in the clinical practice indicating its translational applicability [41].

In some xenograft experiments a further slowdown of tumor growth is observed after the linear phase. In these cases, a more traditional Gompertz model may be more suited for describing the plateau reached by the tumor in the unperturbed group [39]. Another popular model

is the signal distribution model proposed by Lobo et al. [42]. Here, the drug acts on a receptor which initiates a signal transduction cascade whose final product is a modulation of the killing effect against tumor cell. Additional complexities were added to the basic cell or signal distribution models on an ad hoc basis: Stuyckens et al. modified the Simeoni TGI model to account for the development of resistance to antitumor therapy [43]; Pigatto et al. to account for the schedule-dependent effect of etoposide on TGI in rats [44].

Other popular PK-PD models were developed to consider the activity of anti-angiogenic compounds. Hanfeldt et al. adopted a Gomperzt model in which tumor growth is limited by a carrying capacity variable (defined as the maximal sustainable tumor size due to the input of oxygen and nutrients) inhibited by the effect of the anti-angiogenic therapy. The concept of carrying capacity has been employed and modified in many recent papers [45, 46, 47]. In particular, Ribba et al. used four ordinary differential equations to describe the temporal changes of non-hypoxic, hypoxic and necrotic tissues within tumor while the carrying capacity concept was adopted to account for the angiogenesis process [47]. When dealing with anti-angiogenic therapy, another potential alternative is proposed in the work of Rocchetti et al. [48]. Here the exponential+linear tumor growth of the Simeoni model is adopted to describe unperturbed group, while an inhibitory E_{max} function is used to account for the tumoristatic effect of bevacizumab.

Several mathematical models were, also, developed to investigate the effect of combination therapy, a situation that is very common in anticancer treatments. Koch et al. described the antitumor effect of anticancer compounds given alone or in combination in *in vivo* xenograft models [49]. The starting point was the Simeoni TGI model [40] with minor modifications; the combined administration of two anticancer compounds was described through an interaction term that account for the nature of the drug-drug interaction (antagonistic, additive, or synergistic effects). This approach was also used by Li et al.

to model the schedule-dependent interaction of the combined administration of erlotinib and gemcitabine [50].

Always based on the Simeoni TGI model, Rocchetti et al. proposed an additivity model able to predict the TGI followed the administration of anticancer compounds in combination under the assumption of a PD null interaction [51]. When two drugs are given in combination, it is assumed that cells hit by one agent can also be hit by the other one as well, thus, 16 possible states of tumor cells are represented by a 4 x 4 mortality matrix. Then, by comparing the predicted curves with the actual tumor weight data, possible departures from additivity can be ascertained. Starting from this work, Terranova et al. [52] developed a combination model accounting for the drug-drug interactions through an interaction term γ that can be equal to, less than, or greater than 1, respectively, in case of additive, antagonistic, or synergistic combinations.

Further modeling approaches have been proposed to analyse experiments involving combinations of anti-angiogenic and cytotoxic compounds. The Simeoni TGI and Rocchetti TGI models were used to evaluate data from combination experiments in which bevacizumab was given with a Polo-like kinase 1 (PLK1) inhibitor [48]. In this case, a weak antagonistic effect between the two compounds was observed and modeled via an inhibitory function, parametrized with bevacizumab concentration, applied on the potency parameter k_2. In their work [46], Wilson and coworkers analyzed tumor diameters data following the combined administration of the cytotoxic agent irinotecan and the anti-angiogenic compound sunitinib using a model based on the carrying capacity concept. The authors concluded that the two drugs showed a weak synergism.

The approaches presented in the previous paragraphs underline the paramount importance of mathematical models in summarizing and integrating the diverse and often sparse observations collected in the typically xenograft experiments that are performed to characterize

anticancer compounds. They can provide objective and quantitative criteria for ranking candidate drugs and, when properly qualified, can also be efficiently used to predict, via simulations, the outcome of conditions not experimentally tested. Eventually, modeling approaches enable the extrapolation from preclinical to human setting that, differently, may be difficult or unsuccessful. Indeed, simple metrics of activity (e.g. *in vivo* percentage of TGI) are too much linked to the specific experimental conditions to be extended and translated directly to the clinics. Only experiment-invariant parameters, derived from models characterized by some mechanistic grounds (that allow the definition of drug-related and system-related parameters) and able to describe in quantitative manner uncertainty and inter-subject variability, have the best chances to be applicable in a translational exercise. However, some issues and gaps are still present in the modeling framework of tumor growth inhibition and need some further considerations.

All the TGI model currently reported in literature described tumor as an independent entity that does not interact with the host organism. Actually, host features, such as cell proliferation rates, caloric intake, metabolism and energetic conditions, significantly influence tumor growth [53]. At the same time, tumor growth can have relevant implications for host physiology. In particular, severe loss of body weight (cachexia) and reduced food intake (anorexia) frequently affect tumor bearing animals during tumor progression [54, 55, 56, 57]. Moreover, cachexia and anorexia are common sides effect of many type of anticancer agents already observable during preclinical xenograft studies. Despite this, mathematical models able to describe the physiological interactions between the tumor and the body host (tumor-in-host models) generally do not foresee the action of anticancer treatments on the tumor, and this appears too complex to be directly applied in the preclinical setting [58, 59].

The lack of an adequate mathematical framework accounting for both the tumor-host interactions and the PD effects of anticancer

therapy leads to relevant consequences. On one side, even if significant Body Weight Loss (BWL) is reported as a sensitive endpoint for xenograft experiments [60], the impact of cachexia mediated by tumor and/or drug treatment is usually assessed only by visual inspection of body weight curves in control and treated animals. This limits the possibility to deeper investigate and separate cancer anorexia-cachexia from the possible effects and complications of anticancer therapy on the host body weights [56]. On the other side, mathematical approaches, that neglect the mutual influence between tumor and host, may provide bias interpretation of TGI, not disentangling and integrating all the factor that affected tumor dynamics.

Thus, the mathematical modeling of tumor and host interactions and of the consequent cachexia onset during an anticancer drug treatment is still one of the open issues of the MID3 in the oncology preclinical setting.

1.4 Thesis Overview

Following the above considerations, the aim of this thesis is to investigate the potential MID3 applications of a tumor-in-host approach in the preclinical oncology R&D. This investigation, starting from the work of Van Leeuwen et al. [58, 59], adopts the Dynamic Energy Budget (DEB) theory as general framework to describe the host physiology. Different PK-PD models describing the tumor-in-host growth inhibition and cachexia onset observed in different preclinical xenograft experiments have been developed and are, here, presented as follows.

In Chapter 2, a DEB-TGI model able to describe the tumor and host body weight dynamics followed cytotoxic anticancer treatment in xenograft mice is introduced and mathematically analyzed. Model assumptions and some biologically relevant considerations derived from the mathematical analysis are widely discussed.

In Chapter 3, the tumor-in-host growth inhibition model, previously developed for mice xenograft experiments, is adapted and applied to evaluate the etoposide effect on Wistar rats. Model structure has been selected and assessed through a naÃ¯ve average data approach, then, a population model has been developed on individual data through a non-linear mixed effect (NLME) approach. Due to the unusually reach experimental design and the availability of information about etoposide intra-tumoral concentration, the model capabilities in describing and distinguishing all the factors characterizing the *in vivo* tumor studies are investigated and exploited.

In Chapter 4, a DEB-TGI model accounting for the cytostatic effect of anti-angiogenic therapy is proposed and evaluated on xenograft mice experiments involving two marketed compounds (bevacizumab and cetuximab) and several tumor cell lines. Furthermore, to account for the decrease of bevacizumab efficacy for prolonged treatment, the arising of an hypoxia-mediated resistance has been hypothesized, modeled and tested on DU145 tumor cell line.

In Chapter 5, starting from the DEB-TGI models previously developed for anti-angiogenic and cytotoxic treatments, a tumor-in-host approach to analyse combination experiments is proposed. A tumor-in-host growth inhibition model able to predict the response of tumor and host organism to a combined treatment of anti-angiogenic and cytotoxic drugs in case of additivity of the effects is developed and applied to an illustrative example.

An overall conclusion is reported in Chapter 6.

Finally, in Appendix A a population modeling approach to establish a level-A IVIVC between the *in vitro* release of two batches of Progesterone vaginal rings, a dosage form designed for the continuous delivery *in vivo*, and the corresponding serum profiles observed during clinical studies, is presented as example of IVIVC modeling. The model is also used to estimate the expected *in vivo* relative bioavailability of two batches tested *in vitro*.

Chapter 2

A DEB-based approach to model tumor-in-host growth kinetics following cytotoxic anticancer treatment [1]

One of the main assumptions underlying the use of xenograft models is that human cancers xenografted into immunocompromised animals closely reflect the human condition. Nevertheless, mathematical models used to describe data on *in vivo* tumor growth and its inhibition followed an anticancer treatment often neglect the interactions between tumor and host [30].

To cope this gap, a tumor-in-host model has been proposed by van Leeuwen et al. [59]. Based on the Dynamic Energy Budget (DEB) theory, this mathematical model is able to explore and describe the implications of the various tumor-host energetic interactions.

[1] The content of this chapter is partially published in [61].

Starting from the Dutch work and the Simeoni TGI model [40], a new tumor-in-host DEB-TGI model accounting, also, for the pharmacological effect of cytotoxic anticancer treatments in xenograft mice is proposed here. This new model is able to describe in a unique framework the different aspects characterizing the *in vivo* tumor growth studies: the drug cytotoxic activity on the tumor, the onset of cachexia due to the treatment, the effect of the tumor on the host and, viceversa, the influence of the host condition on tumor dynamics. Average data coming from several preclinical experiments involving xenograft mice were successfully analysed with this DEB-TGI model [61] that was able to quantify the antitumor effect of the treatment and, at the same time, to provide a quantitative measurement of its effect on the host growth. In addition, the contributions to cachexia attributable to the drug (drug-related cachexia) and to the tumor (tumor-related cachexia) were dissected in the model.

In this Chapter, the tumor-in-host DEB-TGI model and the assumptions on which it is based are introduced and thoroughly analyzed. In particular, a mathematical analysis is presented and biologically relevant conclusions are discussed with the support of model simulations.

2.1 Unperturbed Tumor-free DEB-based growth

The DEB theory, whose complete and exhaustive formulation can be found in [62, 63, 64], constitutes a general framework that describes host physiology by providing quantitative expressions for the fundamental physiological characteristics and processes, such as food consumption, body growth, metabolic rate and ageing. A reduced formulation of this theory is, hereafter, presented and adopted to model

the physiology of the host organism.

2.1.1 Model formulation and assumptions

The main model assumption, as reported in [59], is that the host body consists of two components: the reserve compounds and the structural biomass. The first pool represents the stored energy, coming from assimilation and essential to carry out the somatic processes, that is growth and maintenance, and the reproductive processes, development and reproduction [58]. The relationship between the structural biomass, conceived as volume and denoted by $V(t)$, and the amount of reserves, $E(t)$, is represented by the utilization rate $U_t(t)$. This is the rate at which the energy mobilized from reserves is made available for physiological processes (Fig. 2.1) and it is described by the equation

$$U_t(t) = \frac{E(t)}{V(t)}\left(\nu V(t)^{2/3} - \frac{dV(t)}{dt}\right) \tag{2.1}$$

where $\nu = \{A_m\}/[E_m]$ is the energy conductance with $\{A_m\} = A_m V_{1\infty}^{-2/3}$ the surface-specific maximum assimilation rate, A_m the maximum assimilation rate, $V_{1\infty}$ the *ad libitum* asymptotic maximum structural volume and $[E_m]$ the maximum reserve density for unit of volume [59, 58].

As in [63], it is assumed that the assimilation rate is given by $A(t) = \rho A_m$ for a given fraction ρ (called food-supply coefficient) of *ad libitum* food consumption.

From Fig. 2.1, it derives that the amount of reserves $E(t)$ is governed by $dE(t)/dt = A(t) - U_t(t)$. Then, given the expressions of $U_t(t)$ and $A(t)$, and defined the scaled energy density $e(t) = E(t)/[E_m]V(t)$, we can obtain

$$\frac{de(t)}{dt} = \nu\left(\frac{\varrho V_{1\infty}^{2/3}}{V(t)} - \frac{e(t)}{V(t)^{1/3}}\right) \tag{2.2}$$

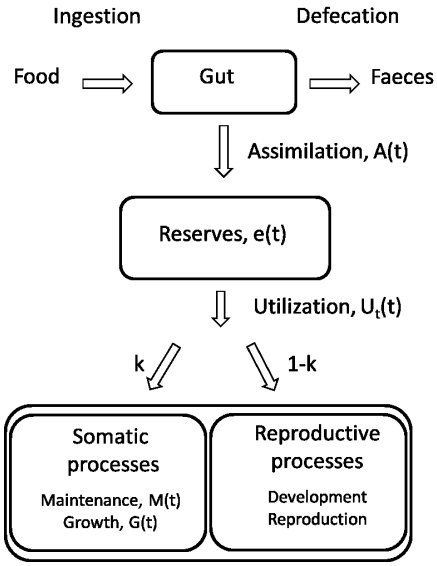

Figure 2.1: Energy fluxes, according to the DEB theory. Food is conceived as material that bears energy. Part of this energy is taken up via blood and delivered to the reserves. Energy required to carry out the various physiological processes is, then, obtained from these reserves. (Source [61])

with initial condition $e(t_0) = e_0$. The presence of the food-supply coefficient ρ in the equation indicates that the food intake directly influences the energy density.

The DEB-theory assumes that somatic (growth and maintenance) and reproductive (development and reproduction) processes take place in parallel. Thus, in accordance with this so-called k-rule, only a fixed fraction k of the available energy is spent for the first. Therefore, the energy available for growing for unit of time, $G(t)$, is

$$G(t) = kU_t(t) - M(t) \tag{2.3}$$

where $M(t)$ represents the maintenance cost amount per time unit. Note that an organism has to give maintenance priority over growth

to stay alive; consequently, increase in size ceases when all the energy available for maintenance and growth is spent on maintenance only. Therefore, maintenance costs determines the ultimate size that an organism can reach.

As in [63], it is reasonably assumed that the growth and maintenance costs per unit of structural volume are constant. Thus, the cost of griwth per time unit, $G(t)$, turn to be proportional to the instant variation of structural volume, while the energy used for maintenance, $M(t)$, to the structural volume (Eqs. 2.4 and 2.5):

$$G(t) = [G]\frac{dV(t)}{dt} \tag{2.4}$$

$$M(t) = [M]V(t) \tag{2.5}$$

where the constants $[G]$ and $[M]$ represent the instant cost of growth and maintenance, respectively.

Combining Eqs. 2.3-2.5, the dynamics of structural biomass can be described as

$$\frac{dV(t)}{dt} = \frac{kU_t(t) - [M]V(t)}{[G]} = \frac{\nu e(t)V(t)^{2/3} - gmV(t)}{g + e(t)} \tag{2.6}$$

with initial condition $V(t_0) = V_0$, where $g = [G]/k[E_m]$ is the energy-investment ratio and $m = [M]/[G]$ the maintenance-growth rate ratio, that can be expressed as

$$m = \frac{\nu}{V_{1\infty}^{1/3} g}\,. \tag{2.7}$$

The actual body weight, $W(t)$, is the sum of the two body compartments (structural biomass and reserves): $W(t) = W_V(t) + W_E(t) = d_V V(t) + d_E E(t)/r_E$, where the coefficients d_V and d_E represent the specific weight of structural biomass and reserves, respectively, and r_E

is defined as the amount of reserves for a unit of volume. As in [58], the expression of host body weight can be rewritten as

$$W(t) = d_V(1 + \xi e(t))V(t), \tag{2.8}$$

where ξ is a dimensionless parameter representing the scaled reserve specific weight and is defined by

$$\xi = \frac{d_E}{d_V}\frac{[E_m]}{r_E}. \tag{2.9}$$

From Eq. 2.8, it can be derived that the initial body weight $W(t_0) = W_0$ is related to the initial volume V_0 through

$$V_0 = \frac{W_0}{d_V(1 + e_0\xi)}. \tag{2.10}$$

Thus, the Tumor-free DEB-based individual model is described by the following system of differential equations (Sys. 2.11) and by the parameters summarized in the host-related section of Tab. 2.1.

$$\begin{cases} \dfrac{de(t)}{dt} = \nu\left(\dfrac{\varrho V_{1\infty}^{2/3}}{V(t)} - \dfrac{e(t)}{V(t)^{1/3}}\right) \\ \dfrac{dV(t)}{dt} = \dfrac{\nu e(t)V(t)^{2/3} - gmV(t)}{g + e(t)} \\ W(t) = d_V(1 + \xi e(t))V(t) \end{cases} \tag{2.11}$$

with $e(t_0) = e_0$ and $V(t_0) = V_0$.

2.1.2 Model analysis

In this section the dynamic system (Sys. 2.11) describing the unperturbed tumor-free growth of the host organism is mathematically

analyzed. In particular, we search for the possible equilibrium points and study their stability (all the proofs of the following propositions are reported in the Supplementary Material of Chapter 2).

Proposition 1: The Tumor-free DEB-based model (Sys. 2.11) admits a unique equilibrium point $P = (\bar{e}, \bar{V}) = (\rho^{1/3}, \rho V_{1\infty})$.

Remark 1: Note that $(\bar{e}, \bar{V}) = (0, 0)$ is not an admissible point because $V(t)$ must to be greater than 0 for each time instant.

Proposition 2: The equilibrium point P is globally asymptotically stable.

Remark 2, asymptotic maximum host body weight: From the stability of the equilibrium point P and Eq. 2.8 that defines $W(t)$ it follows that, as $t \to +\infty$, the body weight of the host organism $W(t)$ tends to $W_{\rho\infty} = d_V(1 + \xi\rho^{1/3})\rho V_{1\infty}$ for any initial condition in $\mathbb{R}^2_+$.

Note that the presence of the food-supply coefficient ρ in the expressions of the asymptotic maximum values of both structural biomass, $V_{\rho\infty} = \rho V_{1\infty}$, and host body weight, $W_{\rho\infty}$, implicates that the food-intake directly influences their values.

2.2 Unperturbed Tumor-in-host DEB-based growth

Host features such as cell proliferation rates, caloric intake, metabolism and energetic conditions, significantly influence the potential tumor growth. At the same time, tumor growth can have relevant implications on the host physiology [53]; indeed, loss of body weight (cachexia) and reduced food intake (anorexia) are widespread syndromes during cancer progression [56].

With the aim of modeling the mutual dependence of tumor and host, the DEB framework has been expanded to also take into account the tumor growth *in vivo*. The starting point is the tumor-in-host model proposed by Van Leuween et al. [59] that has been modified to allow an S-shaped saturation pattern of tumor growth.

2.2.1 Model formulation and assumptions

Tumor cells, as all the other cells, have to obtain nutrients from the host to survive (maintenance) and proliferate (growth). Due to their less differentiation, tumor cells may be characterized by lower growth and maintenance costs and, thus, proliferate faster than normal cells. Moreover, tumor cells may become gluttonous, taking all the available energy at the expense of normal cells. Following these considerations, it is assumed that at each instant a fraction $k_u(t)$ of the energy available for the somatic processes is used by tumor cells (Fig. 2.2).

In particular, in accordance with [59], $k_u(t)$ is defined as a function of tumor volume, $V_u(t)$,

$$k_u(t) = \frac{\mu_u V_u(t)}{V(t) + \mu_u V_u(t)} \tag{2.12}$$

where μ_u is the coefficient of gluttony. From Eq. 2.12, it follows that the amount of energy assigned to the tumor or to the host biomass depends on their corresponding volumes ($V_u(t)$ and $V(t)$), whilst the parameter μ_u determines the weights of the two components for unit of volume. In particular, if $\mu_u = 1$, the energy demand of a tumor cell is the same of an average normal cell; if $\mu_u > 1$, tumor cells are more successful in extracting nutrients from blood than normal cells. For this reason, the parameter μ_u can be considered as a measurement of tumor aggressiveness. The energy rate balance represented by Eq. 2.3

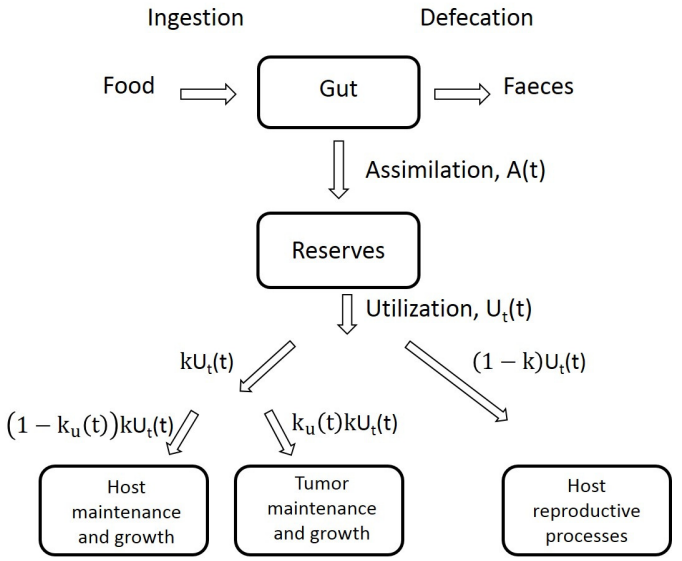

Figure 2.2: Tumor-bearing individual: energy-allocation rules within the DEB framework. Source [61]

is, then, modified as

$$G(t) = k(1 - k_u(t))U_t(t) - M(t)\,. \tag{2.13}$$

Consequently, the dynamics of the structural volume in a tumor-bearing individual is described by

$$\frac{dV(t)}{dt} = \frac{(1 - k_u(t))\nu e(t)V(t)^{2/3} - gmV(t)}{g + (1 - k_u(t))e(t)} \tag{2.14}$$

with initial condition $V(t_0) = V_0$. Similarly, the energy rate available for tumor growth, $G_u(t)$, can be written as

$$G_u(t) = kk_u(t)U_t(t) - M_u(t)$$

being $M_u(t)$ the energy rate necessary for tumor cell maintenance. By defining the tumor growth energy-investment ratio, $g_u = [G_u]/k[E_m]$,

and the maintenance-growth rate coefficient, $m_u = [M_u]/[G_u]$, where the constants $[G_u]$ and $[M_u]$ represent, respectively, the instant cost of tumor growth and maintenance tumor, dynamics can be described as

$$\frac{dV_u(t)}{dt} = \frac{(\nu V(t)^{2/3} + mV(t))gk_u(t)e(t)}{gg_u + (1-k_u(t))g_u e(t)} - m_u V_u(t) \tag{2.15}$$

with initial condition $V_u(t_0) = V_{u_0}$. As the tumor exploits the host resources destined to physiological processes, the maximum size for the host volume, $V_{\rho\infty}$, has to be adjusted to take into account its dependence on tumor size:

$$V_{\rho\infty}(t) = \rho \frac{V(t)}{V_u(t) + V(t)} V_{1\infty}.$$

Thus, the equation for the scaled reserve density (Eq. 2.2) becomes

$$\frac{de(t)}{dt} = \frac{\nu}{V^{1/3}(t)} \left(\varrho \Big(\frac{V_{1\infty}}{V_u(t) + V(t)} \Big)^{2/3} - e(t) \right) \tag{2.16}$$

with initial condition $e(t_0) = e_0$. Eqs. 2.14-2.16 specify the changes in size of both tumor and host as long as the organism disposes energy enough to carry out normal physiological processes and, in particular, to sustain growth costs ($dV/dt \geq 0$). Indeed, if the available energy is not sufficient to satisfy the demand, the host starts degrading its structural biomass to survive and, at the same time, to satisfy the tumor energy demand. The cachexia-related degradation of structural biomass is a thermodynamic process with an efficiency coefficient ω; therefore, for $dV/dt < 0$, the energy rate balances for host and tumor can be written as

$$G(t) = (1 - k_u(t))(kU_t(t) + S(t)) - [M]V(t) = 0 \tag{2.17}$$

$$G_u(t) = k_u(t)(kU_t(t) + S(t)) - [M_u]V_u(t) \tag{2.18}$$

where $S(t)$ is the rate at which the energy is obtained from the degradation of structural biomass[2], described by

$$S(t) = -\omega[G]\frac{dV(t)}{dt}\,. \tag{2.19}$$

From Eqs. 2.17-2.19, for $t \geq t_d$ (with t_d the time instant at which the degradation process starts) the loss of structural biomass and the increase in tumor size are given by

$$\frac{dV(t)}{dt} = \frac{(1-k_u(t))\nu e(t)V^{2/3}(t) - gmV(t)}{(1-k_u(t))(e(t)+\omega g)}$$

$$\frac{dV_u(t)}{dt} = \frac{mgk_u(t)V(t)}{g_u(1-k_u(t))} - m_u V_u(t) = \left(\frac{mg\mu_u}{g_u} - m_u\right)V_u(t)$$

with initial conditions $V(t_d) = V_d$ and $V_u(t_d) = V_{u_d}$.

If the tumor growth is not hindered by drug treatment, host continues to consume biomass with an increasing degradation rate until a time instant, $t_{d_{Max}}$, when a maximum threshold, $\delta_{V_{Max}}$, is reached [61].

Finally, the tumor weight, $W_u(t)$, can be computed as $W_u(t) = d_{V_u}V_u(t)$, where d_{V_u} is the specific weight of tumor mass.

The unperturbed tumor-in-host model is, thus, described by the three systems Sys. 2.20-2.22 and by the host-related, tumor-related and cachexia-related parameters of Tab. 2.1.

[2]Note that the amount of energy per time unit (energy rate) is proportional to the tissue degradation rate, and it has a positive value ($dV/dt < 0$).

- Case $\frac{dV}{dt} \geq 0$ (growing of structural biomass)

$$\begin{cases} \frac{de(t)}{dt} = \frac{\nu}{V^{1/3}(t)}\left(\rho\left(\frac{V_{1\infty}}{V_u(t)+V(t)}\right)^{2/3} - e(t)\right) \\ \frac{dV(t)}{dt} = \frac{(1-k_u(t))\nu e(t)V^{2/3}(t) - gmV(t)}{g+(1-k_u(t))e(t)} \\ \frac{dV_u(t)}{dt} = \frac{(\nu V^{2/3}(t) + mV(t))gk_u(t)e(t)}{gg_u + (1-k_u(t))g_u e(t)} - m_u V_u(t) \\ k_u(t) = \frac{\mu_u V_u(t)}{V(t)+\mu_u V_u(t)} \\ W(t) = d_V(1+\xi e(t))V(t) \\ W_u(t) = d_{Vu}V_u(t) \\ \quad \text{with} \quad e(t_0) = e_0, \quad V(t_0) = V_0 \quad \text{and} \quad V_u(t_0) = V_{u_0} \end{cases} \tag{2.20}$$

- Case $-\delta_{V_{Max}} \leq \frac{dV}{dt} < 0$ (degradation of structural biomass)

Only equations relative to $\frac{dV}{dt}$ and $\frac{dV_u}{dt}$ differ from Sys. 2.20:

$$\begin{cases} \frac{dV(t)}{dt} = \frac{(1-k_u(t))\nu e(t)V^{2/3}(t) - gmV(t)}{(1-k_u(t))(e(t)+\omega g)} \\ \frac{dV_u(t)}{dt} = \left(\frac{mg\mu_u}{g_u} - m_u\right)V_u(t) \end{cases} \tag{2.21}$$

- Case $\frac{dV}{dt} < -\delta_{V_{Max}}$ (degradation of structural biomass at the maximum rate)

Only equations relative to $\frac{dV}{dt}$ and $\frac{dV_u}{dt}$ differ from Sys. 2.20:

$$\begin{cases} \dfrac{dV(t)}{dt} = -\delta_{V_{Max}} \\ \dfrac{dV_u(t)}{dt} = \dfrac{k_u(t)}{g_u}\left(e(t)\nu V(t)^{2/3} + \delta_{V_{Max}}(e(t)+\omega g)\right) - m_u V_u(t) \end{cases} \tag{2.22}$$

2.2.2 Model analysis: exponential tumor growth rate

As already done for the Tumor-free model, in this section a mathematical analysis of the tumor-in-host DEB-based model properties (Sys. 2.20-2.22) is presented. In particular, we search for the possible equilibrium points of the system and study their stability through linearization. Furthermore, biologically relevant considerations on tumor dynamics are derived from the linearized model. All the proofs of the following propositions are reported in the Supplementary Material of Chapter 2.

For reasons of readability, we rewrote the Sys. 2.20-2.22 in a more compact and useful way, simply recalling Eq. 2.12 for $k_u(t)$ and Eq. 2.7 for m:

$$\begin{cases} \dfrac{de(t)}{dt} = \dfrac{\nu}{V^{1/3}(t)}\left(\rho\left(\dfrac{V_{1\infty}}{V_u(t)+V(t)}\right)^{2/3} - e(t)\right) \\ \dfrac{dV(t)}{dt} = F_V(e,V,V_u) \\ \dfrac{dV_u(t)}{dt} = F_{V_u}(e,V,V_u) \end{cases} \tag{2.23}$$

where

$$F_V(e,V,V_u) = \begin{cases} \dfrac{V\left[\nu e(t)V(t)^{2/3} - gm(\mu_u V_u(t) + V(t))\right]}{g(\mu_u V_u(t) + V(t)) + e(t)V(t)} & \text{Case A} \\ \dfrac{V\left[\nu e(t)V(t)^{2/3} - gm(\mu_u V_u(t) + V(t))\right]}{g\omega + e(t)} & \text{Case B} \\ -\delta_{V_{Max}} & \text{Case C} \end{cases} \tag{2.24}$$

$$F_{V_u}(e,V,V_u) = \begin{cases} \left[\dfrac{\left(\nu V(t)^{2/3} + mV(t)\right)ge(t)\mu_u}{gg_u(\mu_u V_u(t) + V(t)) + g_u e(t)V(t)} - m_u\right]V_u(t) & \text{Case A} \\ \left(\dfrac{mg\mu_u}{g_u} - m_u\right)V_u(t) & \text{Case B} \\ \left[\dfrac{\mu_u\left(e(t)\nu V(t)^{2/3} + \delta_{V_{Max}}(e+\omega g)\right)}{g_u(\mu_u V_u(t) + V(t))} - m_u\right]V_u(t) & \text{Case C} \end{cases} \tag{2.25}$$

with the Cases A, B and B determined by the conditions

$$\text{Case A:} \qquad \mu_u V_u(t) \leq V(t)^{2/3} e(t) V_{1\infty}^{1/3} - V(t) \tag{2.26}$$

$$\text{Case B:} \qquad V(t)^{2/3} e(t) V_{1\infty}^{1/3} - V(t) < \mu_u V_u(t) \leq V(t)^{2/3} e(t) V_{1\infty}^{1/3} + \\ -V(t) + V_{1\infty}^{1/3} \delta_{V_{Max}} (e(t) + \omega g) \nu \tag{2.27}$$

$$\text{Case C:} \qquad \mu_u V_u(t) > V(t)^{2/3} e(t) V_{1\infty}^{1/3} - V(t) + \\ + V_{1\infty}^{1/3} \delta_{V_{Max}} (e(t) + \omega g) \nu \tag{2.28}$$

Steady state analysis

Proposition 3: Introduced the secondary parameter

$$\tilde{\lambda}_0 = \frac{mg\mu_u}{g_u} - m_u \,, \tag{2.29}$$

the dynamic systems Sys. 2.20-2.22 predict different behaviours based on the value of $\tilde{\lambda}_0$. In particular,

- if $\tilde{\lambda}_0 \neq 0$, the only equilibrium point is $P_1 = (\bar{e}_1, \bar{V}_1, \bar{V}_{u1}) = (\rho^{1/3}, \rho V_{1\infty}, 0)$;
- if $\tilde{\lambda}_0 = 0$, there are infinite equilibrium points $P_i = (\bar{e}_i, \bar{V}_i, \bar{V}_{ui})_{i>1}$ with

$$\bar{e}_i = \rho \left(\frac{V_{1\infty}}{\bar{V}_{ui} + \bar{V}_i} \right)^{2/3},$$

$$\mu_u \bar{V}_{ui} + \bar{V}_i = \rho V_{1\infty} \left(\frac{\bar{V}_i}{\bar{V}_{ui} + \bar{V}_i} \right)^{2/3}.$$

Remark 3, spontaneous tumor regression: Note that in P_1 the tumor is eradicated and the equilibrium states for the host energy and biomass coincide with that of the equilibrium point P of the Tumor-free model (Proposition 1, Section 2.1.2).

Stability analysis

Proposition 4: The equilibrium point P_1 is unstable if $\tilde{\lambda}_0 > 0$ and locally asymptotically stable if $\tilde{\lambda}_0 < 0$.

Remark 4, exponential tumor growth rate $\tilde{\lambda}_0$: From the linearized system, reported in the Supplementary Material of Chapter 2, it follows that, if the tumor mass is sufficiently small and the conditions of Case A are satisfied (early phase of tumor development), the tumor growth is independent from the structural biomass and the energy reserves and it can be approximated by an exponential growth with a constant rate given by the parameter $\tilde{\lambda}_0$ (Eq. 2.29). Note that the same exponential rate characterizes tumor growth also during the second phase (Eq. 2.25, Case B). Furthermore, the exponential tumor growth rate $\tilde{\lambda}_0$ is strictly linked to the tumor and host cell characteristics. In particular, the maintenance and growth costs of both normal and tumor cells along with tumor gluttony play a central role in these early phases of tumor growth.

Remark 5: For initial conditions that guarantees the asymptotically stability of P_1, the body weight of the host organism $W(t)$ tends to the asymptotic maximum value $W_{\rho\infty}$ already found for the Tumor-free model (Remark 2) when $t \to +\infty$.

Model simulations

From the previous results, it follows that, in the early phases of its development, tumor dynamics are governed by the value of $\tilde{\lambda}_0$. In particular, the relationship $\tilde{\lambda}_0 = 0$ marks the bifurcation between tumor growing ($\tilde{\lambda}_0 > 0$) and spontaneous tumor dying off ($\tilde{\lambda}_0 < 0$).

Fig. 2.3 shows model predictions of tumor and host dynamics for different values of parameters and initial conditions. Data of xenograft mice (15-30 g of body weight) are used as reference.

More in details, for $\tilde{\lambda}_0 > 0$ (red curves) tumor grows exponentially with a rate dependent on the $\tilde{\lambda}_0$ value (i.e. on the values of model parameters m, g, μ_u, g_u and m_u). Consequently, the host starts consuming biomass with an increasing degradation rate until the time instant $t_{d_{Max}}$ when the maximum threshold is reached. Thus, from the Sys. 2.22 it follows that, for $t > t_{d_{Max}}$, the time course of biomass is described by

$$V(t) = V(t_{d_{Max}}) - \delta_{V_{Max}}(t - t_{d_{Max}})\,. \tag{2.30}$$

Eq. 2.30 means that $V(t)$ continues decreasing until a theoretical instant $t_{V=0}$ when $V(t)$ has reached the 0.

For $\tilde{\lambda}_0 < 0$ tumor decreases exponentially and the system tends to P_1 (black solid curves). Note that, in this case, the body weight of the host organism, $W(t)$ tends again to its asymptotic maximum value, $W_{\rho\infty}$. However, for initial conditions (not biologically relevant) in which tumor mass is extremely big in comparison of host volume, the structural biomass $V(t)$ reaches the theoretical bound 0 before the system can reach the equilibrium point P_1 (black dashed curves).

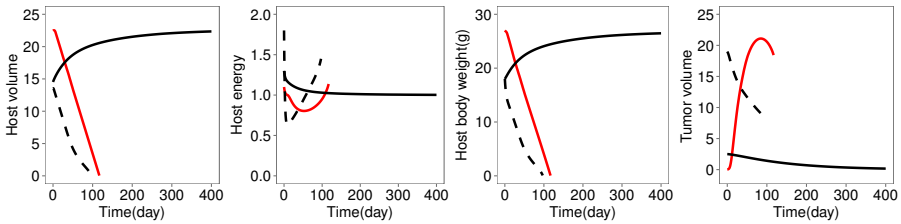

Figure 2.3: Model predictions performed with $\tilde{\lambda}_0 = 0.46 > 0$, $\delta_{V_{Max}} = 0.2$, $V_{u0} = 0.03$g, $e_0 = 1.1$, $W_0 = 27$g and $\rho_b = 1$ (red lines), $\tilde{\lambda}_0 = -0.0073 < 0$, $\delta_{V_{Max}} = 0.2$, $V_{u0} = 2.5$g, $e_0 = 1.3$, $W_0 = 18$g and $\rho_b = 1$ (black solid lines), $\tilde{\lambda}_0 = -0.0073 < 0$, $\delta_{V_{Max}} = 0.2$, $V_{u0} = 19$g, $e_0 = 1.8$, $W_0 = 18$g and $\rho_b = 0.75$ (black dashed lines). Note that host death can occur before the lowest body weight values are actually reached.

From a biological point of view the theoretical bound $V(t) = 0$ (or more generally body weight lower than 10-12 g) is not realistically

reachable because the host death will occur before this limit is actually reached. In particular, according to the recommendations of the international guidelines for the the welfare and use of animals in cancer research, a 20% of weight loss can be considered as reasonable bound for host death.

As a consequence of the previous considerations, it follows that the globally stability for P_1 is not guaranteed even if $\lambda_0 < 0$.

2.3 Tumor-in-host growth under cytotoxic drug treatments

The unperturbed Tumor-in-host model presented in the previous section has been integrated with the assumptions of the Simeoni TGI model [40] to describe the effect of an administered anticancer drug. The undesired drug effects on the host body weight are also been considered.

2.3.1 Model formulation and assumptions

Cytotoxic drugs are assumed to exert two effects: an inhibitory effect on the tumor cell proliferation and a toxic effect on the host body weight due to a reduction of the energy input (assimilation process).

Drug cytotoxic effect on tumor growth: cell kill hypothesis

Drug action on tumor is modeled hypothesizing that a portion of proliferating cells, V_{u1}, becomes non-proliferating due to the anticancer treatment and goes to death through three stages of damage, V_{u2}, V_{u3}, V_{u4}. This cytotoxic activity is assumed proportional to the drug concentration, $c(t)$, and to the proliferating cells through a parameter, k_2, representing the drug potency. Furthermore, only tumor proliferating

cells are supposed able to exploit host resources; thus, the volume of the proliferating cells, V_{u1}, replaces the whole tumor volume, V_u, in all the energetic balances.

Drug effect on host organism: drug-related cachexia

Drug effect on host body weight is modeled hypothesizing that, during days of treatment, side effects, like weakening and lack of appetite or limited assimilation, lead to a temporally decrease of energy intake (drug-related anorexia), followed, eventually, by a loss of structural biomass (drug-related cachexia). The temporary inhibitory effect on the assimilation rate due to the drug is described by a standard I_{max} model:

$$\rho(t) = \rho_b \left(1 - \frac{c(t)}{IC_{50} + c(t)} \right) \tag{2.31}$$

where ρ_b represents the basal food-supply coefficient, with values between 0 and 1, and IC_{50} denotes the drug concentration producing the 50% of the maximal caloric restriction due the drug side effects. Note that the assumption of a time-dependent food-supply coefficient, Eq. 2.31, has an impact on the tumor growth dynamics as well.

In summary, the model for the tumor-bearing treated animals, of which a schematic representation is showed in Fig. 2.4, is described by the following three systems of differential equations (Sys. 2.32-2.34) and by all the parameters reported in Tab. 2.1.

Table 2.1: Structural parameters of the DEB-TGI model.

Parameter	Dimension	Description
Host-related parameters		
ν	L/T	Energy conductance
ρ_b	-	Basal food-supply coefficient
$V_{1\infty}$	L^3	Maximum structural volume
g	-	Growth energy-investment ratio
m	$1/T$	Maintenance-growth rate ratio
ξ	-	Scaled reserve specific weight
d_V	W/L^3	Specific weight of structural biomass
Tumor-related parameters		
μ_u	-	Coefficient of gluttony
g_u	-	Tumor growth energy-investment ratio
m_u	$1/T$	Tumor maintenance-growth rate ratio
d_{Vu}	W/L^3	Specific weight of tumor
Cachexia-related parameters		
ω	-	Thermodynamic extraction efficiency coefficient
$\delta_{V_{Max}}$	L^3/T	Maximum degradation rate
Drug-related parameters		
k_1	$1/T$	First-order rate constant of transit
k_2	$CONC/T$	Drug potency
IC_{50}	$CONC$	Half maximal inhibitory concentration

- Case $\frac{dV}{dt} \geq 0$ (growing of structural biomass)

$$
\begin{cases}
\frac{de(t)}{dt} = \frac{\nu}{V^{1/3}(t)}\left(\rho(t)\left(\frac{V_{1\infty}}{V_{u1}(t)+V(t)}\right)^{2/3} - e(t)\right) \\
\frac{dV(t)}{dt} = \frac{(1-k_u(t))\nu e(t)V^{2/3}(t) - gmV(t)}{g+(1-k_u(t))e(t)} \\
\frac{dV_{u1}(t)}{dt} = \frac{(\nu V^{2/3}(t)+mV(t))gk_u(t)e(t)}{gg_u+(1-k_u(t))g_u e(t)} - m_u V_{u1}(t) - k_2 c(t) V_{u1}(t) \\
\frac{dV_{u2}(t)}{dt} = k_2 c(t) V_{u1}(t) - k_1 V_{u2}(t) \\
\frac{dV_{u3}(t)}{dt} = k_1 V_{u2}(t) - k_1 V_{u3}(t) \\
\frac{dV_{u4}(t)}{dt} = k_1 V_{u3}(t) - k_1 V_{u4}(t) \\
\rho(t) = \rho_b\left(1 - \frac{c(t)}{IC_{50}+c(t)}\right) \\
k_u(t) = \frac{\mu_u V_{u1}(t)}{V(t)+\mu_u V_{u1}(t)} \\
W(t) = d_V(1+\xi e(t))V(t) \\
W_u(t) = d_{Vu}(V_{u1}(t)+V_{u2}(t)+V_{u3}(t)+V_{u4}(t))
\end{cases}
\tag{2.32}
$$

with $e(t_0) = e_0$, $V(t_0) = V_0$, $V_{u1}(t_0) = V_{u1_0}$ and $V_{u2}(t_0) = V_{u3}(t_0) = V_{u4}(t_0) = 0$.

- Case $-\delta_{V_{Max}} \leq \frac{dV}{dt} < 0$ (degradation of structural biomass)

Only equations relative to $\frac{dV}{dt}$ and $\frac{dV_{u1}}{dt}$ differ from the Sys. 2.32:

$$\begin{cases} \dfrac{dV(t)}{dt} & = \dfrac{(1-k_u(t))\nu e(t)V^{2/3}(t) - gmV(t)}{(1-k_u(t))(e(t)+\omega g)} \\ \dfrac{dV_{u1}(t)}{dt} & = \left(\dfrac{mg\mu_u}{g_u} - m_u\right)V_{u1}(t) - k_2 c(t)V_{u1}(t) \end{cases} \tag{2.33}$$

- Case $\dfrac{dV}{dt} \leq -\delta_{V_{Max}}$ (degradation of structural biomass at the maximum rate)

Only equations relative to $\frac{dV}{dt}$ and $\frac{dV_{u1}}{dt}$ differ from the Sys. 2.32:

$$\begin{cases} \dfrac{dV(t)}{dt} & = -\delta_{V_{Max}} \\ \dfrac{dV_{u1}(t)}{dt} & = \dfrac{k_u(t)}{g_u}\left(e(t)\nu V(t)^{2/3} + \delta_{V_{Max}}(e(t)+\omega g)\right) - m_u V_{u1}(t) + \\ & -k_2 c(t)V_{u1}(t) \end{cases} \tag{2.34}$$

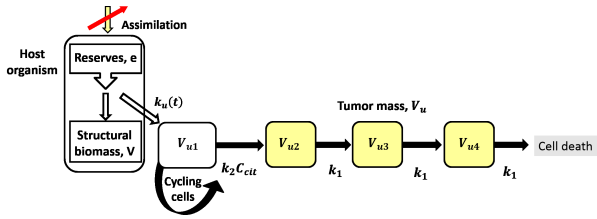

Figure 2.4: Schematic representation of the Tumor-in-host DEB-TGI model.

2.3.2 Model analysis: the concentration threshold for tumor eradication

In this section the dynamic systems Sys. 2.32-2.34 describing the perturbed tumor-in-host growth is analyzed in the biologically rele-

vant case $\tilde{\lambda}_0 > 0$ (i.e. condition for which the model predicts tumor growth in absence of therapy). In particular, following the works of Magni et al. [65] and D'Onofrio et al. [66], we search for the possible equilibrium points and study their stability supposing that the drug is administered through an infusion yielding a (steady-state) constant concentration $c(t) = \bar{c}$. Then, we obtain the minimum constant concentration, c_t, necessary for asymptotic tumor eradication. For reasons of readability, the proofs of all the propositions are reported in the Supplementary Material of Chapter 2.

The systems (2.32)-(2.34) can be rewritten more compactly as

$$\begin{cases} \dfrac{de(t)}{dt} = \dfrac{\nu}{V^{1/3}(t)}\left(\rho(\bar{c})\left(\dfrac{V_{1\infty}}{V_{u1}(t)+V(t)}\right)^{2/3} - e(t)\right) \\ \dfrac{dV(t)}{dt} = F_V(e, V, V_{u1}) \\ \dfrac{dV_{u1}(t)}{dt} = F_{V_{u1}}(e, V, V_{u1}) - k_2\bar{c}V_{u1}(t) \\ \dfrac{dV_{u2}(t)}{dt} = k_2\bar{c}V_{u1}(t) - k_1V_{u2}(t) \\ \dfrac{dV_{u3}(t)}{dt} = k_1V_{u2}(t) - k_1V_{u3}(t) \\ \dfrac{dV_{u4}(t)}{dt} = k_1V_{u3}(t) - k_1V_{u4}(t) \\ \rho(\bar{c}) = \rho_b\left(1 - \dfrac{\bar{c}}{IC_{50}+\bar{c}}\right) \\ W(t) = d_V(1+\xi e(t))V(t) \\ W_u(t) = d_{Vu}(V_{u1}(t)+V_{u2}(t)+V_{u3}(t)+V_{u4}(t)) \end{cases} \tag{2.35}$$

with $F_V(e, V, V_{u1})$ and $F_{V_u}(e, V, V_{u1})$ defined by Sys. 2.24 and Sys. 2.25,

respectively, where the volume of the proliferating cells, V_{u1}, replaces the whole tumor volume, V_u, in all the relationships.

Steady state analysis

Proposition 5: Suppose $\tilde{\lambda}_0 > 0$ and that the anticancer drug is administered through an infusion yielding a (steady-state) constant concentration, $c(t) = \bar{c}$. The equilibrium points of the dynamic system Sys. 2.35 are the following:

- if $\bar{c} \neq \tilde{\lambda}_0/k_2$, the only equilibrium point is $P_{c,1} = \big(\bar{e}_{c,1}, \bar{V}_{c,1}, \bar{V}_{u1_{c,1}}, \bar{V}_{u2_{c,1}}, \bar{V}_{u3_{c,1}}, \bar{V}_{u4_{c,1}}\big) = \big(\rho(\bar{c})^{1/3}, \rho(\bar{c})V_{1\infty}, 0, 0, 0, 0\big)$;
- if $\bar{c} = \tilde{\lambda}_0/k_2$, the infinite equilibrium points $P_{c,i} = \big(\bar{e}_{c,i}, \bar{V}_{c,i}, \bar{V}_{u1_{c,i}}, \bar{V}_{u2_{c,i}}, \bar{V}_{u3_{c,i}}, \bar{V}_{u4_{c,i}}\big)_{i>1}$ are defined by the relationships

$$\bar{e}_{c,i} = \rho(\bar{c})\left(\frac{V_{1\infty}}{\bar{V}_{u1_{c,i}} + \bar{V}_{c,i}}\right)^{2/3} \tag{2.36}$$

$$\mu_u \bar{V}_{u1_{c,i}} + \bar{V}_{c,i} = \rho(\bar{c})V_{1\infty}\left(\frac{\bar{V}_{c,i}}{\bar{V}_{u1_{c,i}} + \bar{V}_{c,i}}\right)^{2/3} \tag{2.37}$$

$$\bar{V}_{u2_{c,1}} = \bar{V}_{u3_{c,1}} = \bar{V}_{u4_{c,1}} = \frac{\tilde{\lambda}_0}{k_2}\bar{V}_{u1_{c,1}} \tag{2.38}$$

Remark 6, tumor eradication: Note that in $P_{c,1}$ the tumor is eradicated and the equilibrium states for the host energy and biomass coincide with those of the tumor-free asymptotic condition (equilibrium point P introduced in the Proposition 1, Section 2.1.2).

Local Stability analysis

Proposition 6: The equilibrium point $P_{c,1}$ is unstable if $\bar{c} < \tilde{\lambda}_0/k_2$ and locally asymptotically stable if $\bar{c} > \tilde{\lambda}_0/k_2$.

Remark 7, concentration threshold for tumor eradication: From Propositions 5 and 6, it follows immediately that, if $\bar{c} > \tilde{\lambda}_0/k_2$, tumor eradication is admissible by the model. Conversely, if $\bar{c} < \tilde{\lambda}_0/k_2$, tumor will not be eradicated because the equilibrium point $P_{c,1}$, predicting tumor eradication, is never stable. Thus, we can define

$$c_t = \frac{\tilde{\lambda}_0}{k_2} \tag{2.39}$$

as the concentration threshold for tumor eradication, that is the concentration level necessary (but not sufficient) to guarantee the eradication of the tumor mass.
This parameter, that depends on the tumor exponential growth rate $\tilde{\lambda}_0$ (and, thus, on the tumor and host cell characteristics m, g, μ_u, m_u and g_u) and on the drug potency k_2, together with the drug clearance, can help choosing an efficacious daily dosage. To make an example, letting C_L [ml/kg/h] denote the drug clearance, the daily dose D [ng/kg] corresponding to the threshold concentration c_t [ng/ml] will be $D = 24 C_L c_t$.

Remark 8, score of the drug-related cachexia: For initial conditions that guarantees the asymptotically stability of the equilibrium point $P_{c,1}$, the body weight of the host organism $W(t)$ tends to $W_{\rho(\bar{c})\infty} = d_V(1 + \xi\rho(\bar{c})^{1/3})\rho(\bar{c})V_{1\infty}$ when $t \to +\infty$.
Note that the inhibition of the food-supply coefficient, ρ, linked to the concentration level $\bar{c}$, results in a reduction of the asymptotic maximum weight, $W_{\rho(\bar{c})\infty}$, reachable by the host organism. In particular, if the drug is ideally administered via a constant infusion, the reduction of the asymptotic maximum value of the host body weight depends only on the concentration level, $\bar{c}$, and on the drug-related parameter IC_{50}. To make an example, Fig. 2.5 shows the asymptotic trends of host body and tumor weight predicted by the model when the drug is administered at a constant concentration $\bar{c} > c_t$ able to guarantee

tumor eradication (asymptotically stability of $P_{c,1}$) for different values of IC_{50}.
From the previous considerations, the ratio $W_{\rho(\bar{c})\infty}/W_{\rho\infty}$ can be considered as a cachexia score for the concentration level $\bar{c}$ of a drug characterized by the toxicity parameter IC_{50} .

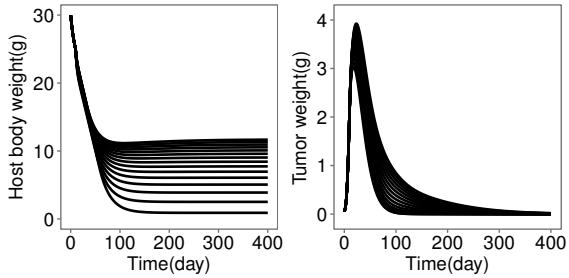

Figure 2.5: Asymptotic dynamics of host body and tumor weight predicted by the model under the assumption of a constant concentration $\bar{c} > c_t$ that guarantees tumor eradication and varying IC_{50} value in the range $0.5 - 14.5$ ng/ml. Simulations performed with $\tilde{\lambda}_0 = 4.6$, $\delta_{V_{Max}} = 0.3$, $k_2 = 0.05$ml/ngday ($c_t = 9.2$ng/ml), $\bar{c} = 9.5$ng/ml, $k_1 = 0.1$ 1/day, $V_{u0} = 0.05$g, $e_0 = 1.3$, $W_0 = 30$g and $\rho_b = 0.75$. Note that host death can occur before the lowest body weight values are actually reached.

Model simulations

From the previous results, it follows that the DEB-TGI model predicts different tumor-host behaviours depending on the drug concentration level $\bar{c}$. In particular, the relationship $\bar{c} = \tilde{\lambda}_0/k_2$ marks the bifurcation between tumor eradication and animal death. However, $\bar{c} > \tilde{\lambda}_0/k_2$ is a condition only necessary, and not sufficient for tumor eradication.

Fig. 2.6 shows the different scenarios predicted by the model by varying the concentration levels $\bar{c}$ and the initial conditions. More in details, for concentration levels under the concentration threshold, $\bar{c} < c_t$, after an initial response phase, tumor re-starts growing and model predicts animal death, $V(t) \to 0$ (red curves).

For concentration levels beyond the concentration threshold, $\bar{c} > c_t$, tumor may be completely eradicated and host may reach its tumor-free asymptotic condition, $W_{\rho(\bar{c})\infty}$ (black solid profiles). However, $V(t)$ may reach its bound $V(t) = 0$ before the solution will converge to the equilibrium point $P_{c,1}$.

Moreover, from a biological point of view, time taken to completely eradicate the tumor may not be compatible with the host survival. Indeed, for initial conditions in which tumor mass is extremely big in comparison of host volume, host death will be occur before tumor eradication (black dashed profiles).

From these considerations, it follows that the globally stability of the equilibrium point $P_{c,1}$, predicting tumor eradication, is not guaranteed even if the concentration level is greater than the concentration threshols c_t. Thus, $P_{c,1}$ is only locally asymptotically stable and its attraction basin depends on parameter values.

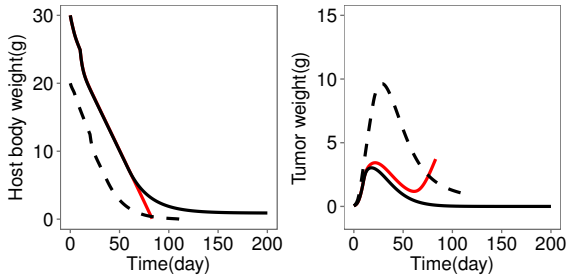

Figure 2.6: Model predictions performed with $\tilde{\lambda}_0 = 0.46 > 0$, $\delta_{V_{Max}} = 0.3$, $\rho_b = 0.75$, $V_{u0} = 0.03$ g, $k_1 = 0.1$ 1/day, $k_2 = 0.05$ ml/ngday ($c_t = 9.2$ ng/ml), $IC_{50} = 0.5$ ng/ml for all the simulations and with $e_0 = 1.3$, $W_0 = 30$ g and $\bar{c} = 6$ng/ml from day 10 (red lines), $e_0 = 1.3$, $W_0 = 30$ g and $\bar{c} = 9.5$ ng/ml from day 10 (black solid lines), $e_0 = 1.8$, $W_0 = 20$ g and $\bar{c} = 9.5$ ng/ml from day 20 (black dashed lines). Note that host death can occur before the lowest body weight values are actually reached.

2.4 Discussion: advantages of the tumor-in-host modeling approach

The Tumor-in-host TGI model presented in this Chapter is based on mechanistic and physiological hypothesis provided by the DEB theory and characterized by parameters with a precise biological meaning. For this reasons, results followed from the previous mathematical analysis suggest some further considerations. More in details, similarities, differences and advantages of the DEB-TGI model in respect to the Simeoni TGI model are discussed in the following sections.

2.4.1 A mechanistic justification for the exponential tumor growth rate

From the mathematical analysis of the unperturbed model, fully derived from theoretical considerations/assumptions, it follows that, in the early phases of tumor development, tumor growth is approximately exponential and governed by a rate, $\tilde{\lambda}_0$ (Eq. 2.29), strictly linked to the tumor and host cell characteristics (Section 2.2.2).

This founding is in accordance with the hypothesis of the empirical Simeoni model that, based on experimental evidence, supposes an exponential + linear tumor growth. The relationship between the empirical parameter λ_0 and the physiologically-based parameter $\tilde{\lambda}_0$ was confirmed, also, by comparable estimates obtained on experimental data of xenograft mice [61]. Moreover, from the simulation analysis reported in [61], the empirical switch point between the exponential and the linear phase of the Simeoni model seems to be linked to the third phase of the DEB-based model (degradation of structural biomass with maximum rate). Indeed, the change in tumor growth dynamics modelled by the Simeoni model always occurs when the tumor slows down its growth while the host degrades its structural biomass

at the maximum rate, and the energy demand remains unfulfilled.

Thus, the model here presented, based on the description of the energetic interactions between tumor and host, can provide a mechanistic explanation to the empirical tumor growth curve introduced by the Simeoni model and observed in huge numbers of xenograft experiments.

Moreover, the presence of species-dependent physiological parameters would allow, from a theoretical point of view, the translation from one species to another. It would be sufficient estimating the growth parameters of the specific species and applying the identification strategy described in [61] to analyse tumor weight data. Interestingly, an exponential growth (constant increase of tumor volume on a logarithmic scale in relation to time) has been observed for several types of human malignancies [67].

Thus, an interesting open point is how the Tumor-in-host DEB-TGI model could be applied and used as an efficient translational tool from animal to human studies of anticancer drug activity.

2.4.2 Unbiased estimates of cell killing drug effect

As the Simeoni TGI model, the DEB-based perturbed model presented in the Section 2.3 is able to quantify the drug effect on tumor growth providing a quantitative measurement of its cytotoxic activity. In particular, the drug efficacy parameters (k_1 and k_2) maintain the same meaning providing similar efficacy metrics.

However, the tumor-in-host approach provides a better interpretation of tumor growth inhibition dynamics. Indeed, it is able to disentangle the direct effect of the drug on tumor cells from the slowdown in tumor growth due to the depletion of host energies, possibly occurring during cancer progression and after the administration of anticancer treatment. Conversely, current modeling approaches, not accounting for host features, explain tumor growth inhibition only as

a consequence of the direct cytotoxic effect of the drug. This could lead to an overestimation of the drug efficacy parameters, such as the potency parameter k_2 in the Simeoni TGI model.

Actually, comparing the estimates of the parameter k_2 obtained by the DEB-TGI model [61], $k_{2,DEB}$, with those available for the Simeoni TGI model [41], $k_{2,Sim}$, this bias seems to be confirmed ($k_{2,Sim} > k_{2,DEB}$), although its entity is very limited. However, it is worth to note that the experimental studies analyzed in [61, 41] were essentially focused on the efficacy assessment and that their administration schedules and dose levels were selected within a range of acceptable tolerability. Nevertheless, in presence of more severe toxicities the overestimation of drug efficacy could be more relevant.

To further investigate this aspect, from a theoretical point of view, borderline cases were analysed through a simulation approach. The tumor-in-host DEB-TGI model (Sys. 2.32-2.34) identified on data collected during a xenograft study on paclitaxel (Exp. a analyzed in [61]) was used as starting point to assess the tumor inhibition response after administration of several (simulated) drugs, differing from each other for efficacy and/or toxicity.

In particular, by varying the values of parameters related to drug potency ($k_{2,DEB}$) and drug toxicity on host body weight (IC_{50}), and keeping fixed all the other model parameter to the value reported in [61] for Exp. a, the tumor time-course after an administration following the same dose and schedule of Exp. a (30 mg/kg i.v. q4dx3 from day 8) was simulated. Then, the drug-related parameters ($k_{1,Sim}$ and $k_{2,Sim}$) of the Simeoni TGI model were estimated on these simulated data, while the tumor-related parameters (λ_0, λ_1 and W_0) were fixed to the estimates obtained from experimental data of the control group of Exp. a.

In particular, starting from values of $k_{2,DEB}$ and IC_{50} of the DEB-TGI model close to the estimates obtained for paclitaxel ($k_{2,DEB}$ = 6.5e-4 ml/ngday and IC_{50} = 0.461 ng/ml), simulations were per-

formed increasing drug toxicity (IC_{50} =5e-1, 1e-1, 1e-2, 1e-3, 1e-4,1e-5 ng/ml) and decreasing drug potency ($k_{2,DEB}$=6.5e-4, 1e-4,1e-5, 1e-6,1e-7 ml/ngday). The estimated values of the $k_{2,Sim}$ parameter of the Simeoni TGI model, normalized by the $k_{2,DEB}$, are reported in Fig. 2.7.

DEB-TGI model : increasing toxicity ($1/Ic_{50}$)

DEB-TGI model : decreasing efficacy (k_2)

$k_{2,DEB}$ \ Ic_{50}	Ic_{50}=5e-1 ng/ml	Ic_{50}=1e-1 ng/ml	Ic_{50}=1e-2 ng/ml	Ic_{50}=1e-3 ng/ml	Ic_{50}=1e-4 ng/ml	Ic_{50}=1e-5 ng/ml
$k_{2,DEB}$=6.5e-4 ml/ngday	1.68	1.99	2.46	2.80	2.92	3.09
$k_{2,DEB}$=1e-4 ml/ngday	4.31	6.15	9.12	10.40	11.20	11.50
$k_{2,DEB}$=1e-5 ml/ngday	33.1	50.4	79.7	90.8	96.5	101
$k_{2,DEB}$=1e-6 ml/ngday	308	499	795	890	950	996
$k_{2,DEB}$=1e-7 ml/ngday	3050	4930	7900	9310	9430	9730

Figure 2.7: Estimates of the parameter $k_{2,Sim}$ [ml/ngday] of the Simeoni TGI model on tumor weight data simulated by the DEB-TGI model varying the values of $k_{2,DEB}$ and IC_{50} and keeping fix all the other model parameters to the estimates reported in [61] for Exp. a, normalized by the $k_{2,DEB}$.

The comparison of drugs characterized by the same cytotoxic potency (i.e., data simulated by DEB-TGI with the same $k_{2,DEB}$ value, rows in Fig. 2.7) indicates that the Simeoni TGI model estimates a higher efficacy for drugs with higher toxicity (i.e., simulations performed with lower IC_{50}, columns in Fig. 2.7).

As extreme situations, we can compare the $k_{2,Sim}$ value obtained by identifying the Simeoni TGI model on the dataset simulated with $k_{2,DEB}$ = 6.5e-4 ml/ngday and IC_{50} = 5e-1 ng/ml (highest cytotoxic effect on tumor cells and lowest toxic effect on host body weight) to the value obtained for the drug simulated with $k_{2,DEB}$ = 1e-7 ml/ngday and IC_{50} = 1e-5 ng/ml (lowest cytotoxic effect on tumor cells and

highest toxic effect on host body weight). The Simeoni TGI model provided almost the same estimates of drug efficacy ($k_{2,Sim}$) for these two quite different simulated drugs. Fig. 2.8 shows the simulated data and the predictions of the Simeoni TGI model in the two considered scenarios.

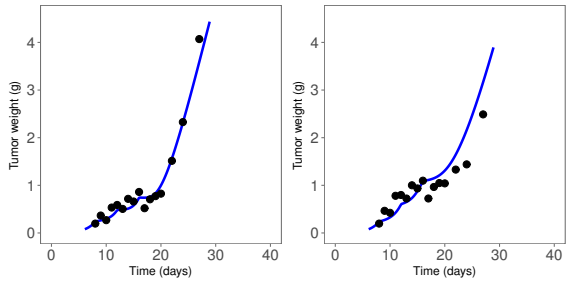

Figure 2.8: Identification of Simeoni TGI model on simulated data: tumor weight profiles obtained identifying the Simeoni TGI model on data simulated with DEB-TGI model by using parameter values of the Exp.a, $k_{2,DEB}$=6.5e-4 ml/ngday and IC_{50}= 5e-1 ng/mL (left panel) or $k_{2,DEB}$= 1e-7 mL/ngday and IC_{50}= 1e-5 ng/mL (right panel).

In summary, this simulation analysis showed that, at least from a theoretical point of view, not including host feature and in particular the cachexia phenomena in the modelling approach could lead to a biased estimation of the cytotoxic drug potency. However, from the experience collected on real experimental data, this bias seems to be not so relevant in presence of acceptable toxicity and efficacy, as usually happen in the real typical studies done for drug development.

2.4.3 Necessary condition for tumor eradication

Following the work of Magni et al. [65] for the Simeoni TGI model, a stability analysis of the DEB-based perturbed growth model was conducted under the assumption that drug is administered through an infusion yielding a (steady-state) constant concentration, i.e. $c(t) = \bar{c}$.

The mathematical analysis, reported in Section 2.3.2, partially confirmed the results obtained by Magni et al.. In particular, a concentration threshold, c_t, beyond which tumor can be asymptotically eradicated was found. Nevertheless, these results require two further considerations.

First, similarly to the Simeoni TGI model, the concentration threshold c_t (Eq. 2.39), depends on the tumor exponential growth rate, $\tilde{\lambda}_0$, and on the drug potency, $k_{2,DEB}$. However, the exponential growth rate of the DEB-based model is not an empirical parameter but is inherently linked to the tumor and host cell characteristics (Eq. 2.29). Moreover, as discussed in the Section 2.4.2, the estimate of drug potency provided by the DEB-TGI model is purified by the tumor slowdown due to the depletion of host energies. Thus, because $k_{2,DEB}$ provides a more representative measurement of the cytotoxic drug activity, from a theoretical point of a view the concentration threshold predicted by the tumor-in-host DEB-TGI model could be a more realistic efficacy metrics.

Furthermore, if the drug is administered via a constant infusion with a concentration level beyond the threshold c_t, the Simeoni TGI model predicts complete tumor eradication starting from any possible initial condition. Differently, for the DEB-TGI model, the condition $\bar{c} > c_t$ is only necessary and not sufficient to guarantee tumor eradication because host death could occur before tumor will be completely eradicated. This result, following from the tumor-in-host approach and more representative of the experimental *in vivo* studies, could help to identify anticancer drug concentration levels effective and, at the same time, compatible with the survival of the host organism. In particular, utility curves could be developed exploited the DEB-TGI model that, considering the drug effect on the host body weight as a toxicity of the anticancer treatment, allows a risk/benefit assessment between tumor eradication and host survival to a negative energetic balance.

2.4.4 Experimental protocol design based on cachexia phenomena

The tumor-in-host DEB-TGI model simultaneously describes both the tumor growth inhibition followed drug administration and its undesired effect on the normal animal growth. For these reasons, it could be extremely useful for a protocol design based on considerations about drug efficacy as well as drug toxicity on animal body weight (even if body weight decreasing is not the only toxicity sign and also other elements, not considered in this modelling approach, actually influence the experimental design).

In fact, once the model has been identified on data generated during standard preclinical studies, the concentration threshold for tumor eradication, c_t, and, thus, an ideally efficacious daily dosage, D, can be calculated. Based on this daily dose, one can consider different administration protocols, theoretically ensuring tumor regression, and, using the model, predict the expected degree of cachexia for each of them.

The advantages of knowing in advance the effect of the anticancer treatment on host conditions are manifold. First, significant body weight loss (BWL $> 20\%$) were indicated as ethical criteria for animal sacrifice by the international guidelines for animal care and euthanasia. Second, preventing high cachexia degree could help to avoid biased situations in which tumor regression is imputable not only to the anticancer drug effect but also to the degradation of host conditions, resulting in an uncorrected evaluation of drug efficacy (see Section 2.4.2).

Starting from the Exp. a on paclitaxel analyzed in [61], we show, as an example, a possible evaluation of different administration protocols.

First of all, from experimental data, a theoretical concentration threshold of about 720 ng/ml was identified and, considering the paclitaxel clearance in mice, an efficacious daily dosage of about 12.2

mg/kgday was computed. Then, the DEB-TGI model was used to find the maximum dose causing a BWL below the 20% of the initial animal body weight: supposing an initial weight of 25 g, a bound of 20 g was found. Adopting the same administration schedule of Exp. a (q3dx4 starting from day 8), tumor and host body weight responses after a bolus administration of 48.8, 60, 70, and 80 mg/kg were simulated. As can be seen from the first panels in Fig. 2.9 (Panels A)), all the considered dose levels lead to a tumor regression without relevant differences in terms of toxic effect on host body weight suggesting that, in absence of other toxic effects, a higher level than the minimum efficacious daily dosage could be consider eligible for experimental assessment.

A second possible scenario considered different administration protocols characterized by the same total dose. In particular, a total dose of 146.4 mg/kg over 12 days was simulated by varying the administration protocol (12.2 mg/kg q1dx12, 24.4 mg/kg q2dx6, 36.6 mg/kg q3dx4 and 48.8 mg/kg q4dx3). The tumor and host body weight responses are reported in the lower panels of Fig. 2.9 (Panels B)). As you can seen, only the last protocol respected the toxicity bound of 20% BWL suggesting that q4dx3 is the preferable administration protocol in terms of cachexia degree.

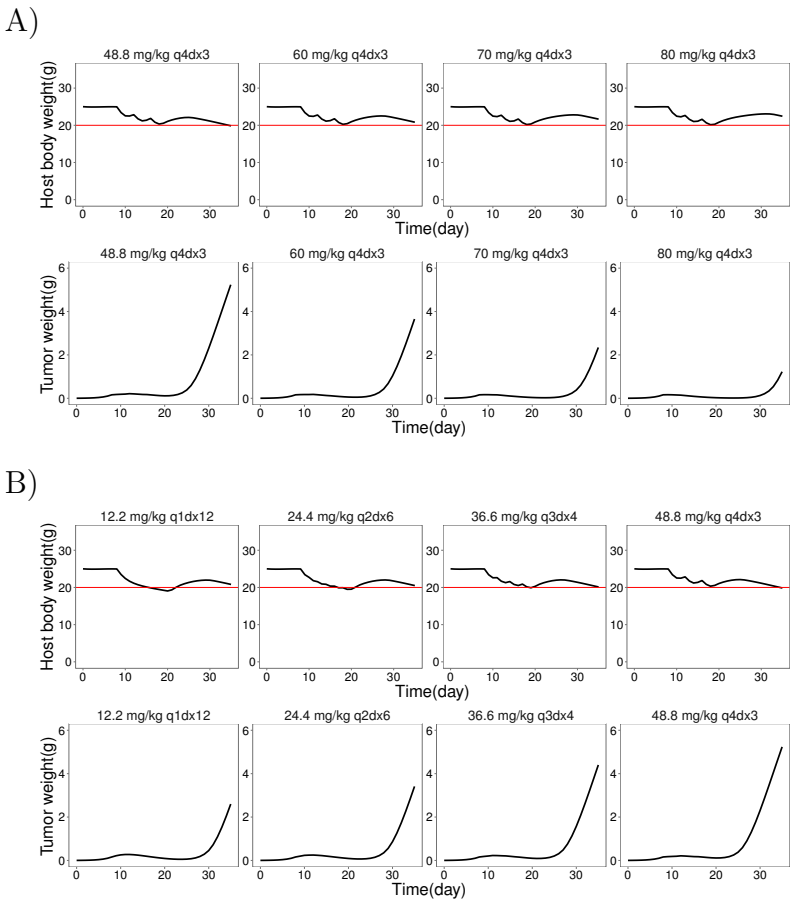

Figure 2.9: Simulated host body and tumor weight response following the paclitaxel treatment with the different administration protocols (Black curves). Horizontal red line indicate the toxicity limit of 20% BWl

Chapter 3

A population Tumor-in-host DEB-based TGI model for etoposide effects on Wistar rats [1]

Traditional PK-PD models generally used to analyse preclinical data of tumor growth inhibition suffer of some gaps. As already discussed in the previous chapter, they are commonly based on an empirical approach that allows to describe only a part of the several aspects characterizing the *in vivo* tumor growth studies. In particular, the mutual influence of tumor and host physiology, as well as the possible toxic effect of anticancer treatment on the host organism is usually neglected. Moreover, the anticancer drug effect is generally driven by plasma concentration that, in case of relevant differences in tumor tissue penetration, could not represent a good surrogate of the phar-

[1] The content of this chapter is partially published.

macologically active concentration [68, 69, 70]. Finally, experiments not optimally designed and, thus, poorly informative make difficult the development and application of more mechanistic models.

In this chapter, the DEB-TGI model previously introduced in Chapter 2 was adapted to analyse average and individual data relative to the etoposide effects on Wistar rats. The unusual experimental design, including control groups used for measuring animal weight changes in both treated and untreated animals without tumors, and the availability of information about intratumoral concentration allowed to fully exploit model capabilities of describing and distinguishing all the dynamics characterizing the *in vivo* tumor studies.

3.1 Background

In a recent work, Pigatto et al. applied the well-known Simeoni TGI model to investigate the PK/PD relationship between total plasma, free interstitial tumor etoposide concentrations and tumor growth dynamics [44]. In this study, the activity of etoposide, a topoisomerase II inhibitor used for treating hematopoietic malignancies and different solid tumors, was evaluated on Walker-256 (W256) tumor line implanted in Wistar rats.

The considered experiment was characterized by an unusual design. Differently from the typical preclinical studies, in which tumor-bearing animals are randomized in control and treated groups, two additional experimental arms were here included: a tumor-free untreated group and a tumor-free treated group of healthy animals treated with placebo or etoposide, respectively. However in [44], data collected within these two arms, as well as host body weights of both tumor-bearing rats, were not included in the modeling efforts.

Experimental results showed a significant antitumor activity of etoposide. In particular, drug effect exhibit a relevant dependence on

the administration protocol: the 8-day treatment with $5\,\mathrm{mg/kg \cdot day}$ presented greater tumor growth inhibition compared to the 4-day treatment with $10\,\mathrm{mg/kg \cdot day}$. Becouse the original Simeoni TGI model resulted inadequate to describe the schedule-dependence of the etoposide effect, an empirical inhibitory Emax function was introduced on the k_2 parameter to account for this phenomenon (Simeoni TGI-Emax model) [44].

Furthermore, the availability of information about intratumoral concentration allowed to comparatively evaluate the PK/PD relationship between total plasma and free-interstitial tumor concentration to tumor growth kinetics. Results suggested that, in this case, free intratumoral concentration could be a better surrogate for the active concentration exhibiting a cytotoxic effect on tumor cells.

A population tumor-in-host DEB-TGI model able to describe tumor and host body weight data collected in the etoposide study on Wistar rats was developed and presented in this chapter. The tumor-in-host approach allowed to better exploit and distinguish the different factors highlighted by the unusual experimental design of this *in vivo* tumor study. Moreover, the potential advantages arising by the use of the free intratumor concentration as PK input for modeling the cytotoxic drug effect was, also, evaluated in the more mechanistic framework provided by the DEB approach. Finally, the applicability of the model to a target species (rat) different from xenograft mice, in which it was originally developed, was demonstrated.

3.2 Experimental setting

3.2.1 Compound

An etoposide solution, similar to the commercial injectable formulation administered in humans [71, 72], was used for the *in vivo*

antitumor assessment.

3.2.2 Animals, cell lines and *in vivo* tumor growth experiments

Thirty-eight male Wistar rats (150-200 g, 5-6 weeks of age) were obtained from the Center for Reproduction and Experimentation of Laboratory Animals (CREAL/UFRGS - Porto Alegre, Brazil) and received food and water ad libitum. Animal procedures were approved by UFRGS Ethical Committee on Animal Use (CEUA/UFRGS, protocol number 22302) and were conducted under standard conditions according the Brazilian law [73] and the guideline on experimental animal care and use [74].

Walker-256 (W256), a rat breast carcinoma cell line syngeneic to Wistar rats, were used to obtain tumor-bearing animals.

The thirty-eight animals were randomized in the following five arms: tumor-free untreated arm (n=4), tumor-free treated arm (n=3), tumor-bearing untreated arm (n=10) and two tumor-bearing treated arms subjected to two different administration schedules (n=10 and n=11).

For the tumor-bearing arms, the experimental setting is the same described in the Section 1.3.1. In particular, 2×10^7 viable cells were inoculated s.c. and, after about 5 days since inoculation, animals showed a palpable tumor volume of $1\,cm^3$ in average. Etoposide was administrated i.v. to the treated animals as follows: bolus of 10 mg/kg once daily for 4 days (n = 10) or $5\,mg/kg$ once daily for 8 days (n = 11) in the tumor-bearing treated groups; bolus of 10 mg/kg once daily for 4 days in the tumor-free treated group. In order to maintain ceteris paribus condition, vehicle was administered to the two control groups (untreated tumor-bearing/tumor-free animals). Rats were clinically evaluated and weighted daily for 30 days after the inoculation time.

Animals with a tumor diameter higher than $4\,cm$, 20% weight loss compared to baseline weight or inability to eat/drink water were sacrificed before the end of the experiment according to the international guidelines [75].

The collected data were partially analysed in [44]: only average and individual tumor weights were modeled, whereas data related to rat body weights (including those collected in the two tumor-free groups) are unpublished.

3.3 Modeling approach

3.3.1 PK models for etoposide: total plasma and free peripheral tumor concentration

Etoposide PK in W256 tumor-bearing Wistar rats

The PK of etoposide in W256 tumor-bearing Wistar rats was previously investigated in plasma and tumor tissues [76]. A population PK model (popPK), simultaneously describing etoposide concentration in plasma and free concentrations in two regions of the tumor (called centre and periphery), was proposed by Pigatto et al. [76]. The model consists of four compartments with a saturable distribution from plasma to tumor compartments and a first-order elimination. The volume of plasma compartment is a function of body weight. A schematic representation of the model structure and the mathematical equations are reported in the Supplementary Material to Chapter 3.

Because PK and PD data were collected in independent studies involving a different number of animals, inter-individual variability affecting PK parameters was not considered in the identification of the PK-PD model [77]. Therefore, total plasma and free peripheral tumor drug concentration-time profiles were simulated in the tumor-

bearing groups by fixing the values for the model parameters reported in Tab. 3.1. The volume of plasma compartment was computed from the animal body weight. The simulated profiles are reported in the Supplementary Material to Chapter 3 for both the total plasma and the free peripheral tumor concentration in the tumor-bearing groups

Etoposide PK in tumor-free Wistar rats

No ad-hoc PK studies were performed in healthy animals. However, the main etoposide plasma PK parameters (AUC, CL and $t_{1/2}$) obtained for W256 tumor-bearing rats [76] were similar to those reported in the literature for healthy animals [78, 79]. Based on this evidence, a classical PK model (three-compartment model), built reanalysing only plasma etoposide concentration data collected in W256 tumor-bearing Wistar rats, was used to obtain etoposide plasma profiles in tumor-free rats . The central compartment volume was modeled as a function of the animal body weight through a covariate model.

Analogously to the tumor-bearing case, the inter-individual variability affecting PK parameters was not considered in the identification of the PK-PD model. Then, the total plasma concentration profiles in tumor-free rats were simulated by fixing the values for the model parameters reported in Tab. 3.1. The volume of the central compartment was computed from the animal body weight. The simulated profiles in the tumor-free group are reported in the Supplementary Material to Chapter 3.

3.3.2 PD model structure

The tumor-in-host DEB-based TGI model introduced in Chapter 2 was adopted as starting point to describe tumor and host growth in response to etoposide treatment. The model structure was revised to

Table 3.1: Parameter values of the etoposide PK models.

Parameter [Dimensions]	**Tumor-free groups**	**Tumor-bearing groups**
V_1 $[L]$	0.161	0.171
β $[-]$	0.561	0.581
k_{10} $[1/day]$	36.24	30.48
k_{12} $[1/day]$	12.38	68.64
k_{21} $[1/day]$	9.99	69.12
k_{13} $[1/day]$	81.12	-
k_{31} $[1/day]$	93.6	95.76
k_{41} $[1/day]$	-	5.18
V_3 $[L]$	-	0.112
V_4 $[L]$	-	2.99
V_{max} $[\mu g/day]$	-	21.77
k_m $[\mu g/day]$	-	5.12
F_p [-]	-	0.155

account for etoposide-specific behaviours and to describe tumor-free treated animals as explained hereafter.

Tumor-bearing animals

The unperturbed Tumor-in-host model (Sys. 2.20-2.22) was used to describe tumor and host dynamics observed in the tumor-bearing group. Since, in this, study the decreases of rat (net) body weight in presence of big tumor masses was not completely justified by tumor energy request, it was hypothesized that big tumor masses can lead to symptoms, like lack of appetite or limited assimilation, get aggravated with tumor progression (tumor-related anorexia). Thus, the food-supply coefficient ρ was described as a function of tumor volume to account for the energy intake reduction linked to tumor progression. Then:

$$\rho(t) = \rho_b \left(1 - \frac{V_u(t)}{IV_{u_{50}} + V_u(t)} \right) \tag{3.1}$$

where ρ_b represents the food-supply coefficient in absence of tumor masses (with values between 0 and 1) and $IV_{u_{50}}$ is the tumor volume

producing a 50% reduction of the energy intake.

The Tumor-in-host DEB-TGI model (Sys. 2.32-2.34) was adopted to describe etoposide activity on tumor-bearing treated animals. As discussed in Section 2.3.1, the drug effect on host body weight is modeled hypothesizing that side effects of treatment lead to a temporally decrease of energy intake, followed by a loss of structural biomass (drug-related cachexia). Otherwise, in this case, a sigmoidal Imax model resulted more appropriate to describe etoposide toxic effect on assimilation rate. Moreover, data showed a delay between the end of the treatment and the regrowing of the rat body weight. Because this trend was evident in all the three treated groups and, in particular, in the tumor-free treated arm, we conclude that the prolonged body weight decrease is independent from tumor-host interaction and imputable only to drug dynamics. Thus, an effect compartment was included in the model and the effect compartment concentration, C_{Eff}, was used to drive the energy intake inhibition. Therefore, the food-supply coefficient $\rho(t)$ in the treated groups was defined as:

$$\rho(t) = \rho_b\left(1 - \frac{V_{u1}(t)}{IV_{u_{50}} + V_{u1}(t)}\right) \cdot \left(1 - \frac{C_{Eff}(t)^{\eta}}{IC^{\eta}_{Eff_{50}} + C_{Eff}(t)^{\eta}}\right) \quad (3.2)$$

where $IC_{Eff_{50}}$ denotes the effect compartment concentration producing a 50% reduction of the energy intake and η is the Hill coefficient.

Tumor-free animals

The unperturbed tumor-free growth was described by the Sys. 2.11. However, the Tumor-free model has to be modified to account for the drug effect on the body weight growth in treated tumor-free animals (Sys. 3.3-3.5). An inhibition of the energy intake was introduced to describe body weight loss occuring during the treatment period and the days immediately after. Consequently, since host energy resources could be insufficient to fully satisfy the energy needs, the degradation

of the structural biomass (drug-related cachexia) was allowed also in absence of any tumor masses to cover the maintenance costs.

- Case $\dfrac{dV}{dt} \geq 0$ (growth of structural biomass)

$$\begin{cases} \dfrac{de(t)}{dt} = \nu\left(\dfrac{\varrho(t)V_{1\infty}^{2/3}}{V(t)} - \dfrac{e(t)}{V(t)^{1/3}}\right) \\ \dfrac{dV(t)}{dt} = \dfrac{\nu e(t)V(t)^{2/3} - gmV(t)}{g + e(t)} \\ \dfrac{dC_{Eff}(t)}{dt} = k_{Eff}\big(C_{Plasma}(t) - C_{Eff}(t)\big) \\ \rho(t) = \rho_b\left(1 - \dfrac{C_{Eff}(t)^\eta}{IC_{Eff_{50}}^\eta + C_{Eff}(t)^\eta}\right) \\ W(t) = d_V(1 + \xi e(t))V(t) \\ \qquad \text{with} \quad e(t_0) = e_0 \quad \text{and} \quad V(t_0) = V_0 \end{cases} \tag{3.3}$$

where $C_{Plasma}(t)$ is the total plasma concentration of the drug and $C_{Eff}(t)$ the effect-site concentration.

- Case $-\delta_{V_{Max}} \leq \dfrac{dV}{dt} < 0$ (degradation of structural biomass)

Only the equation relative to $\frac{dV}{dt}$ differs from Sys. 3.3 as

$$\frac{dV(t)}{dt} = \frac{\nu e(t)V(t)^{2/3} - gmV(t)}{g + e(t)} \tag{3.4}$$

- Case $\dfrac{dV}{dt} < -\delta_{V_{Max}}$ (degradation of structural biomass at the maximum rate)

Only the equation relative to $\frac{dV}{dt}$ differs from Sys. 3.3 as

$$\frac{dV(t)}{dt} = -\delta_{V_{Max}}\,. \tag{3.5}$$

3.3.3 Data analysis

PK and PD models were implemented in Monolix (version 2016R1) [80]. Goodness Of Fit (GOF) plots were performed in R (Version 3.4.4) on the graphic data exported from Monolix.

Total plasma and free peripheral tumor concentration-time profiles of etoposide were simulated by the PK models reported in Section 3.3.1. Model fitting was performed simultaneously on tumor and rat net body weight data collected in all the five experimental arms. The quantification limit for the tumor diameter was set to $3\,mm$ (the minimum value appreciable with the calliper), corresponding to a tumor volume of $0.01\,g$. Therefore, in the following analysis, tumor measurements below the quantification limit (BQL) were coded as left censored data (30% of the total tumor measurement), while the correspondent body weights were considered as net body weights.

As a first step, the model structure was defined and assessed on average data adopting a naïve average data approach, a strategy frequently adopted in preclinical TGI modeling. Then, as second step, individual data were directly taken into account through a Non Liner Mixef Effect (NLME) approach [81] .

Different from [61], the presence of also a tumor-free untreated arm allowed to identify all the model parameters, host-related (g, ν, $V_{1\infty}$, ξ, ρ_b), tumor-related (μ_u, g_u, m_u, IV_{u50}), cachexia-related ($\delta_{V_{max}}$) and drug-related (k_1, k_2, $IC_{Eff_{50}}$, k_{Eff}), in a single step. The parameter m was derived by Eq. 2.7; the thermodynamic efficiency coefficient ω was fixed to 0.75; the density of structural biomass, d_V, and of tumor volume, d_{V_u}, were fixed to $1\,g/cm^3$. The Hill coefficient η was fixed to a value sufficiently high to make steep the inhibitory response curve ($\eta = 50$). The initial time instant, t_0, was set to the inoculation day; the initial conditions (e_0, W_0 and V_{u0}) were estimated from data together with the other model parameters. Finally, initial value of structural biomass, V_0, was derived from Eq. 2.10.

In the preliminary analysis on the average data, the model was identified fixing the food-supply coefficient ρ_b to 1. Because, at the begin of the experiment, average rat body weights showed a relevant inter-group variability (CV% upper than 20%), a log-normally distributed random effect was added on W_0 parameter.

In the NLME approach, inter-individual variability was assigned only on the initial conditions of energy, host body weight and volume of inoculated tumor cells (i.e., e_0, W_0 and V_{u10}). Individual model parameters (P_i) were supposed to be log-normally distributed ($P_i = \theta \exp(\eta_i)$ where θ is the typical population value and η a normally distributed random effect with zero mean and variance ω^2). The food-supply coefficient ρ_b, that takes value in $[0, 1]$, was re-parametrized as $\rho_b = 1/(1+R_b)$ with R_b in $[0, +\infty]$. A log-normally distributed random effect was added on R_b to take into account inter-individual variability affecting the assimilation process. A first preliminary data analysis showed a significant difference (in average) between the initial weight of the tumor-bearing and the tumor-free animals. Thus, to improve model performance, a categorical covariate tumor-free/tumor-bearing was added on the typical value of W_0 parameter.

The residual error model was supposed proportional to the square root of the predicted values (i.e. body or tumor weights), thus $y = f + b\sqrt{f}\epsilon$ where y is the measurement, f the predicted value, b a coefficient and ϵ a standardized random variable normally distributed.

GOFs, estimated precision, AIC and BIC values were the main criteria used to evaluate the adequacy of the model.

3.4 Results

Model structure was defined and assessed first on average data and, then, the model was implemented and evaluated in the population context.

3.4.1 Evaluation of the model structure on average data

First of all, the PK/PD relationships between plasma or free tumor drug concentration and tumor growth kinetics were comparatively investigated on average data. To this aim, the model was identified on the average data using both C_{Plasma} and $C_{T,Periphery}$ as driver for the etoposide cytotoxic effect on tumor cells. Fitting results are shown in Fig. 3.1.

The dynamics of net body weight are excellent described in all the arms using both plasma and tumor concentrations. Comparing the tumor-free and the tumor-bearing untreated groups (Fig. 3.1, panels 1a vs 3a), it can be appreciated the huge impact of tumor progression on host (tumor-related chachexia): tumor-free animals growth almost 100g (one third of body weight) more than tumor-bearing animals. Furthermore, body weight profiles of the three treated groups (Fig. 3.1, panels 2a, 4a and 5a) show sharp decreases during the treatment period and the days immediately after its suspension. More in details, the comparison of the two tumor-free groups (untreated vs treated, Fig. 3.1, panels 1a and 2a) allows to evaluated the etoposide direct effect (drug related-cachexia). Conversely, body weight decreases in the two tumor-bearing treated groups (Fig. 3.1, panels 4a and 5a) are attributable to both drug effect on food assimilation and tumor mass progression: about 40g (22% of body weight) is the maximum weight loss in the 10 mg/kg-4 day arm and about 29g (15% of body weight) in the 5 mg/kg-8 day arm that appears to be the less impacting administration schedule. The goodness of the simultaneous fitting highlights the excellent model capability of describing, distinguishing and separating all the dynamics shown in the body weight data. First, due to the set of energy balance rules on which it is based, the model is able to describe host body growth and its slowdown in presence of tumor masses (panels 1a and 3a). Second, the inhibition of the en-

ergy intake driven by the effect compartment concentration enables the model to well explain the delayed body weight loss in tumor-free treated animals, attributable only to the etoposide toxic effect (panel 2a). In this way, also the simultaneous contributions of tumor-related and drug-related cachexia shown by the tumor-bearing treated groups (panels 4a and 5a) are correctly described and separated.

For what concerns the tumor dynamics, the unperturbed growth in the untreated arm (Fig. 3.1, panel 3b) is always well described. Conversely, results obtained on the tumor weight in the treated groups (Fig. 3.1, panels 4b and 5b) require a more extensive comment. The experimental regrowth curves show that the 8-days treatment with 5 mg/kg·day presents greater tumor growth inhibition (regrowth observed after 21.4 $\pm$ 1.1 day) compared with the 4-day treatment with 10 mg/kg·day (regrowth observed after 16.8 $\pm$ 0.8 day). Because the total administered dose (40 mg/kg) and the respective AUC are the same, it was supposed that etoposide has a schedule-dependent antitumor effect [44]. Even if the overall tumor growth inhibition is always sufficiently well described, when the cytotoxic activity is driven by the total plasma concentration (dashed lines in Fig. 3.1), the model is not able to fully capture the differences of the etoposide effects in the two different schedules. To support this, separated fittings in which one of the two tumor-bearing treated groups was keeping out (results not shown) were performed and different estimates for the parameter k_2 were provided: 7.17 mL/μg $\cdot$ day excluding the 5 mg/kg-8 day group and 8.7 mL/μg·day excluding 10 mg/kg-4 day group. Contrariwise, using free interstitial tumor concentration (solid lines in Fig. 3.1), tumor response is excellently described in both 5 and 10 mg/kg arms. Thus, intratumoral concentration seems correlate better with the etoposide inhibitory effect than total plasma concentration. Also AIC and BIC (1001.15 vs 940.97 and 993.73 vs 933.55 for plasma and tumor concentration, respectively) model selection criteria confirm the preference in using tumor concentration than plasma concentration.

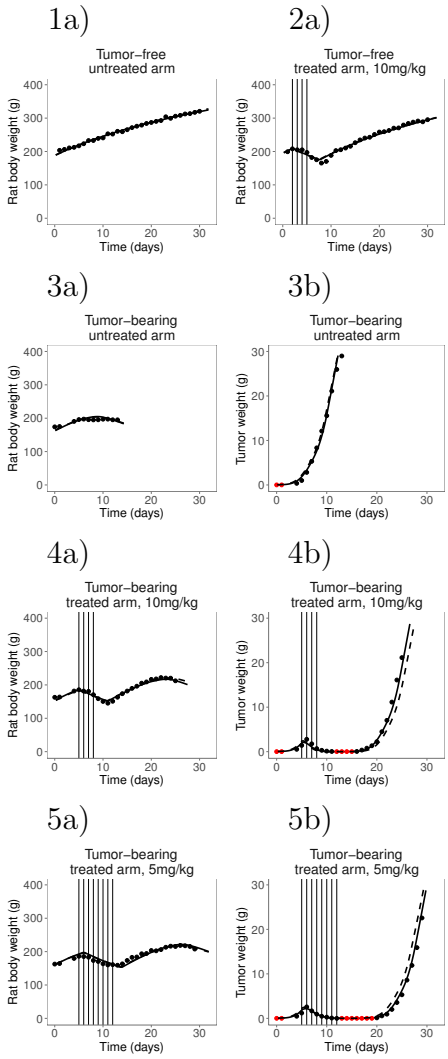

Figure 3.1: Plots with average observed (black dots), left censored (red dots) and model-fitted (lines) body weight and tumor growth curves in the five arms. In treated arms, model predictions considering interstitial free tumor or total plasma concentration as driver for the cytotoxic effect are reported with solid and dashed lines, respectively.

3.4.2 Population model on individual data

Once the model structure was assessed on the average data, a population model was developed as described in Section 3.3.3. Fitting results as well as model selection criteria confirmed previous findings: AIC was 8396.06 vs 8307.41 and BIC was 8435.38 vs 8346.71 for plasma and tumor concentration, respectively. Thus, intratumoral concentration was definitely selected as driver for etoposide cytotoxic effect. Individual fit plots are shown in Figs. 3.2 and 3.3, while the population parameter estimates are reported in Tab. 3.2 together with inter-individual and residual variability.

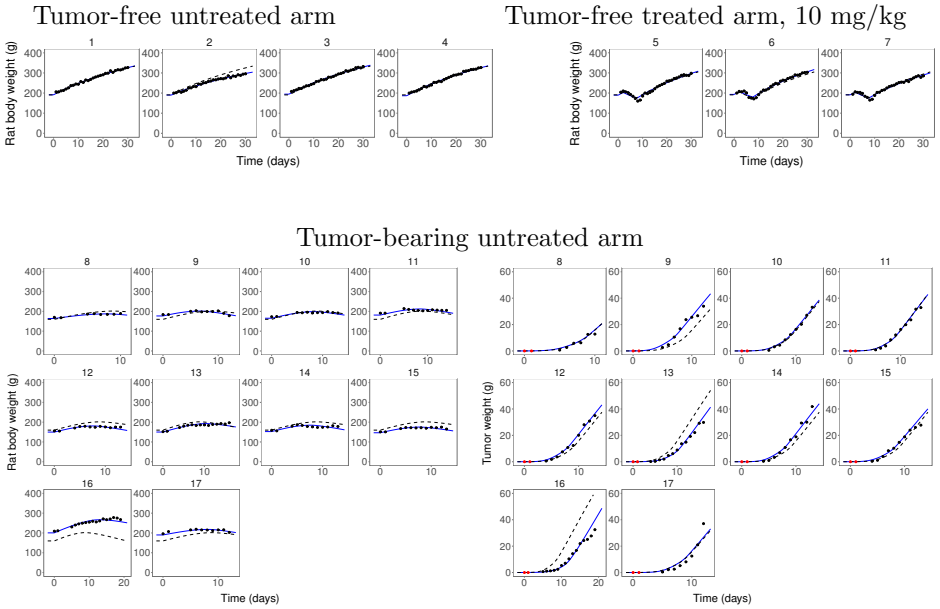

Figure 3.2: Plots with individual observed (black dots), left censored (red dots) and model-fitted rat body weight and tumor growth curves in the tumor-free arms. Individual and population model predictions are reported with solid and dashed lines, respectively.

The model is able to simultaneously grasp all the dynamics shown

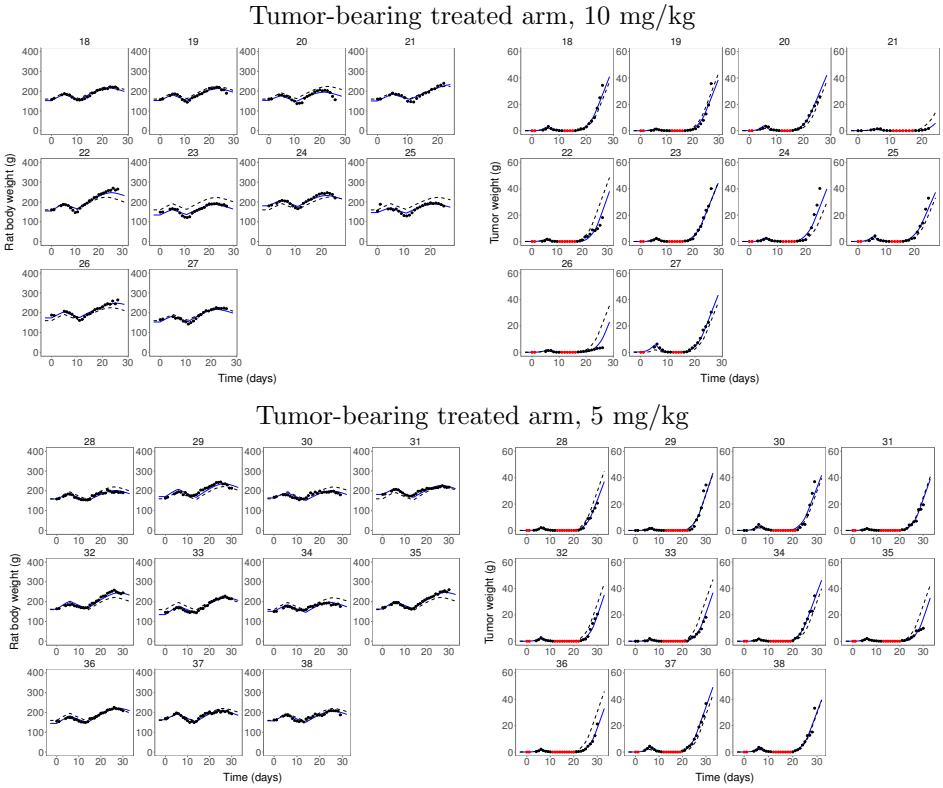

Figure 3.3: Plots with individual observed (black dots), left censored (red dots) and model-fitted rat body weight and tumor growth curves in the tumor-bearing treated arms. Individual and population model predictions are reported with solid and dashed lines, respectively.

by the five experimental arms: body weight growth in the tumor-free untreated animals, its slowdown in presence of tumor masses and body weight decreases due to the etoposide toxicity both in the tumor-bearing and tumor-free groups. Also tumor dynamics in the untreated and treated animals are adequately fitted by the model that is able to take into account schedule-dependence of the etoposide inhibitory effect. Moreover, individual predictions showed how, despite the inter-

individual variability was considered only for the initial conditions of the host (W_0, e_0), the inoculated tumor mass (V_{u10}) and the assimilation process (R_b), the experimental variability was appropriately described.

Table 3.2: Parameter estimates for the population DEB-TGI model.

Population parameters		
Parameter [Dimensions]	**Typical values, θ [RSE%]**	**Inter-individual variability, ω [RSE%]**
ν $[cm/day]$	0.284 [3]	-
$V_{1\infty}$ $[cm^3]$	436 [5]	-
g $[-]$	6.99 [14]	-
ξ $[-]$	0.765 [3]	-
ρ_b $[-]$	0.9408 [NA]	0.2165 [NA]
W_0 $[g]$	191 [3]	0.0869 [12]
β $[-]$	-0.178 [21]	-
e_0 $[-]$	1.46 [6]	0.246 [14]
μ_u $[-]$	30.9 [5]	-
g_u $[-]$	3.14 [3]	-
m_u $[1/day]$	0.0005 [23]	-
$IV_{u_{50}}$ $[cm^3]$	95.4 [33]	-
V_{u10} $[cm^3]$	0.0234 [13]	0.949 [18]
$\delta_{V_{Max}}$ $[cm^3/day]$	0.953 [8]	-
k_1 $[1/day]$	1.86 [4]	-
k_2 $[mL/\mu g \cdot day]$	24.1 [4]	-
k_{eff} $[1/day]$	0.671 [2]	-
$IC_{Eff_{50}}$ $[\mu g/ml]$	0.101 [2]	-
Residual variability		
b (W)	0.557 [2]	-
b (W_u)	0.729 [3]	-

Individual parameters are given by $P_i = \theta \exp(\eta_i)$ with θ the typical value and η a random effect normally distributed with zero mean and standard deviation $\omega(P)$. ρ_b and ω (ρ_b) were computed by approximation from estimates of $R_b = 0.0629$ (26%) and ω (R_b)= 1.22 (14%).

From Tab. 3.2 it can be observed that all the parameters were identified with good precision (RSE $\leq$ 33%). It is worth to note that estimates of the host-related parameters are in good agreement with the values obtained by van Leeuwen [59].

GOF plots, presented in Fig. 3.4, illustrate that the proposed population DEB-TGI model adequately described the collected experimental data. In Fig. 3.4, the weighted residuals are shown. Finally, VPCs (Fig. 3.5) confirm that the final model effectively explained the observed tumor and host body weights.

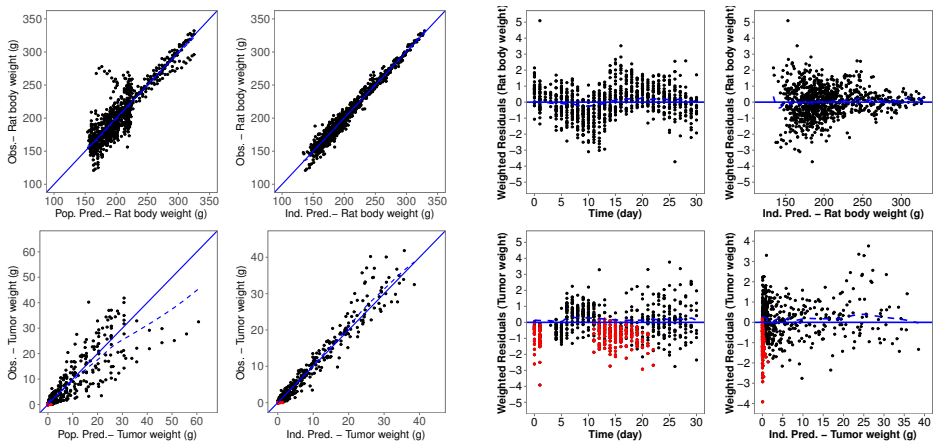

Figure 3.4: On the left, goodness-of-fit plots for the rat body weight (upper panels) and for the tumor weight (lower panels): solid and dashed lines indicate identity line and linear regression fit, respectively. On the right, residual plots for the rat body weight (upper panels) and for the tumor weight (lower panels): black dots are the data, red dots represent the left censored data.

3.5 Discussion

Starting from the tumor-in-host model presented in Chapter 2, a new population PK/PD model of cachexia onset and tumor growth inhibition following etoposide treatment in Wistar rats was developed. The excellent results allowed to affirm that, even if the DEB-based modeling approach was initially proposed to describe mice data, due to the use of species-dependent parameters, it resulted applicable also in experiments involving rat as target species.

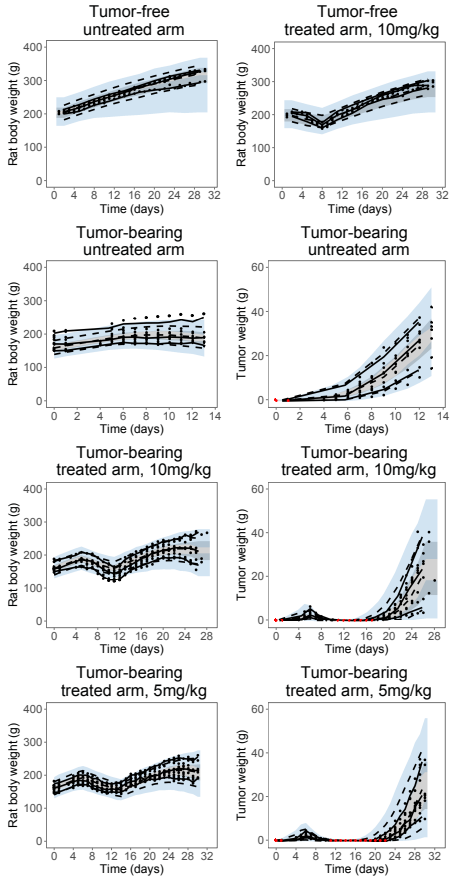

Figure 3.5: VPC plots stratified by group based on 1000 simulated replicates of the original data. The solid and dashed lines show the 10th, 50th and 90th percentiles of observed and simulated data, respectively; the shaded areas represent the 90% confidence interval for the corresponding model predicted percentile. The left censored data are indicated by the red dots.

More in details, the PK/PD model structure described in Chapter 2 was revised as follows. The assimilation process was supposed to be affected by two different and independent inhibition phenomena (Eq. 3.2): a reduction of food intake directly linked to tumor progres-

sion (tumor-related anorexia) and an energy inhibition due to the effect of etoposide treatment on the host (drug-related anorexia). In particular, a sigmoidal Imax model and an effect compartment for the drug plasma concentration were used to model the delay between the end of the treatment and the rat body weight regrowth (Eq. 3.2). Finally, both plasma and free peripheral tumor concentration were tested as driver for the etoposide cytotoxic effect on tumor cells (Section 3.4.1).

The adoption of a population technique allowed, for the first time, to describe individual behaviours accounting for and characterizing the heterogeneity of tumor-host interactions.

The resulting model was able to simultaneously describe the individual host body and tumor growth dynamics observed in tumor-bearing animals both for the treated and the control groups. At the same time, it was able to characterize body weight dynamics in tumor-free rats and the decreases following etoposide administration. Thus, the tumor-in-host growth, its inhibition after anticancer treatment, as well as the cachexia onset were taken into account by the model that was also able to discern body growth alterations due to the effect of tumor progression (tumor-related cachexia) from that of drug treatment (drug-related cachexia).

The unusual experimental design here adopted is worthy of further considerations. Indeed, developing a good experimental setting is of paramount importance because poorly designed experiments result in poorly supported conclusions [31]. In particular, defining the proper control groups could be extremely useful to consider all the possible factors that influence a correct estimation of the anticancer drug efficacy. For example, the presence of the two groups of tumor-free animals (treated with both placebo or etoposide) highlighted relevant dynamics often overlooked during preclinical studies. First of all, comparing the time course of the host body weight in the untreated tumor-free and tumor-bearing arms, the huge impact of the tumor progression on the animal condition (tumor-related cachexia) resulted

clear: tumor-bearing rats reached weights one third lower than tumor-free animals. This evidence underlines the key role that tumor-host energetic interactions seems to play in the *in vivo* tumor growth. Secondly, even if all the treated animals showed significant body weight losses due to the etoposide administration, only in the tumor-free arm this 'toxic' effect was purified from the influence that tumor had on the host growth (drug-related cachexia). Only the presence of the two tumor-free groups allowed to properly identify and discern the alteration of host assimilation attributable to the tumor progression and to the drug treatment. It is important to keep in mind that the selection of a suitable experimental design able to separately capture the several dynamics influencing *in vivo* tumor growth experiments and the availability of a model able to describe and discern each of them is crucial to obtain unbiased estimates of the anticancer efficacy of the drug and avoid confounding factors (see Section 2.4.2).

The good precision of the parameter estimates further confirmed that data coming from well designed experiments provide benefits in terms of parameter estimation and can contribute to solve the identifiability issues encountering in [61]. Moreover, the population approach, providing estimates of both the typical values and the inter-individual variability, allows, for the first time, to describe the tumor-host interactions on an individual level.

Finally, even if the use of plasma concentration is at the heart of traditional PK/PD models, plasma pharmacokinetics may not be sufficiently informative about the target site (active) concentrations. Indeed, the presence of necrotic areas, heterogeneous blood flow, high cell density and interstitial pressure may limit a homogeneous and adequate drug penetration into the tumor tissues [82]. In the specific case of etoposide, the PK study conducted by Pigatto et al. highlighted a higher penetration of the drug in the tumor periphery than in the central region and a saturable diffusion from plasma to tumor [76]. In this work, the use of free interstitial tumor concentration made the

model able to catch the schedule-dependence of etoposide inhibitory effect on tumor growth, differently from [44] in which an empirical Emax model had to be added on k_2 parameter.

Thus, we can conclude that only a mechanistic modeling approach, based on tumor-host energetic interactions, combined with the use of free intratumoral concentrations, could explain all the dynamics characterizing *in vivo* tumor studies and so provide a better understanding of the PK/PD relationships.

Chapter 4

A DEB-based modeling approach to anti-tumor activity and progressive resistance after anti-angiogenic therapy

Angiogenesis inhibitors are widely used for the treatment of cancer. The first marketed anti-angiogenic drug was bevacizumab (Avastin) but, later on, several different compounds entered the market of anticancer drugs. Differently from cytotoxic agents, angiogenesis inhibitors are not supposed to cause tumor cell death but to block oxygen and nutrient supplies to tumor cells decreasing, thus, their proliferation rate. For this reason, the DEB-TGI model presented in Chapter 2, basing on a direct cell kill hypothesis, is not applicable to anti-angiogenic therapies.

In this Chapter, a new DEB-based anti-angiogenic model describing the tumor growth modulation following cytostatic therapy is proposed and evaluated on xenograft experiments.

4.1 Background: the anticancer effect of the angiogenesis inhibitors

Angiogenesis, the development of new capillary blood vessels, plays a key role in the growth and progression of solid tumors [83]. Indeed, like normal tissues, tumor cells need an adequate supply of oxygen, metabolites and an effective way to remove waste products [84]. Tumors can actually cause this blood supply to form by giving off chemical signals that stimulate angiogenesis or by inducing nearby normal cells to produce pro-angiogenic molecules. Thanks to this dense vascular network, tumors ensure the amount of energy needed to proliferate. In a great number of cases, especially in advanced stages of cancer, the homoeostatic control of energy and protein balance is so compromised in favour of tumor to result in a dramatic loss of host body weight, attributable to the decreases of both skeletal muscle (biomass) and adipose tissue (energy reserve). In particular, depletion of skeletal muscle is a key component of cancer-associated cachexia and is responsible for increased chemotherapy toxicity, complications from cancer surgery, poor quality of life and mortality [56, 57].

In 1971, for the first time, Folkman proposed that anti-angiogenesis might be an efficacious anticancer strategy [85]. On the basis of this pioneering hypothesis, tumor angiogenesis became the focus of an extensive investigation that led to identify a wide variety of factors promoting tumor angiogenesis such as epidermal growth factor (EGF), transforming growth factor (TGF) and tumor necrosis factor (TNF) [86]. Among these numerous pro-angiogenic molecules, the most rele-

vant role is played by vascular endothelial growth factor (VEGF) [87].

Because tumors can not grow beyond a certain size or spread without an adequate blood supply, scientists have developed drugs called angiogenesis inhibitors, which block tumor angiogenesis. The goal of these compounds, also called anti-angiogenic agents, is not to directly hit tumor cells but to prevent or slow their growth by starving them or their needed blood supply. Angiogenesis inhibitors can interfere in different ways with the blood vessel growth process. Some of them are monoclonal antibodies that specifically recognize and bind to VEGFs preventing, so, their activation by receptors. Others directly bind to VEGF receptors as well as to other receptors on the surface of endothelial cells or to other proteins in the downstream signalling pathways, blocking their activities. Others again are immunomodulatory agents that stimulate or suppress the immune system that also have anti-angiogenic properties.

On February 2004, the U.S. FDA approved the first anti-angiogenic agent, bevacizumab (Avastin), a monoclonal antibody targeting the VEGFs, for the treatment of advanced colorectal cancer [88, 89]. Since then, an array of anti-angiogenic inhibitors were developed, tested in clinical trials and many of them got approved for the treatment of multiple cancers, alone or in combination with other cytotoxic/chemotherapy drugs [90, 91]. Despite the demonstrable efficacy of anti-angiogenesis targeted therapies in preclinical models and the increasing number of successful translations to clinic, a few major concerns remain in the anti-angiogenic approach for cancer treatment. Indeed, the introduction of anti-angiogenic therapy in clinic showed only limit transitory benefits and tumor responses much less significant than those expected from preclinical setting.

Mathematical models specially when based on physiological hypothesis and innovative data analysis approaches, could be extremely valuable for the preclinical efficacy assessment and its translation to clinics. Several models, employing a number of different techniques,

have been developed to describe tumor growth and its inhibition following the administration of anti-angiogenic agents given alone or in combination with cytotoxic drugs [48, 92, 93, 94, 95, 47, 46, 96]. Despite many of them have been successfully applied to analyse preclinical xenograft experiments involving anti-angiogenic target therapy, the tumor is always modeled as an independent entity and its interaction with the host organism is neglected.

The goal of angiogenesis inhibitors is to reduce the energy supply to tumor promoting the restoration of the energetic balance between tumor and host with the primary consequence of modulating tumor growth and secondary of improving cachexia condition. Hence, the tumor-in-host DEB-based model, directly accounting for the tumor-host energetic interaction, could provide a reasonable framework to describe tumor modulation followed anti-angiogenic therapy. However, the DEB-TGI model recently developed and presented in Chapter 2, based on a cell kill hypothesis, should not be, in principle, adequate to capture the specific mode of action of anti-angiogenic agents.

In this Chapter, the DEB-based approach has been adopted to describe the tumor growth modulation due to the cytostatic effect of anti-angiogenesis. In particular, a new tumor-in-host TGI model is here proposed and applied to analyse tumor and host body growth data collected during xenograft experiments involving bevacizumab (a known VEGF signalling inhibitor) and cetuximab (Erbitux), a monoclonal antibody biding the EGF receptors (EGFRs) involved in tumor angiogenesis. The integration of a hypoxia-triggered resistance mechanism accounted for the decreased efficacy during prolonged and enabled the model to predict the response to different administration schedules.

4.2 Anti-angiogenic experiments

4.2.1 Compounds

Bevacizumab (Avastin), a humanized anti-VEGF monoclonal antibody, and cetuximab (Erbitux), an IgG1 anti-EGFR monoclonal antibody, were used for the *in vivo* anti-tumor assessments.

4.2.2 Animals, tumor cell lines and *in vivo* tumor growth experiments

Fourteen female CD1 athymic Nu/Nu mice (6 weeks of age, 22-31g of weight), and one hundred and eleven male Balb athymic Nu/Nu mice (5-6 weeks of age, 21-36g of weight) were obtained from Harlan, S. Pietro al Natisone, Italy.

DU145 and Colo-205 cell lines were obtained from American Type Culture Collection (ATCC), HT29 cell line from European Collection of Cell Cultures (ECACC) and MX1 cell line from Cell Lines Service (CLS).

For all the studies, the experimental setting is the same described in Section. 1.3.1, in accordance with the best practices and ethic principles.

4.2.3 Treatments

The information about drug treatments are summerized in Tab. 4.1. In total eight different experiments involving 125 xenograft mice, four different tumor cell lines and two anticancer agents were considered. In particular, tumor weight data collected in the experiments *a*, *b*, *f* and *g* were already partially analyzed in [48], whereas the others are unpublished.

Table 4.1: Analyzed xenograft experiments.

	Cell line	Mice	Compounds	Dose	Route	N. of mice	Days of administration
Experiment a	DU145	male Bulb Nu/nu (6 weeks)	bevacizumab	10 mg/kg	i.p.	11	q4dx6 in days 5,9,13,17,21,25
				20 mg/kg	i.p.	11	q4dx6 in days 5,9,13,17,21,25
Experiment b	DU145	male Bulb Nu/nu (7 weeks)	bevacixumab	20 mg/kg	i.p.	8	q4dx6 in days 9,13,17,21,25,29
Experiment c	DU145	male Bulb Nu/nu (7 weeks)	bevacixumab	20 mg/kg	i.p.	8	q4dx6 in days 6,10,13,17,20,24
Experiment d	DU145	male Bulb Nu/nu (7 weeks)	bevacixumab	20 mg/kg	i.p.	8	q4dx4 in days 8,12,16,20
Experiment e	DU145	male Bulb Nu/nu (7 weeks)	bevacixumab	20 mg/kg	i.p.	8	q4dx3 in days 9,13,17
Experiment f	HT29	male Bulb Nu/nu (8 weeks)	bevacixumab	20 mg/kg	i.p.	7	q4dx4 in days 8,12,16,20
Experiment g	MX1	female CD1 Nu/nu (7 weeks)	bevacixumab	20 mg/kg	i.p.	7	q4dx4 in days 7,11,15,19
Experiment h	Colo-205	male Bulb Nu/nu (6 weeks)	cetuximab	1 mg/kg	i.p.	8	q4dx6 in days 7,11,14,18,21,25

4.3 Modeling approach

4.3.1 PK modeling

A one-compartment model with first-order absorption and elimination was used to generate average plasma concentration profiles for both the drugs. In particular, for bevacizumab, due both s.c. and i.p. administrations resulted to be characterized by complete bioavailability in mouse [97], mean PK parameters (ka=2.69 1/day, ke=0.115 1/day and V=0.119 L/kg) reported in literature for s.c. administration were used [98]. For cetuximab, the mean PK parameters (ka=10.344 1/day, ke=0.36 1/day and V=0.094 L/kg) estimated by Luo et al. for i.v. or i.p. administration in mice were used [99].

4.3.2 PD model stucture

The Tumor-in-host DEB-based model presented in Section. 2.2 was adopted to describe tumor and host growth in the untreated animals. Differently from the previous experimental setting in which the pharmacological effects of cytotoxic compounds were modeled through the inclusion of a mortality chain, here the effect of cytostatic treatments had to be considered.

Unperturbed tumor-in-host model

The tumor and host growth in the untreated group are modeled by the Sys. 2.20-2.22. As already assessed on rat data (Chapter 3), it is hypothesized that animals suffer from inappetence get aggravated with tumor progression. Thus, to account for the energy reduction linked to the presence of tumor masses (tumor-related anorexia), Eq. 3.1 is used to define the food-supply coefficient ρ.

Tumor-in-host DEB-TGI anti-angiogenic Model

Angiogenesis inhibitors are not supposed to directly cause tumor cell death (cytotoxic effect) but only to block tumor cell proliferation (cytostatic effect). Indeed, because blood flow provides the oxygen and nutrients that tumor mass needs to continue growing, energetic resources available to tumor strongly depend on its vascularization network. Moreover, independently from their specific mode of action and target molecules, the goal of angiogenesis inhibitors is to cut tumor blood supply off and, so, to deprive cancer cells of nutrients.

Thus, in case of anti-angiogenic treatment, the model hypothesizes that the reduction of tumor vascularization leads to an alteration of the energy partition between tumor and host with the specific aim of inhibit the energy frow to tumor. As the energy distribution is driven by the fraction $k_u(t)$, drug effect was implemented as an inhibitory I_{max} functionon $k_u(t)$:

$$k_u(t) = \frac{\mu_u V_u(t)}{V(t) + \mu_u V_u(t)} \left(1 - \frac{E_{max} c(t)}{IC_{50} + c(t)}\right) \tag{4.1}$$

where IC_{50} represents the drug concentration exerting the 50% of the maximal inhibitory effect, E_{max}. As expected, in absence of treatment, the partition function, $k_u(t)$, coincides with that of the untreated animals, Eq. 2.12.

In accordance with experimental data, none direct drug effect on the host organism is included. Indeed, the angiogenesis inhibitors here considered has been reported to not directly interact with host cells because they bind only to human VEGF or EGFR produced by tumor cells and not to mice VEGF and EGFR [98, 100]. Differently, considering species in which the anti-angiogenic agents are expected to be pharmacologically active (for example the cynomolgous monkey for bevacizumab [101]), some drug effects may be considered in the model.

4.3.3 Data analysis

PK/PD models were implemented in Monolix (version 2016R1) [80]. GOF plots were performed in R (Version 3.4.4) on graphic data exported from Monolix.

Plasma concentration-time profiles of bevacizumab and cetuximab were simulated using the PK models reported in Section. 4.3.1. Plots of the obtained plasma concentration profiles are reported in the Supplementary Material of Chapter 4.

For each experiment, tumor and mice net body weight data of control and treated groups were analysed simultaneously. First, the model structure was assessed on average data, then, a NLME approach was adopted allowing to describe both typical behaviour and inter-individual variability.

In this case, the absence of tumor-free animals did not allow to identify all the parameters simultaneously. Thus, host-related parameters (g, ν, $V_{1\infty}$, ξ, m, d_V) were kept fixed to estimates obtained from male and female mice growth data. For each experiment, values of the physiological parameters are reported in the Supplementary material of Chapter 4. In particular, for the studies involving Bulb Nu/nu mice the estimates already obtained in [61] were used. Differently, for Exp g, involving CD1 Nu/nu mice, new values were obtained.

In accordance with the general way to describe xenograft experiments, the inoculation day was considered as initial time instant, t_0. Thus, the initial condition for energy reserve, e_0, was determined through simulations considering mice age at the beginning of the experiment (values reported in the Supplementary Material of Chapter 4). Differently, W_0 and V_{u0} were estimated during model identification, while initial value of structural biomass, V_0, was derived from Eq. 2.10.

Furthermore, the thermodynamic efficiency coefficient, ω, was fixed to 0.75 and the density of tumor volume, d_{V_u}, to $1\,g/cm$.

Tumor-related (μ_u, g_u, m_u), cachexia-related ($\delta_{V_{max}}$, $IV_{u_{50}}$) and drug-related parameters (E_{max}, IC_{50}) were identified on mice and tumor weight data of control and treated arms for each experiment. After a preliminary model evaluation, the parameter E_{max} was fixed to 1 because the inclusion of its estimation in the identification step did not provide any relevant improvement in the model predicting capabilities.

To develop the NLME model, inter-individual variability was added on the initial conditions of host body weight and volume of inoculated tumor cells (W_0 and V_{u0}), on the half maximal inhibitory concentration (IC_{50}) and on the food-supply coefficient (ρ_b). Individual parameters P_i were supposed to be log-normally distributed. Moreover, the food-supply coefficient, ρ_b, was re-parametrized in terms of R_b and a log-normally distributed random effect was added on R_b.

The residual error model was supposed proportional to the square root of the predicted values (i.e. body or tumor weights), thus $y = f + b\sqrt{f}\epsilon$ where y is the measurement, f the predicted value, b a coefficient and ϵ a standardized random variable normally distributed.

4.4 Results

As in Chapter 3, model structure was defined and assessed first on average data and, then, the model was implemented and evaluated in the population context.

4.4.1 Average Data

For each experiments, the proposed model was simultaneously identified on average data of control and treated groups. Initially, the estimation of E_{max} was including in the identification step; however, this led to high uncertainty of parameter estimates without any relevant improvement in the model predicting capabilities.

For bevacizumab, results related to Exps d, f and g, involving three different tumor cell lines (DU145, HT29 and MX1) treated with the same schedule (20mg/kg q4dx4), were reported in Fig. 4.1 as representative examples. The time profile of the energy fraction $k_u(t)$ and of the assimilation coefficient $\rho(t)$ are reported for the control and the treated groups. Results for the remaining experiments, performed on DU145 cell line treated with a different number of bulus, are summarized in the Supplementary Material of Chapter 4.

The goodness of fits highlighted model capability to adequately describe the collected experimental data. In particular, tumor growth and its modulation following anti-angiogenic treatment was well fitted by the model that describes the drug effect as a reduction of tumor energy-supply (Eq. 4.1) without hypothesizes any direct killing effects. Furthermore, thanks to the set of energy balance rules on which the model is based, also the dynamics of mice body weight were well described in both the placebo and bevacizumab groups. In particular, comparing treated and control arms, it can be appreciated model capabilities to grasp the slowdown of the host body growth due to the tumor progression in control animals (tumor-related cachexia) and the

positive effect (lower body weight decrease) observed in treated animals due to the bevacizumab activity on tumor growth.

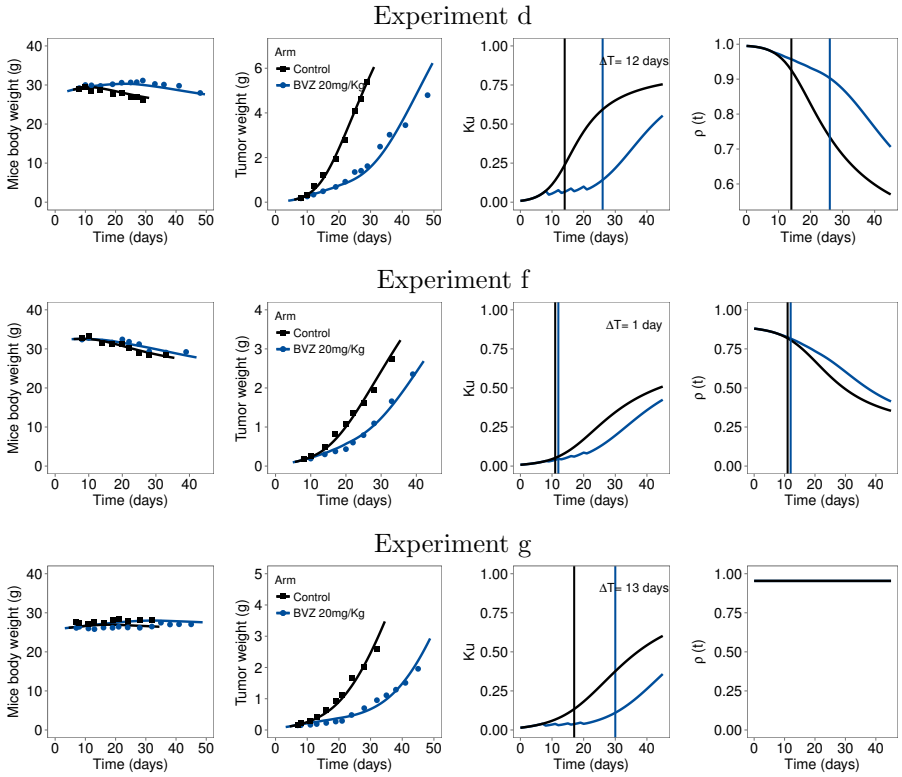

Figure 4.1: Plots with average observed (symbols) and model-fitted (lines) mice body weight and tumor growth curves obtained in the Exps. c, f and g for the placebo (black) and bevacizumab (blue) arms. Profiles of energy fraction k_u (vertical lines mark the $t_{\delta_{V_{Max}}}$ and DT represents the time delay between treated and control arms) and of assimilation coefficient ρ (for Exp f, treated and control groups overlapped) are reported.

For cetuximab, a comparison of plasma concentration and tumor dynamics in the treated arm showed a delay between the drug profile in plasma and the inhibition of tumor growth. Thus, an effect compartment was introduced and the effect-site concentration was used

to drive the inhibitory drug action. In this way, the model was able to adequately describe tumor and host dynamics following cetuximab administration Fig. 4.2. Also AIC (48.43 vs 40.67) and BIC (34.06 vs 26.3) criteria confirmed the advantage of introducing a delayed effect.

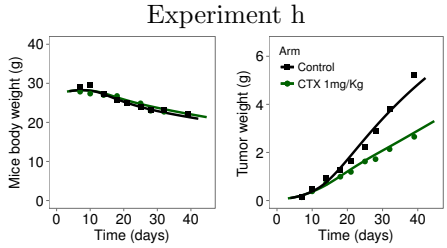

Figure 4.2: Plots with average observed (symbols) and model-fitted (lines) mice body weight and tumor growth curves obtained in the Exps. h for the placebo (black) and cetuximab (dark green) arms.

4.4.2 Population model on individual Data

Once the model structure was assessed on average data, a population approach was developed as reported in Section. 3.3.3. As an example, fitting results obtained for Exp. c are shown in Fig. 4.3, while all the other experiments are reported in Supplementary Material of Chapter 4. The obtained estimates of population parameters are presented in Tab. 4.2 together with inter-individual and residual variability.

The model was able to simultaneously grasp all the dynamics showed by experimental data: tumor growth and its slowdown after anti-angiogenic treatment as well as body weight decreases due to tumor-related cachexia were well described. Moreover, individual predictions showed how, despite inter-individual variability was considered only for few parameters, the experimental variability was appropriately described.

Table 4.2: Parameter estimates for the population DEB-TGI anti-angiogenic model.

Parameter [Dimensions]	**Exp a** (RSE%)	**Exp b** (RSE%)	**Exp c** (RSE%)	**Exp d** (RSE%)	**Exp e** (RSE%)	**Exp f** (RSE%)	**Exp g** (RSE%)	**Exp h** (RSE%)
Typical values								
W_0	26	23.2	28.1	27.7	27	34.2	27.1	30.7
$[g]$	(2%)	(3%)	(2%)	(2%)	(2%)	(3%)	(3%)	(2%)
ρ_b*	0.997	0.986	0.993	0.997	0.986	0.892	0.954	0.803
$[-]$	(NA)	(NA)	(NA)	(NA)	(NA)	(NA)	(NA)	(NA)
V_{u0}	0.01	0.015	0.017	0.023	0.022	0.0405	0.055	0.05
$[cm^3]$	(14%)	(15%)	(16%)	(11%)	(13%)	(16%)	(12%)	(20%)
μ_u	7.58	7.09	7.93	7.93	6.5	5.62	5.71	5.62
$[-]$	(3%)	(3%)	(4%)	(3%)	(5%)	(94%)	(4%)	(44%)
g_u	13.34	13.83	13.58	13.79	12.37	12.16	14.36	10.29
$[-]$	(0%)	(0%)	(1%)	(1%)	(6%)	(99%)	(2%)	(39%)
m_u	0.014	0.017	0.015	0.016	0.0132	0.021	0.012	0.014
$[1/day]$	(7%)	(0%)	(4%)	(3%)	(11%)	(99%)	(0%)	(43%)
$IV_{u_{50}}$**	10.1	-	11	12.1	12.8	2.96	-	1.75
$[cm^3]$	(2%)		(10%)	(5%)	(17%)	(64%)		(32%)
$\delta_{V_{Max}}$	0.016	0.016	0.013	0.011	0.016	0.083	0.01	0.112
$[cm^3/day]$	(1%)	(2%)	(2%)	(3%)	(6%)	(35%)	(105%)	(8%)
IC_{50}	3.29	2.22	2.76	1.31	0.966	4.12	1.74	0.072
$[\mu M]$	(19%)	(9%)	(23%)	(17%)	(13%)	(34%)	(21%)	(40%)
k_{Eff}	-	-	-	-	-	-	-	0.061
$[1/day]$								(52%)
Inter-individual variability								
ω (W_0)	0.097	0.095	0.091	0.089	0.061	0.081	0.117	0.043
	(16%)	(20%)	(19%)	(19%)	(23%)	(21%)	(20%)	(24%)
ω (ρ_b)*	0.004	0.152	0.769	0.464	0.55	0.183	0.175	0.978
	(NA)	(NA)	(NA)	(NA)	(NA)	(NA)	(NA)	(NA)
ω (V_{u10})	0.433	0.419	0.435	0.212	0.36	0.328	0.289	0.415
	(20%)	(21%)	(22%)	(33%)	(22%)	(23%)	(29%)	(23%)
ω (IC_{50})	0.515	0.21	0.597	0.452	0.342	0.406	0.462	0.596
	(27%)	(30%)	(27%)	(26%)	(29%)	(52%)	(28%)	(46%)
Residual variability								
b (W)	0.199	0.179	0.186	0.166	0.235	0.256	0.182	0.21
	(6%)	(7%)	(7%)	(6%)	(7%)	(7%)	(6%)	(6%)
b (W_u)	0.223	0.152	0.179	0.221	0.173	0.115	0.158	0.187
	(6%)	(7%)	(7%)	(6%)	(7%)	(7%)	(6%)	(7%)

Individual parameter are given by $P_i = \theta \exp(\eta_i)$ with θ the typical value and η a random effect normally distributed with zero mean and standard deviation $\omega(P)$. *Values of ρ_b and $\omega(\rho_b)$ were approximated from estimates of R_b and ω (R_b) reported in Supplementary Material of Chap.4. **In Exps b and f the estimates for $IV_{u_{50}} were$ so high that its inhibitory effect can be considered negligible. Thus, in these cases, ρ was set equal to the tumor-free constant ρ_b.

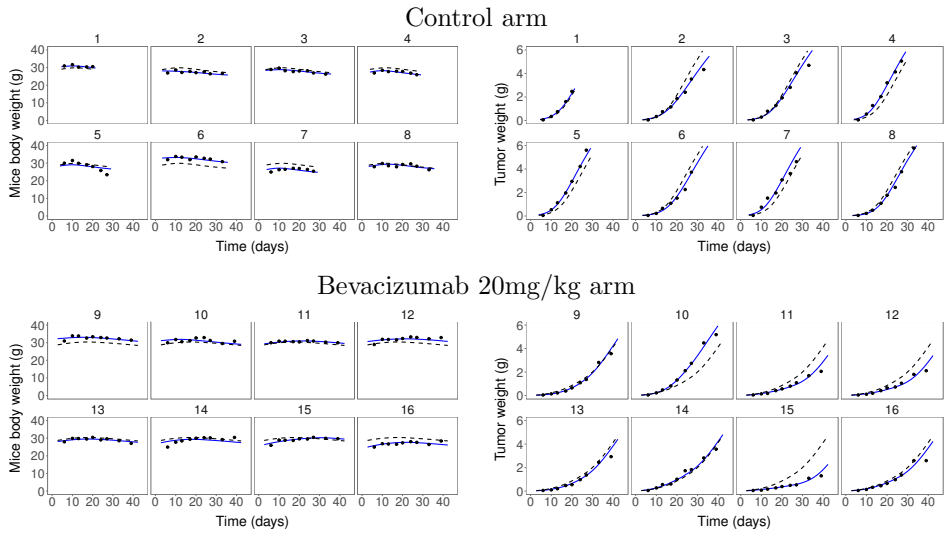

Figure 4.3: Individual fit plots for control and treated arms of Exp. c: black dots are the observed data, solid and dashed lines the individual and population model predictions, respectively.

From Tab. 4.2 it can be observed that model parameters were identified with good precision with a few exceptions for few parameters of experiment f that is characterized by a low number of subject and sampling times. Estimates of tumor-related and cachexia-related parameters are consistent among experiments a-e involving the same tumor cell line, DU145. Of interest, the values of IC_{50} increase with the duration of anti-angiogenic treatment. Furthermore, GOF plots (Fig. 4.4) show that the proposed population DEB-TGI model adequately described the collected experimental data; weighted residuals are randomly distributed around zero indicating the absence of model bias and, finally, VPCs confirm that the individual observed tumor and host body weights were effectively explained.

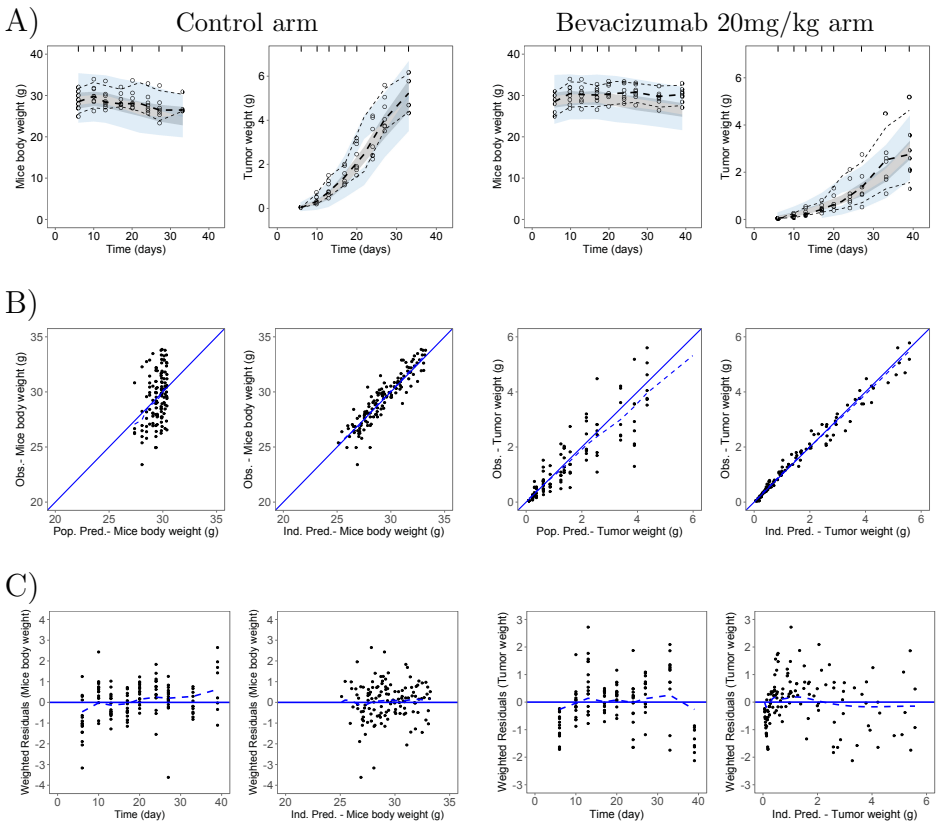

Figure 4.4: Panels A: VPC plots stratified by group (500 replicates of the dataset), dashed lines show the 10th, 50th and 90th percentiles of observed data, shaded areas represent the 90% confidence interval for the corresponding model predicted percentile, empty dots are individual observed data. Panels B: GOF plots for mice body (left panels) and tumor weight (right panels); solid and dashed lines indicate identity line and linear regression fit, respectively. Panels C: residual plots for mice body (left panels) and tumor weight (right panels).

4.4.3 Model Predictive Power

To further assess the predictive power of the proposed DEB-TGI anti-angiogenic model, data observed in Exp. a, in which bevacizumab was administered at 10 mg/kg or 20 mg/kg, were considered. Model

parameters were first identified on data relative to the placebo and to the lowest dose level (see Tab. 4.2 and fit plots reported in the Supplementary Material of Chapter 4) and, then, used (combined with the correspondent PK profile) to predict tumor and host dynamics in the 20 mg/kg arm. The agreement between predictions and observations, both considering average and individual data (Fig. 4.5), confirmed the predictive capabilities of the model and its potential use to correctly simulate new arms.

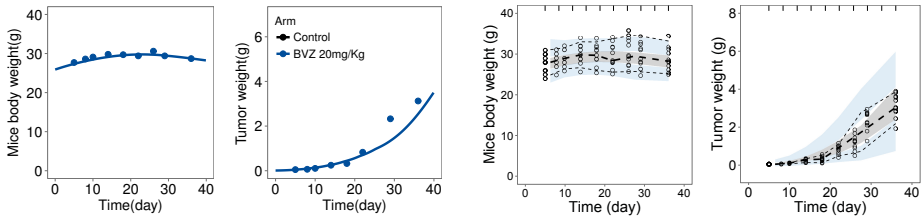

Figure 4.5: Model predicted mice body weight and tumor growth profiles relative to 20mg/kg bevacizumab arm of Exp. a. Average data on the left and individual data on the right (dashed lines show the 10th, 50th and 90th percentiles of observed data, shaded areas represent the 90% confidence interval for the corresponding model predicted percentile, empty dots are individual observed data).

4.5 Modeling resistance development to bevacizumab on DU145 cell line

Previous results show how the proposed DEB-based TGI model excellent describe the activity of anti-angiogenesis inhibitors in xenograft mice. In particular, anticancer drug activity is modeled by an inhibition function parametrized using IC_{50} which value encloses information about compound potency. Indeed, we can consider $1/IC_{50}$ as an indicator of the average potency of drug treatment.

In this section, the mechanistic approach at the basis of the anti-angiogenic TGI model is exploited to investigate and formulate realistic hypothesis about the development of resistance to bevacizumab in DU145 tumor cell line. Even if the lack of adequate experimental information did not allow an extensive investigation, literature data confirmed the plausibility of the obtained results.

4.5.1 Evidence from experimental data and model results

The availability of experiments in which different durations of bevacizumab therapy were tested on tumor cell line DU145 (Exps. a-e) provided the opportunity for some further considerations. Indeed, experimental data showed that doubling the length of bevacizumab treatment (from 20mg/kg q4dx3 to q4dx6) did not result into greater tumor growth inhibition. From the comparison of the average tumor profiles (Fig. 4.6), it is evident that the unperturbed tumor growth in the placebo groups are almost super-imposable and effected by a very low inter-experiment variability. Furthermore, despite the number of bolus varying from 3 to 6, no significant differences in the overall inhibitory effect is shown by the treated arms.

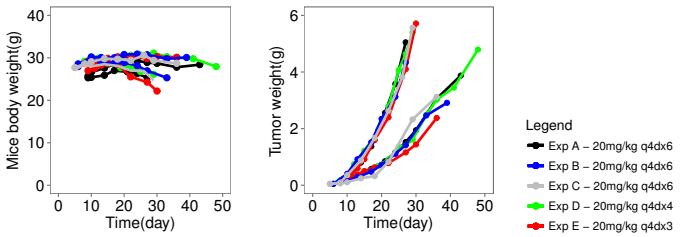

Figure 4.6: Spaghetti plots of the average mice body and tumor weight for Exps. a-e, involving tumor cell line DU145.

According to experimental data, obtained values for the tumor-

related parameters did not differ significantly between the studies on DU145 cell line. Moreover, the model estimates of the the average bevacizumab potency, $1/IC_{50}$, decrease with the increasing of therapy duration (see Tab. 4.2).

To assess that the discrepancies in the IC_{50} estimates actually reflect a difference of the overall potency between the different administration protocols, tumor weight profiles of the Exp. b were simulated using parameter estimates obtained on the appropriate experimental data and the IC_{50} values of Exps. d and e (Fig. 4.7). As can be appreciated, model predicts an over-estimation of the inhibitory effect on tumor weight when drug potency estimated on q4dx4 or q4dx3 bevacizumab experiments was used to simulate tumor response to q4dx6 bolus of bevacizumab.

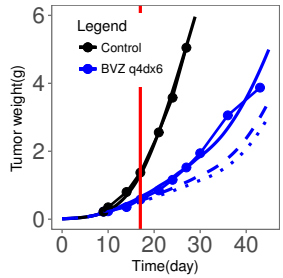

Figure 4.7: Model simulations of the average tumor weight for Exp. b performed using parameters obtained on Exp. b (solid lines) and changing the IC_{50} value to the estimates obtained on Exp. d (dashed lines) and and Exp. e (dotted lines). Red vertical line marks the third administered bolus.

4.5.2 Adaptive resistance arising: the hypoxia hypothesis

From the previous considerations, we supposed that, efficacy of prolonged anti-angiogenic administration was prejudiced by the arising of some resistance mechanisms. Literature data confirmed the

plausibility of this hypothesis: apparent resistance to angiogenesis inhibitors was deeply described both in clinical and preclinical settings [102, 103, 104, 105, 106, 107, 108, 109]. In particular, the development of non-responsiveness to an initially efficacious anti-VEGF therapeutic regimen was clearly documented in xenograft models [110, 111, 109]. Current experimental evidence suggests that tumors can adapt to the presence of VEGF-target agents acquiring different adaptive mechanisms to functionally evade the therapeutic blockade of angiogenesis [102, 106, 110, 112, 107]: activation and/or up-regulation of alternative pro-angiogenic signalling pathways within the tumor, recruitment of bone marrow-derived pro-angiogenic cells and increased pericyte coverage of tumor vasculature. Activation of alternative pro-angiogenic signalling, independent from VEGF, was revealed in pancreatic cancer mouse model [110]: after an initial response phase (10-14 days), tumors started regrowing and the typically dense tumor vasculature was restored. Notably, the VEGF-blockade persist during all the study and tumors had regions of acute hypoxia, a known inducer of angiogenic responses in a wide variety of cancer types [113, 109].

Based on these information, we supposed that during the longer anti-angiogenic therapy, the aggravated tumor hypoxia, combined with the persistent VEGF-blockade, triggered a VEGF-independent tumor re-vascularization and, led to a consequence lower effectiveness of bevacizumab therapy.

4.5.3 Model of hypoxia-triggered resistance

It was hypothesized that the aggravation of tumor hypoxia over a critical threshold $\bar{H}$ triggered a VEGF-independent tumor re-vascularization and, consequently, led to a lower effectiveness of bevacizumab therapy. From a modeling point of view, first, the expected hypoxia condition imputable to the VEGF-blockade, H, was defined as:

$$H(t) = \frac{\int \frac{\mu_u V_u(t)}{\mu_u V_u(t) + V(t)} \frac{E_{max} C(t)}{IC_{50} + C(t)} dt}{\int \frac{\mu_u V_u(t)}{\mu_u V_u(t) + V(t)} dt}, \tag{4.2}$$

that is the ratio between the energy not absorbed by the tumor due to drug effect (in the hypothesis of a VEGF-dependent tumor angiogenesis) and the energy absorbable in absence of anti-angiogenic therapy. Then, when $H(t)$ exceeds a critical threshold $\bar{H}$, the maximum effect of the VEGF-blockade induced by bevacizumab is reduced. Thus, in Eq.4.1 the E_{max} parameter is redefined as:

$$E_{max_{Inhib}}(t) = \begin{cases} E_{max} & \text{if } H(t) \leq \bar{H} \\ E_{max} e^{k_H(\bar{H} - H(t))} & \text{if } H(t) > \bar{H}. \end{cases} \tag{4.3}$$

and consequently

$$k_u(t) = \frac{\mu_u V_u(t)}{V(t) + \mu_u V_u(t)} \left(1 - \frac{E_{max_{Inhib}} c(t)}{IC_{50} + c(t)}\right). \tag{4.4}$$

4.5.4 Data analysis and results

The hypoxia-triggered resistance model was evaluated on the Experiments b, d and e in which 20 mg/kg bolus of bevacizumab were administered q4dx6, q4dx4 and q4dx3, respectively, from day 8 or 9 since the inoculation.

First of all, average data were simultaneously identified with the DEB-TGI anti-angiogenic model: estimates for host-related and tumor-related parameters matched those of separated fittings and a common value of IC_{50} was found to be 1.31 μM. However, the profiles of tumor weight in treated arms (blue curves in Fig. 4.8) showed a slight

over-estimation of the inhibitory effect in Exp. b (with the longest treatment period) and a under-estimation in Exp. e (with the shorter treatment period).

Then, the DEB-TGI anti-angiogenic model integrated with the hypoxia-mediated resistance description was identified against the same set of experiments. The inclusion of the hypoxia-triggered resistance mechanism made enable the model to describe the decreasing efficacy of prolonged bevacizumab therapy (red profiles in Fig. 4.8). Also AIC (200.79 vs 215.54) and BIC (215.54 vs 213.45) model selection criteria confirmed this evidence.

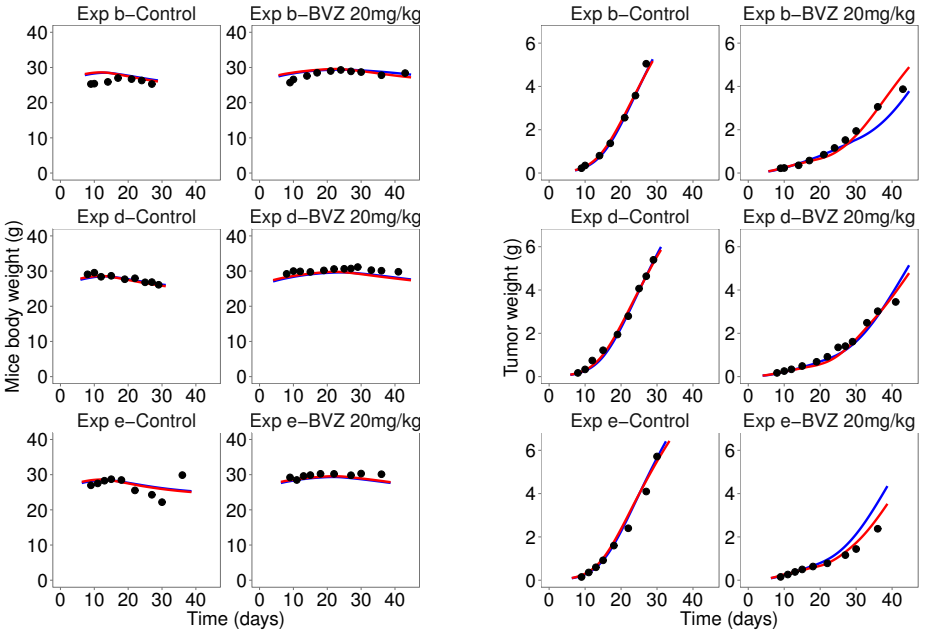

Figure 4.8: Plots with average observed (symbols) and model-fitted (lines) mice body weight and tumor growth curves obtained in Exps. b, d and e for the placebo and the bevacizumab treated arms. Model predictions obtained including or not the hypoxia-mediated resistance model are reported in red and blue, respectively.

Once the resistance model was assessed on average data, a population model was developed to analyse individual data. In particular, log-normally distributed random effects were included on parameters W_0, V_{u0}, R_b and IC_{50}. However, adding inter-individual variability on the drug potency parameter led to unreasonable estimates, so it was removed from the model. Moreover, to account for the differences between experiments, a categorical covariate "Experiment" was added on the typical value of W_0, V_{u0}.

The obtained parameter estimates and VPC plots are reported in Tab. 4.3 and in Fig. 4.9, while the other diagnostic plots are included in the Supplementary Material of Chapter 4.

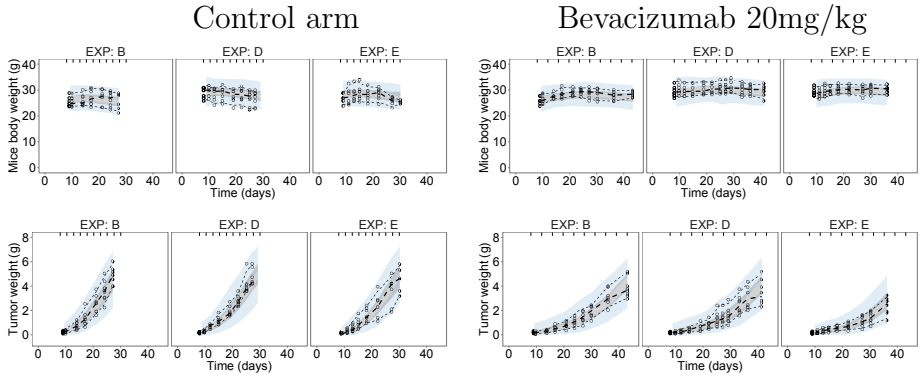

Figure 4.9: VPC plots stratified by group and experiment (500 replicates of the dataset): dashed lines show the 10th, 50th and 90th percentiles of observed data, shaded areas represent the 90% confidence interval for the corresponding model predicted percentile, empty dots are individual observed data.

The obtained results show that, with the integration of a hypoxia-mediated resistance mechanism, the model was able to capture the decreased efficacy affecting prolonged therapy. In agreement with literature data, in which a response phase of 10-14 days was documented [102], the hypoxia condition remains below the threshold $\bar{H}$

($E_{Max} = 1$) for a period of about 11 days. Accordingly, the estimated IC_{50} value, 0.95 μM, resulted very closed to that previously observed in Exp e characterized by the shortest treatment of bevacizumab. Furthermore, the model was able to account for inter-individual variability showed by treated tumors without the need of random effect on IC_{50} parameter. This could mean that a modulation of drug efficacy on the basis of hypoxia condition is able, alone, to catch inter-individual variability of tumor response to anti-angiogenic treatment.

Table 4.3: Parameter estimates for the hypoxia-triggered resistance DEB-TGI model.

Population parameters		
Parameter [Dimensions]	**Typical values, θ [RSE%]**	**Inter-individual variability, ω [RSE%]**
W_0 (Exp e) $[g]$	25.7 [3]	0.109 [11]
β_{W_0} (Exp b) $[-]$	0.054 [40]	-
β_{W_0} (Exp d) $[-]$	-0.101 [74]	-
e_0 $[-]$	1.27 [fixed]	-
ρ_b $[-]$	0.993 [NA]	0.002 [NA]
V_{u10} (Exp e) $[cm^3]$	0.021 [18]	0.283 [96]
$\beta_{V_{u10}}$ (Exp b) $[-]$	0.534 [38]	-
$\beta_{V_{u10}}$ (Exp d) $[-]$	0.034 [>100]	-
μ_u $[-]$	6.33 [3]	-
g_u $[-]$	13.34 [1]	-
m_u $[1/day]$	0.013 [4]	-
IV_{u50} $[cm^3]$	16.3 [12]	-
$\delta_{V_{Max}}$ $[cm^3/day]$	0.014 [73]	-
IC_{50} $[\mu M]$	0.95 [1]	-
k_H $[-]$	2.49 [21]	-
$\bar{H}$ $[-]$	0.371 [9]	-
Residual variability		
b (W)	0.2 [4]	-
c (W)	0.5 [fixed]	-
b (W_u)	0.237 [4]	-
c (W_u)	0.5 [fixed]	-

Individual parameters are given by $P_i = \theta \exp(\eta_i)$ with θ the typical value and η a random effect normally distributed with zero mean and standard deviation $\omega(P)$. ρ_b and ω (ρ_b) were computed by approximation from estimates of $R_b = 0.007$ (37%) and ω (R_b) =0.286 (96%).

Once established, the hypoxia-triggered resistance model can be

used also as a tool for exploring the expected tumor and host responses to different administration protocols accounting for the resistance effect. In particular, continuous or intermittent schedules, whose convenience is still under debate in literature, can be evaluated. For example, considering the DU145 cell line, tumor-in-host response at 20mg/kg bolus q4dx6, or q4dx3 for two cycles, or q4dx2 for three cycles, were simulated and reported in Fig. 4.10. In panel A, the comparison of the tumor profiles predicted by the model with or without hypoxia provides a clear view of the negative effect of hypoxia in case of continuous repeated administration. In panel B, a positive indication towards the use of the intermittent schedules seems to be present.

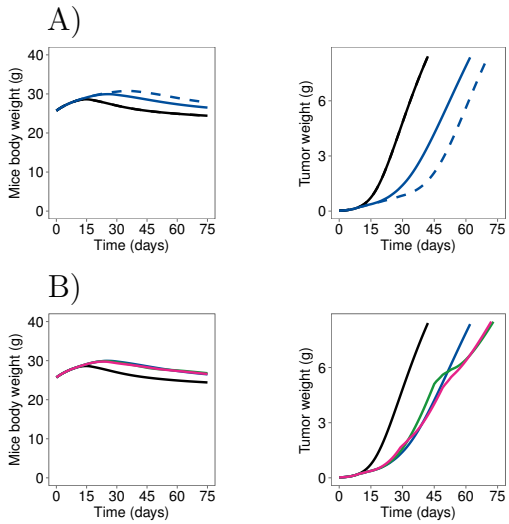

Figure 4.10: Panel A: tumor and mice net body weight predicted by the model with (solid blue line) or without (dashed blue line) the hypoxia-resistance mechanism following the administration of 20mg/kg bolus q4dx6; black line showing control group. Panel B: tumor and mice net body weight predicted by the hypoxia-resistance model after the administration of 20mg/kg bolus q4dx6 (blue), q4dx3 for two cycles (green), or q4dx2 for three cycles (magenta).

Finally, the hypoxia-triggered resistance model was evaluated also on literature data relative to patient-derived CRC xenograft mice

treated with bevacizumab [108]. In this experiment the antiangiogenic agent was administered twice-a-week at 5mg/kg for a treatment period of 30 days, 50 days, 30 days followed by 20 days without treatment, 70 days or 70 days-treatment with a drug-break period between day 30 and 50. The tumor-related parameters were estimated from the experimental data whilst the hypoxia-triggered resistance model here developed on DU-145 cell line was used to predict CRC tumor response to bevacizumab treatment. As documented by model simulations reported in the Supplementary Material of Chapter 4, our DEB-TGI model integrated with the hypoxia-resistance mechanism was able to adequately predict tumor response at the different administration schedules, showing its good potentialities as prediction tool of bevacizumab anticancer effects.

4.6 Discussion

In this work, a new PK/PD model of tumor growth inhibition following anti-angiogenic treatment in xenograft mice was developed on the basis of the tumor-in-host DEB-based approach described in Chapter 2.

The proposed model was successfully tested on eight preclinical experiments performed for the *in vivo* anti-tumor assessment of two marked agents: the anti-VEGF monoclonal antibody bevacizumab, tested on three different tumor cell lines, and cetuximab, an anti-EGFR monoclonal antibody studied on Colo-125 tumor line. Results highlighted the good model capability in describing and predicting the dynamics of both tumor and host net body weight in control and treated xenograft mice after the administration of anti-angiogenesis inhibitors. Differently from other standard PK/PD models completely focused on the evaluation of the antitumor efficacy [48, 46, 94, 95], the present approach, thanks to its physiological hypothesis, provides ad-

ditional information on various animal clinical outcomes such as body weight, energy-intake and assimilation (anorexia), tumor-host energy distribution and degradation process of structural biomass (cachexia).

More in details, PK models were obtained from literature [98, 99] and used to simulate plasma concentration profiles. The unperturbed tumor-in-host growth was described through the tumor-in-host model presented in Section. 2.2 with the integration of the food supply reduction, directly linked to tumor progression (Eq. 3.1), to model the negative influence that tumor growth itself exerts on host energy intake (tumor-related anorexia). In particular, the parameter IV_{u50} could provide a quantitative measure of tumor-related anorexia and could be extremely useful to compare its severity among different tumor cell lines, anticancer drugs or anti-cachectic compounds. For example, comparing the three tumor cell lines involved in Exps a-g, all the experiments on DU145 cell line showed $IV_{u_{50}}$ higher than 10 cm^3 (10.1-12.8 cm^3 or higher for exp. b) corresponding to a 10% reduction of the energy supply in presence of tumor volumes of around 1.5 cm^3. Interestingly, a different behaviour was observed in the other two cell line, MX1 and HT29. In the first case, no significant host body weight decrease followed tumor growth and, accordingly, the estimate of $IV_{u_{50}}$ was so high to result unidentifiable. On opposite, for HT29 tumor cell line, $IV_{u_{50}}$ was about 3 cm^3, providing a strong energy reduction of about 35% for a tumor mass of 1.5g. The strong body weight losses observed in the control animals of experiment f (more than 15% of BW in a three week period) confirmed the severity of this effect and suggested a possible higher impact of tumor-related anorexia in case of a gastric line, as HT29, in comparison of other lines [56, 57].

In addition to the inhibition of host assimilation due to tumor progression, the mechanistic approach of the model allows to extrapolate also the time course of energy distribution within the tumor-host system (Fig. 4.1). This is governed by the $k_u(t)$ function that, at any time instant, represents the fraction of energy exploited to the host by the

tumor. From Eq.2.12 it follows that the amount of energy assigned to the tumor or to the host biomass depends on their corresponding volumes (V_u and V), whilst the parameter μ_u determines the weights of the two components for unit of volume. For this reason, the parameter μ_u can be considered a measurement of tumor aggressiveness, understood to mean capabilities of sustaining tumor vascularization and, thus, growth. Considering all the experiments here analyzed, μ_u values in the 5.62-7.93 range were observed, thus, for body mass volume of 30 cm^3 and tumor volume of 1.5 cm^3, about 25-35% of the available energy is delivered to the tumor instead of the expected 5% if $\mu_u = 1$.

The contribution of both tumor-related anorexia and tumor-host energy distribution determined the tumor impact on host body weight. For its evaluation, the product of the assimilation coefficient, $\rho(t)$, and the fraction 1-$k_u(t)$ could be extremely useful.

In case of anti-angiogenic treatment, the drug activity limits the energy delivery to the tumor and, thus, counteracts the energetic unbalance between tumor and host. Coherently, the Eq.2.12 for the $k_u(t)$ fraction was modified adding a I_{max} inhibitory function, parametrized in terms of IC_{50} (Eq.4.1) that provides a measurement of drug potency. For example, IC_{50} estimates for bevacizumab are different for the three tumor cell lines; this variable magnitudine of inhibition depends on the human/mouse VEGF ratio that could varying with tumor line [89]. Interestingly, the ranking obtained for Exps. b, f and g, involving the three lines DU145, HT29 and MX1, is the same of that obtained with the Rocchetti model [48].

In addition to the information provided by the IC_{50} parameter estimates, further considerations about the drug potency can be obtained considering the biomass degradation process. In particular, the time $t_{V_{Max}}$, at which this process reaches its maximum rate, $\delta_{V_{Max}}$, represents a meaningful index of cachexia severity. Hence, the time delay, $\Delta t_{V_{Max}}$, observed between treated and control groups provides an addi-

tional quantitative measure of the drug activity on energy distribution (see Fig. 4.1).

As a further consideration, we can observed that in the bevacizumab treated groups the PD effect of the drug was directly linked to plasma concentration levels. This means that there is not delay between drug kinetics in plasma and its effect on tumor vascularization. Otherwise, based on the biology of tumor angiogenesis, some delay might be expected as the formation of the micro-vessel network requires time. For bevacizumab the inclusion of a delay in the model was not necessary, possibly because its very slow disposition (the half-life in mice is almost one week) may represent the overall rate-limiting step. Conversely, for cetuximab a delay compartment was needed; this difference could be due to the faster disposition of cetuximab or to an actual delay between plasma concentration dynamics and the inhibition of tumoral EGFR, as documented in [99].

Furthermore, results obtained on DU145 tumor cell line highlighted a decrease of bevacizumab efficacy for prolonged treatments, phenomena widely documented both in preclinical and clinical setting. Even if the lack of adequate experimental information did not allow further investigations, based on literature data the arising of an adaptive evasive resistance was hypothesized. More in details, we supposed that prominent vessel pruning and excessive inhibition of new vessel growth by bevacizumab treatment induced tumor hypoxia. The hypoxia condition, up-regulating alternative pro-angiogenic signalling pathways, led to a VEGF-independent re-vascularization. Thus, a hypoxia-triggered resistance model was developed and integrated in the DEB-TGI anti-angiogenic model, allowing to describe the decreased efficacy of prolonged bevacizumab therapies. Moreover, the modulation of the inhibitory drug effect on the basis of the hypoxia condition allowed to catch inter-individual variability of tumor response to the treatment.

In summary, the tumor-in-host DEB-based framework was extended to account for the effect of anti-angiogenic treatments. Its mechanis-

tic approach, based on a set of energetic tumor-host interaction rules, not only allowed to excellent describe the activity of anti-angiogenesis inhibitors in xenograft mice but also to investigate and formulate realistic hypothesis on the complexities of resistance to bevacizumab.

Chapter 5

Testing additivity of combined anti-angiogenics with chemotherapy: a tumor -in-host modeling approach

Angiogenesis inhibitors, due to their specific mode of action, are particularly suited for combination with different anticancer therapies, such as chemotherapy and radiotherapy. For this reason, already in the preclinical setting, specific combination experiments are performed in order to evaluate if a concomitant therapy of chemotherapeutics and antiangiogenics show an enhanced antitumor activity. However, the efficacy of these combinations is variable and apparently, strongly dependent on the administration schedule. In this scenario, the application of model-based methodologies able to evaluate *in vivo* PD drug-drug interactions could be extremely relevant to recognize synergisms or antagonisms and to understand the dynamic interactions between

tumor progression, anti-angiogenesis inhibitors and chemotherapeutic drugs.

Starting from the DEB-TGI models previously developed for anti-angiogenic and cytotoxic agents given as monotherapy, a new tumor-in-host approach to analyse combination experiments is proposed. A xenograft study concerning the administration of bevacizumab in combination with NMS-937H, a Polo-Like Kinase 1 (PLK1) inhibitor, is analyzed as illustrative example.

5.1 Combinations of anti-angiogenics with chemotherapy

The use of combination therapies (administration of two or more different drugs) has become a widely adopted strategy in the cancer treatment, thanks to its advantages over single agent administrations. Indeed, drug cocktails can provide a more flexible therapy, characterized by a better response and a reduced toxicity, due to the possibility of attacking the tumor through different biological pathways at the same time. In particular, as antiangiogenics are generally cytostatic rather than cytoreductive, combinations involving conventional cytotoxic or targeted chemotherapies may be useful to maximize the therapeutic activity. As a consequence, interactions between anti-angiogenic drugs and anticancer agents inducing tumor cell kill have been often evaluated in many preclinical and clinical studies raising a considerable debate about their possible advantages [114].

Several studies have suggested that combining anti-angiogenic drugs, such as the anti-VEGF antibody bevacizumab, with chemotherapy may result in synergistic antitumor activity. One likely mechanism underlying this synergism is the functional normalization of the chaotic tumor vasculature following the anti-angiogenic therapy that is tran-

sient and can potentiate the activity of coadministered chemotherapies [115, 116]. In addition, the activity of anti-angiogenic drugs can be enhanced by cytotoxic treatments. For example, chemotherapy can augment the sensitivity of tumor blood vessels to VEGF inhibition, which leads to increased antitumor effect in the combination therapy setting [117].

In contrast to the normalization hypothesis and the expected increase in the delivery of chemotherapy to tumor, it has also been reported that chronic angiogenesis inhibition leads to an increased vascular damage and to a subsequent decrease in cytotoxic drug exposure.

Schedule of administration could be the key factor of these conflicting results [118, 115]. Antiangiogenic therapy may initially normalize the abnormal tumor blood vessels, thereby improving delivery of oxygen and chemotherapy. However, this window of opportunity, wherein cytotoxic agents will have maximal access to cancer cells, is only transitory. Thus, suboptimal scheduling of administration may lead to antagonism between cytotoxic and anti-angiogenic therapies. Alternately, in some cases, the strong and independent antitumor effects of the anti-angiogenic drugs can more than compensate for the decrease in cytotoxic drug exposure, leading to an increased overall antitumor activity [118].

In this scenario, already the simple qualitative classification of the drug interactions in the three groups, synergistic, additive or antagonistic, is not easily and largely discussed. Finding the most effective drug cocktails and optimizing doses and schedules in combination regimens are more challenging tasks. How mathematical modeling can address these issues is not an new question and different modeling approaches have been proposed to quantify and predict the impact of anti-angiogenesis combined with chemotherapy on tumor growth dynamics [48, 46, 119, 120].

An interesting approach is that proposed by Rocchetti et al. in [51] for combinations of two or more cytotoxic agents and, then, adapted

for the administration of bevacizumab combined with chemotherapy [48]. Indeed, starting from an additive model in absence of drug-drug interaction was proposed and used to assess the nature of drug combination. In particular, the simulations obtained by the no-interaction model are compared with the experimental data of the combination therapy; the validity of the zero-interaction hypothesis is, then, evaluated by visual assessment and a statistical test. Therefore, the model is able to predict the tumor growth inhibition in case of an additive effect, whereas any synergistic or antagonistic behaviours are derived from departures of the experimental data from the predictions and can be, then, easily integrated in a combination model [48].

In this Chapter, adopting the same strategy proposed by Rocchetti et al. [51], the tumor-in-host DEB-based approach previously developed was extended and applied to the more complex framework of the preclinical combination studies. An illustrative example of its application of a real case study is, also, presented.

5.2 Modeling approach to combination experiments

5.2.1 Model structures

The Tumor-in-host DEB-TGI models for the single agent arms

Tumor and host body growth in the untreated group are described by the Tumor-in-host DEB-based model introduced in Chapter 2 (panel A in Fig. 5.1). The model is characterized by the Sys. 2.20-2.22 with the addition of the Eq. 3.1 to account, also, for the aggravation of tumor-related cachexia during cancer progressions.

For what concerns animals treated with angiogenesis inhibitors,

assuming a reduced vascularization and, then, a reduced nutrient supply to the tumor, the anti-angiogenic action is implemented as an inhibitory effect on the energy fraction $k_u(t)$ appropriated by the tumor to the host (panel B in Fig. 5.1). The anti-angiogenic DEB-TGI model developed in Chapter 4, is, thus, adopted to describe the single agent arms treated with an anti-angiogenic drug.

Finally, the Tumor-in-host DEB-TGI model characterized by the Sys. 2.32 -2.34 is used to describe tumor and host body dynamics in the single agent chemotherapy arms (panel C in Fig. 5.1). As already discussed in Chapter 2, tumor cells hit by the drug enter in the transit compartments leading to cell death; moreover, an inhibited assimilation due to the toxic drug-effect characterizes the treatment period.

The no-interaction Tumor-in-host DEB-TGI combination model

In a combination therapy, when an agent inducing tumor cell kill (either a standard cytotoxic or a targeted therapy) is given together with an anti-angiogenic compound, the simplest modeling assumption is that the two drugs do not interact. Under this hypothesis, the tumor-in-host growth inhibition in the combination arms can be described by a joint model that incorporates both the previously introduced DEB-TGI anti-angiogenic model and DEB-TGI cytotoxic model. The resulted no-interaction model (panel D in Fig. 5.1) is described by the following systems of differential equations in which the suffix 'Cit' refers to the agent inducing tumor cell kill and 'Angio' to the angiogenesis inhibitors.

- Case $\frac{dV}{dt} \geq 0$ (growth of structural biomass)

$$
\begin{cases}
\dfrac{de(t)}{dt} = \dfrac{\nu}{V^{1/3}(t)}\left(\rho(t)\left(\dfrac{V_{1\infty}}{V_{u1}(t)+V(t)}\right)^{2/3} - e(t)\right) \\
\dfrac{dV(t)}{dt} = \dfrac{(1-k_u(t))\nu e(t)V^{2/3}(t) - gmV(t)}{g+(1-k_u(t))e(t)} \\
\dfrac{dV_{u1}(t)}{dt} = \dfrac{(\nu V^{2/3}(t) + mV(t))gk_u(t)e(t)}{gg_u + (1-k_u(t))g_u e(t)} - (m_u - k_2 c_{Cit}(t))V_{u1}(t) \\
\dfrac{dV_{u2}(t)}{dt} = k_2 c_{Cit}(t)V_{u1}(t) - k_1 V_{u2}(t) \\
\dfrac{dV_{u3}(t)}{dt} = k_1 V_{u2}(t) - k_1 V_{u3}(t) \\
\dfrac{dV_{u4}(t)}{dt} = k_1 V_{u3}(t) - k_1 V_{u4}(t) \\
\rho(t) = \rho_b\left(1 - \dfrac{V_{u1}(t)}{IV_{u_{50}} + V_{u1}(t)}\right)\left(1 - \dfrac{c_{Cit}(t)}{IC_{50,Cit} + c_{Cit}(t)}\right) \\
k_u(t) = \dfrac{\mu_u V_{u1}}{V(t) + \mu_u V_{u1}}\left(1 - \dfrac{E_{max}c_{Angio}(t)}{IC_{50,Angio} + c_{Angio}(t)}\right) \\
W(t) = d_V(1 + \xi e(t))V(t) \\
W_u(t) = d_{Vu}(V_{u1}(t) + V_{u2}(t) + V_{u3}(t) + V_{u4}(t))
\end{cases}
\tag{5.1}
$$

with $e(t_0) = e_0$, $V(t_0) = V_0$, $V_{u1}(t_0) = V_{u1_0}$ and $V_{u2}(t_0) = V_{u3}(t_0) = V_{u4}(t_0) = 0$.

- Case $-\delta_{V_{Max}} \leq \dfrac{dV}{dt} < 0$ (degradation of structural biomass)

Only equations relative to $\frac{dV}{dt}$ and $\frac{dV_{u1}}{dt}$ differ from the Sys. 5.1:

$$\begin{cases} \dfrac{dV(t)}{dt} &= \dfrac{(1-k_u(t))\nu e(t)V^{2/3}(t) - gmV(t)}{(1-k_u(t))(e(t)+\omega g)} \\ \dfrac{dV_{u1}(t)}{dt} &= \left(\dfrac{mg\mu_u}{g_u} - m_u\right)V_{u1}(t) - k_2 c_{Cit}(t)V_{u1}(t) \end{cases} \tag{5.2}$$

- Case $\dfrac{dV}{dt} \leq -\delta_{V_{Max}}$ (degradation of structural biomass at the maximum rate)

Only equations relative to $\frac{dV}{dt}$ and $\frac{dV_{u1}}{dt}$ differ from the Sys. 5.1:

$$\begin{cases} \dfrac{dV(t)}{dt} &= -\delta_{V_{Max}} \\ \dfrac{dV_{u1}(t)}{dt} &= \dfrac{k_u(t)}{g_u}\left(e(t)\nu V(t)^{2/3} + \delta_{V_{Max}}(e(t)+\omega g)\right) - m_u V_{u1}(t) + \\ & -k_2 c_{Cit}(t)V_{u1}(t) \end{cases} \tag{5.3}$$

5.2.2 Data analysis

All the steps necessary to analyse a combination experiment, including both the estimation of model parameters against single agent arms and the computation of the expected tumor and host body growth curves for the combination arms, can be carried out in Monolix (version 2016R1) [80] and R (Version 3.4.4).

The population approach and the data analysis of the individual tumor and host body weights is developed in accordance with procedures described in Section 4.3.3. Thus, inter-individual variability is considered only for the initial conditions of structural biomass and volume of inoculated tumor cells, the effect of the anti-angiogenic agent

and the assimilation process. In particular, log-normally distributed random effects are added on the parameters W_0, V_{u0}, $IC_{50,Angio}$ and R_b.

5.2.3 Assessing additivity of the effects

The procedure to assess the additivity of chemotherapy administered in combination with an anti-angiogenesis inhibitor within the Tumor-in-host DEB-based framework, is the following.

- PK of the two drugs are obtained from single agent studies or taken from the literature. Assuming no PK interactions, the PK parameters obtained in the single agent studies can be used to describe the plasma concentrations $c_{Cit}(t)$ and $c_{Angio}(t)$, also, in the combination arms. The hypothesis of no PK interactions, that is sensitive due to the different elimination pathways of the two compounds, can be eventually removed if an appropriate PK study highlights the presence of some PK interaction effects.

- The parameters of the DEB-TGI models (host-related, tumor-related, cachexia-related and single agent drug-related parameters) are estimated from the specific single agent arms included in the combination study or from the available single agent studies. In particular, the typical values and the inter-individual parameters are derived through a non-linear mixed effect approach. Under the assumption of a PD null interaction, model parameters, in particular those relative to the drug activities, preserve in combination the same values of those derived in single agent regimens.

- The plasma profiles $c_{Cit}(t)$ and $c_{Angio}(t)$ are used as inputs in the Tumor-in-host DEB-TGI additive model, together with the

previously derived PD parameters, in order to compute the predicted tumor and host body growth curves in the combination study under the hypothesis of no PD interactions between the two drugs. In particular, thanks to the population approach, both the typical behaviour and the inter-individual variability of the tumor-in-host dynamics are predicted.

- A first visual assessment is obtained by the comparison of the observed and predicted individual tumor and host body weights. In particular, the analysis of tumor profiles allow an immediate evaluation of the anti-tumor effect of the drug combination: experimental tumor weights lying below, above or close to the Predicted Tumor Growth Curves (PTGCs) indicate a synergic, antagonistic or additive interaction, respectively.

- In addition, a statistical evaluation based on the Normalised Prediction Distribution Errors (npde) can be performed. Indeed, metrics for external model evaluation [121, 122, 123] can be used to test the additivity of the anticancer drug effects. More precisely, in absence of PD drug interactions, the DEB-TGI additive model should adequately describe the experimental tumor weights collected in the combination arms (H_0 hypothesis). If H_0 holds, the npde realtive to tumor weights should follow a normal distribution, $\mathcal{N}(0,1)$ [123]: a t-test and a Fisher test for variance can be, respectively, used to verify whether the mean and the variance significantly differ from the expected. The 'npde' package for R can be used to compute and analyse npde [124].

A) Tumor-in-host DEB-based model for control group

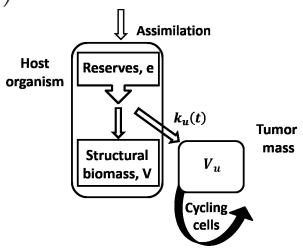

B) Tumor-in-host anti-angiogenic DEB-TGI model

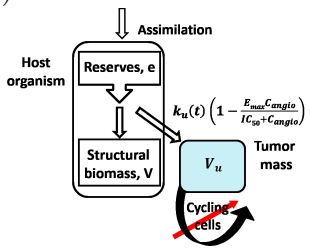

C) Tumor-in-host cell-kill DEB-TGI model

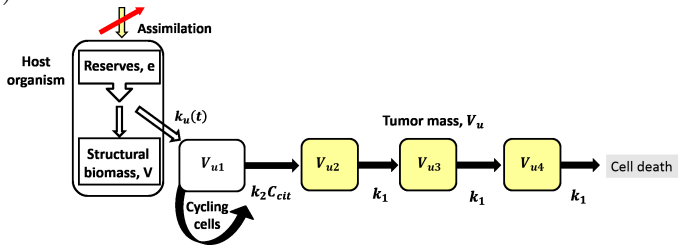

D) Tumor-in-host no-interaction DEB-TGI combination model

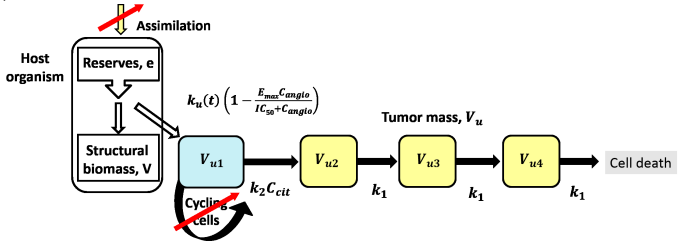

Figure 5.1: Schematic representation of the no-interaction tumor-in-host DEB-TGI model.

5.3 Application to experimental data

In order to illustrate the use of the proposed approach, the analysis of a typical combination experiment is here discussed. The study is one of those routinely performed within several drug development projects in Nerviano Medical Sciences (NMS) labs using human carcinoma cell lines on xenograft mice. Note that, in this context, experimental data are not used to validate the model that acts as reference, providing the expected tumor-in-host growth inhibition assuming no interaction between drugs.

The considered experiment concerns the administration of bevacizumab in combination with two different dosages of NMS-P937 [125], an orally available specific PLK1 inhibitor with antitumor activity in solid and hematological malignancies, synthesized by NMS and, at that time, under preclinical assessment.

5.3.1 The experimental combination study

Forty-two male Balb athymic Nu/Nu mice (5 weeks of age, 26-36g of weight) were obtained from Harlan, S. Pietro al Natisone, Italy, and HT29 cell line from European Collection of Cell Cultures (ECACC). The experimental setting is the same described in Section 1.3.1, in accordance with the best practices and ethic principles.

HT29 tumor-bearing mice were divided in six groups (each of them composed by 7 animals) and treated with bevacizumab, two different dosages of NMS-P937 or combinations of NMS-P937 with bevacizumab. NMS-P937 was given Orally (o.s.) at the dose level of 45 or 60 mg/kg on days 9, 10, 11, 13, 14, 15, 17, 18, and 19. Bevacizumab (20 mg/kg) was given i.p. four times, every 4 days, from day 8. In the combination arms, the two compounds were administered at the same dose levels and schedules of the correspondent single agent arms. A control group, in which mice received vehicle, was also included in the

experiment. All the information about the treated arms are summarized in Tab. 5.1.

Table 5.1: Information about the combination experiment.

Arm	Compounds	Dose	Route	Units	Days of administration
a_1	bevacizumab	20 mg/kg	i.p.	7	in days 8,12,16,20
a_2	NMS-937H	45 mg/kg	o.s.	7	in days 9,10,11,13,14,15,17,18,19
a_3	NMS-937H	60 mg/kg	o.s.	7	in days 9,10,11,13,14,15,17,18,19
a_4	bevacizumab	20 mg/kg	i.p.	7	in days 8,12,16,20
	NMS-937H	45 mg/kg	o.s.	7	in days 9,10,11,13,14,15,17,18,19
a_5	bevacizumab	20 mg/kg	i.p.	7	in days 8,12,16,20
	NMS-937H	60 mg/kg	o.s.	7	in days 9,10,11,13,14,15,17,18,19

In particular, average tumor weight data of controls and treated arms a_1, a_3, and a_5 were already analyzed in [48], whereas the others are unpublished.

5.3.2 PK models

Average pharmacokinetic profiles (plasma concentrations) were generated using mean PK parameters reported in literature. In particular, for bevacizumab the one-compartment open model with first-order absorption already adopted in Chapter 4 were used (see Section 4.3.1 for the parameter values). The NMS-937H plasma profiles were generated using a two-compartment open model with first order absorption and elimination and the mean parameter values reported in [48]: V_1/F=2.13 L/kg, k_{01}= 18.8 1/day, k_{10}=49.2/day, k_{12}=141.1 1/day, k_{21}=10.4 1/day. Simulation of plasma concentration profile for single agent treated arms a_1-a_3 are reported in the Supplementary Material of Chapter 5.

Based on the absence of overlap between the elimination pathways of the two compounds, no relevant PK drug-drug interaction

was expected. Indeed, bevacizumab exposure is not altered significantly when used in combination with many standard therapies [97]. For this reason, parameters values obtained after the single-agent administrations were also used to generate the PK profiles of the two drugs the combination arms.

5.3.3 Identification of the single agent models

The DEB-TGI models were fitted simultaneously against the individual data of tumor and host body weight collected in the controls and the single agent treated groups (arms a_1-a_3). Following the strategy proposed in Section 4.3.3, host-related parameters (g, ν, $V_{1\infty}$, ξ, m, d_V, e_0) were kept fixed to estimates obtained from male mice growth data (same values adopted for Exp. f analyzed in Chapter 4, table in the Supplementary Material of Chapter 4). Conversely, model parameters relative to the tumor (μ_u, g_u, m_u, IV_{u50}), to the cachexia process ($\delta_{V_{max}}$) and to the drugs action ($IC_{50,Angio}$, k_1, k_2, $IC_{50,Cit}$) were estimated from experimental data coming from the single drug administrations. Fitting was performed in Monolix supposing a residual error model proportional to the square root of the predictive values, body or tumor weights ($y = f + b\sqrt{f}\epsilon$).

The estimated parameters (typical values, inter-individual and residual parameters) are reported in Tab. 5.2. In Fig. 5.2, a model simulations (performed with the typical parameter values) are compared to the average data of tumor and host body weight in controls and single agents treated arms. There is good agreement between the data and simulations, leading us to believe that the population DEB-TGI model well captured the dynamics associated with bevacizumab and NMS-937H treatments. Only, tumor re-growth in the 60 mg/kg NMS-937H, arm a_3, is slightly over-estimated. Further model diagnostics (individual fit plots, residual and GOF plots) are reported in the Supplementary Material of Chapter 5. Here, VPC plots are, also, reported

in Fig. 5.3.

Table 5.2: Parameter estimates obtained on controls and single agents arms.

Population parameters		
Parameter [Dimensions]	**Typical values, θ [RSE%]**	**Inter-individual variability, ω [RSE%]**
W_0 $[g]$	33.6 [3]	0.065 [15]
e_0 $[-]$	1.22 [fixed]	-
ρ_b $[-]$	0.867 [NA]	0.278 [NA]
V_{u10} $[cm^3]$	0.04 [22]	0.378 [16]
μ_u $[-]$	5.55 [47]	-
g_u $[-]$	11.55 [48]	-
m_u $[1/day]$	0.026 [43]	-
$IV_{u_{50}}$ $[cm^3]$	4.15 [44]	-
$\delta_{V_{Max}}$ $[cm^3/day]$	0.047 [30]	-
$IC_{50,Angio}$ $[\mu M]$	4.62 [29]	0.341 [90]
k_1 $[1/day]$	0.911 [18]	-
k_2 $[1/\mu Mday]$	0.171 [29]	-
$IC_{50,Cit}$ $[\mu M]$	1.63 [39]	-
Residual variability		
b (W)	0.239 [4]	-
b (W_u)	0.12 [5]	-

Individual parameters are given by $P_i = \theta \exp(\eta_i)$ with θ the typical value and η a random effect normally distributed with zero mean and standard deviation $\omega(P)$. ρ_b and ω (ρ_b) were computed by approximation from estimates of $R_b = 0.154$ (31%) and ω (R_b) =1.02 (15%).

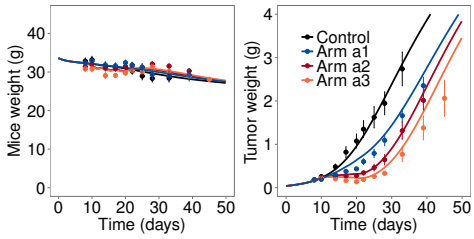

Figure 5.2: Single agent arms: Plots with average observed data (symbols) and model simulations using typical parameters (lines) relative to mice body and tumor weights obtained in controls and single agent arms. Vertical bars *pm* represents standard error.

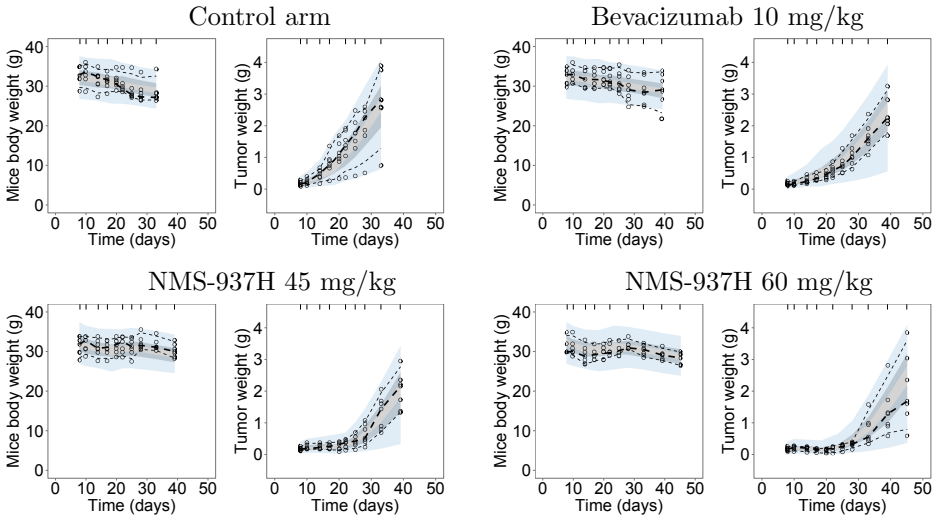

Figure 5.3: Single agent arms: VPC plots stratified by group (1000 replicates of the dataset) relative to placebo and the single agent arms; dashed lines show the 10th, 50th and 90th percentiles of observed data, shaded areas represent the 90% confidence interval for the corresponding model predicted percentile, empty dots are individual observed data.

5.3.4 Assessment of the additivity of the effects

To assess possible interactions between the two drugs, the predicted tumor and host body weight curves of the combination arms a_4 and a_5 were generated by the additive DEB-TGI model (Sys. 5.1-5.3) and the correspondent drug concentration profiles (Fig. 5.4). In particular, in Fig. 5.5 the predicted tumor and host body weight curves assuming additivity of the effects and using the typical values of parameters are over-imposed to the observed average data of the combination arms. Further, Fig. 5.6 shows the external VPC plots obtained simulating 1000 replicates of the dataset.

From the visual assessments, data of the combination arms seem not show significant departures from additivity hypotheses for what concerns both host body cachexia and tumor growth inhibition. Only

treated arm a_5, relative to the combination of bevacizumab with NMS-937H at dose level 60 mg/kg could indicate a slight antagonism in the anticancer effect. However, this phenomena is probably only a consequence of the over-estimated tumor re-growth in the NMS-937H single agent arm a_3.

Focusing the attention on antitumor effect, the absence of significant departures from the expected tumor growth inhibition assuming no drug interactions, was confirmed by the statistical analysis. Npde relative to tumor weights were computed and analyzed in R and the obtained p-values for the two statistical tests are reported in Tab. 5.3 for both the combination arms. Here, the H_0 hypothesis is that the additive model adequately describes the individual tumor weight data in the combination arms (that is, absence of PD drug-drug interaction). Thus, from the obtained p-values there is no evidence to reject the additive hypothesis.

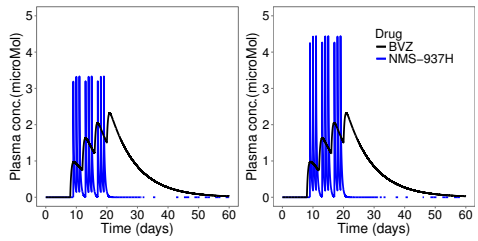

Figure 5.4: Combination arms: Plasma concentration profiles in the treated arm a_4 and a_5.

Table 5.3: p-values for the statistical tests performed on npde.

Arm	**T-test**	**Fisher test**
a_1	0.546	0.681
a_2	0.343	0.958

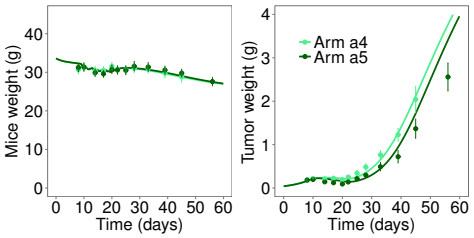

Figure 5.5: Combination arms: Plots with average observed data (symbols) and model prediction using typical parameters (lines) relative to mice body and tumor weights obtained in the combination arms. Vertical bars *pm* represents standard error.

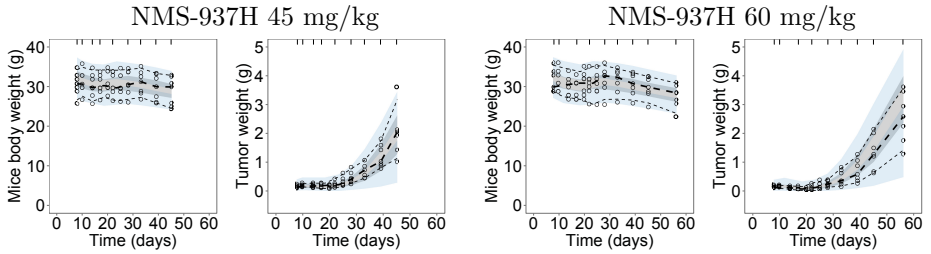

Figure 5.6: VPC plots stratified by group (1000 replicates of the dataset) relative to the combination arms; dashed lines show the 10th, 50th and 90th percentiles of observed data, shaded areas represent the 90% confidence interval for the corresponding model predicted percentile, empty dots are individual observed data.

5.4 Discussion

Given the extensive use of combination therapies in the treatment of cancer, the Tumor-in-host DEB-based approach was extended and adapted to the more complex framework of the combination experiments. Due to their paramount importance in the clinical practise, the focus of this Chapter was placed on anti-angiogenic and chemotherapeutic agents. Thus, starting from the DEB-TGI models previously presented and following the method proposed by Rocchetti et al. [51, 48], a new tumor-in-host modeling approach to evaluate the effects of angiogenesis inhibitors given in combination with cytotoxic

agents was developed.

In particular, a tumor-in-host growth inhibition model able to predict the response of tumor and host organism to a combined treatment of anti-angiogenic and cytotoxic compounds in case of additivity of the effects (no-interaction hypothesis) was developed. The DEB-TGI models introduced in Chapters 2 and 4 for the anticancer activity of cell-killing agents and angiogenesis inhibitors are adopted as references to describe drug effects in monotherapy regimens. Single agent experiments can be used to obtain estimate of the model parameters, even if, controls and single agent arms of the same experiment have to be prefer to assess drug effects. Then, based on these estimates, the no-interaction DEB-TGI model was used to predict the expected tumor and host body growth profiles in the combination experiment assuming no drug-drug interactions. By comparing the predicted curves with actual observed data, the presence of possible interactions and their nature can be easily ascertained by visual inspection. In addition to this qualitative evaluation, a statistical test based on the analysis of npde relative to tumor weight data, was, also, developed.

The proposed modeling approach would like to be an alternative efficacious tool to overcome the complex and discussed problem of the evaluation of drug combinations by exploiting simulations. In order to illustrate its application within the industrial drug discovery process, a real case study has, also, been presented and discussed.

The considered experiment concerns the combination of the anti-VEGF bevacizumab with two different dosages of the PLK1 inhibitor NMS-937H. From the obtained results, no significant differences from the expected effect under the no-interaction hypothesis were found under both efficacy (TGI) and safety (cachexia onset) profiles. However, an incremental tumor growth inhibition due to bevacizumab coadministration was evident from tumor weight profiles, highlighting the advantage of using the combination therapy in comparison with the single-agent therapies.

The combined effects of bevacizumab and NMS-937H were, also, evaluated by Rocchetti et al. in [48]. In that case, the authors found that the combination of bevacizumab and NMS-P937, administered at dose level 60 mg/kg, produced an effect lower than that expected from the Simeoni TGI and Rocchetti TGI models under the no-interaction hypothesis. As a consequence, a model, able to capture this less than additive effect, was developed, including an interaction term: a standard inhibitory function linked the bevacizumab concentration was added on the parameter describing the NMS-P937 potency ($k_{2,inhibited}$).

The conflicting results are worth of further considerations. In both the works, first the concept of additive effect was defined through the development of a theoretical no-interaction model. Then drug combination were classified as synergistic or antagonistic on the basis of departures of observed data from the predictions expected by the no-interaction model. However, the two no-interaction models defining additivity were built using different references for describing the drug activity in the monotherapy regimes. As a consequence, also the classification of drug interactions in the three groups, synergistic, additive or antagonist, may be different. More in details, in [48] the starting points were the Simeoni TGI and Rocchetti TGI models, while, in this Chapter, the additive model was developed on the basis of the more mechanistic framework provided by the DEB theory.

Interestingly, the new approach did not found relevant differences from the expected effect under the additive hypothesis as if its more mechanistic framework, based on the tumor-host energetic interactions, was able, alone, to take into account drug activity in the combination regimens. This trend seems to be confirmed by the analysis of further xenograft experiments (here not presented) in which the effect of bevacizumab combined with other cytotoxic agents was tested. Obviously, this hypothesis has to be further evaluated on a larger number of experimental cases. However, if it will be confirmed, the tumor-in-host DEB-based framework may provide an effective instrument not

only to classify the nature of combination but also to predict the effect of chemotherapy coadministered with anti-angiogenic agents.

Chapter 6

Overall conclusions

Oncology has one of the poorest records for investigational drugs in clinical development with hight attrition rates primarily due to adverse efficacy and safety results in Phase II and III. A likely cause underlying this relevant number of failures is a preclinical drug assessment based on animal models slightly representative of the human condition and the lack of an adequate predictive paradigm of preclinical to clinical translation.

Pharmacometric models could be useful tools to extract, synthesize and integrate information obtained in the often inadequate *in vivo* preclinical experiments, supporting, thus, the transfer of the preclinical results to the clinical setting.

My thesis deals with different M&S applications in the preclinical development of anticancer drugs, highlighting the advantages coming from the development of statistical-mathematical approaches, based on PK/PD models in better characterizing, understanding and predicting PK/PD behaviour of oncology agents.

The actual purpose of this work is a mathematical modeling of interactions between tumor and host organism during anticancer drug

treatments in preclinical studies. To this aim, a tumor-in-host growth model based on a set of tumor-host interaction rules taken from the Dynamic Energy Budget (DEB) theory was developed and applied to analyse different experiments typically performed during the preclinical development of an anticancer drug.

First, a PK/PD model of cachexia onset and tumor growth inhibition (TGI) after anticancer administration was proposed integrating the DEB based tumor-in-growth model with a set of TGI equations derived from the Simeoni TGI model (Chapter 2). This new model is able to describe in a unique framework the different aspects characterizing the *in vivo* tumor growth studies: the drug cytotoxic activity on the tumor, the onset of cachexia due to the treatment, the effect of the tumor on the host and, viceversa, the influence of the host condition on tumor dynamics. Moreover, the tumor-in-host DEB-TGI model is able to quantify the antitumor effect of the treatment and, at the same time, to provide a quantitative measurement of its effect on the host growth. In addition, the contributions to cachexia attributable to the drug (drug-related cachexia) and to the tumor (tumor-related cachexia) are separated by the model. A further advantage of this tumor-in-host modeling approach is the opportunity to disentangle the direct drug effect on the tumor cells from the slowdown in tumor growth due to the depletion of the host energies, avoiding, in this way, an overestimation of the actual antitumor drug efficacy. Biologically relevant considerations were, also, derived from a mathematical analysis of the model: tumor dynamics are characterized by an early exponential growth phase similar to that of the Simeoni TGI model and often observed in experimental setting. Moreover, the minimum constant concentration necessary for the asymptotic tumor eradication was, also, mathematically obtained.

The tumor-in-host DEB-based model, initially developed on average data of xenograft mice, was adapted to analyse individual data of a preclinical study performed for the assessment of etoposide ef-

fects on Wistar rats (Chapetr 3). Due to the use of species-dependent physiological parameters the model resulted applicable also in an experimental contest involving a different target species (rats), while the population approach, based on non-linear mixed effect techniques, allowed to describe for the first time the tumor-host interactions on a individual level. The unusual design of the study, characterized by the presence of tumor-free animals treated or not with etoposide, allowed to completely exploit the model capabilities in describing and discerning all the dynamics concerning tumor-host interactions and, in particular, cachexia onset. The comprehensive experimental design, also, helped to solve identifiability issues previously found [61]. Finally, the PK/PD relationship between plasma of free-intratumoral etoposide concentration and tumor growth kinetics was comparatively investigated. In particular, only the use of the free-interstitial tumor concentration, accounting for the non-linear drug perfusion in the tumor tissue, enabled the DEB-TGI model to catch the schedule-dependence of the etoposide inhibitory effect on tumor growth and proved to be a better surrogate for the active concentration exhibiting a cytotoxic effect on tumor cells.

Angiogenesis inhibitors are widely used in the anticancer treatment with the goal of cutting off tumor blood vessels and, so, blocking the proliferation of cancer cells that are deprived of the oxygen and nutrients supply. Thanks to the set of energy balance rules provided by the DEB theory, the tumor-in-host approach, already used to describe the cell-kill activity of cytotoxic agents, was easily adapted to account for the cytostatic effect of angiogenesis inhibitors (Chapter 4). In particular, the tumor growth modulation observed after an anti-angiogenic treatment is adequately modeled as the consequence of an inhibited energy supply to the tumor that follows the reduction of tumor vascularization. Moreover, the mechanistic approach on which the anti-angiogenic DEB-TGI model is based allowed to investigate and formulate realistic hypothesis about the development of

resistance to bevacizumab in DU145 tumor cell line. Starting from literature evidences, a hypoxia-triggered resistance model was developed and integrated in the DEB-TGI anti-angiogenic model, allowing to describe the decreased efficacy of prolonged bevacizumab therapies.

Within the drugs co-administration framework, recognizing possible pharmacodymamic drug-drug interactions represents a fundamental step for the definition and the optimization of new useful combination therapy for the cancer treatment. For this reason, starting from the work of Rocchetti et al [51], a strategy for assessing additivity of anti-angiogenic and chemotherapeutic agents given in *in vivo* combination studies is proposed, also, for the tumor-in-host DEB-based framework. The developed approach is based on the definition of a population no-interaction tumor-in-host DEB-TGI model able to predict the expected tumor and host response to a combination therapy assuming the absence of drug-drug interactions. A case study involving bevacizumab and NMS-937H was analysed, showing how in this case the no-interaction model is able to adequately describe also tumor-in-host dynamics in the combination experiments.

In summary, the proposed models want to provide new valid tools for exploiting data routinely generated in the preclinical phases of anticancer drug development process. The advantages of the developed tumor-in-host approach are manifold. Indeed, with the DEB framework, for the first time, both tumor and host body responses to an anticancer drug treatment can be simultaneously described allowing to take into account relevant dynamics that can potentially affect an unbiased estimate of the anticancer drug efficacy. Between these often undervalued dynamics, a key role is played by the cachexia onset both induced by tumor progression and anticancer drug treatment. In particular, the clinical relevance of the tumor-associated cachexia led to an increasing interest in developing a clear alignment of the animal models with the intended clinical entity in order to facilitate the translation of cachexia research [56, 57]. Furthermore, drug-related

cachexia could be considered an efficacious preclinical endpoints for the toxic effect of the anticancer therapy and its appropriate modeling assessment could help to select the most promising compounds and administration schedules able to show an adequate efficacy and a tolerable toxicity.

The tumor-in-host models, due to the solid mechanistic approach provided by the DEB theory, not only showed excellent capabilities in describing, summarizing and predicting preclinical experimental data but also provided useful instruments to investigate and formulate realistic hypothesis on the complex dynamics characterizing the the tumor-in-host *in vivo* preclinical studies. Finally, even if the model has been originally developed on mouse model, the use of species-dependent physiological parameters allowed the translation from one species to another. Interestingly, the DEB-based model predicts an exponential tumor growth that has been observed also in several types of human malignancies. These findings, although preliminary, encourage to deeper investigate the applicability of the model as an efficient translational tool from animal to human studies of anticancer drug activity.

The results presented in the previous chapters showed that the tumor-in-host modeling approach, due to the mechanistic basis taken from the DEB theory, provides a framework flexible and general enough to be applicable to different preclinical settings.

Appendix A

Supplementary Material to Chapter 2

A.1 Proofs of propositions

Proposition 1:
By zeroing the state derivatives in the Sys. 2.11, it follows that the equilibrium states $\bar{e}$ and $\bar{V}$ have to satisfy the relationships

$$0 = \nu\left(\frac{\varrho V_{1\infty}^{2/3}}{\bar{V}} - \frac{\bar{e}}{\bar{V}^{1/3}}\right) \text{ with } \bar{V} > 0 \tag{A.1}$$

$$0 = \frac{\nu\bar{e}\bar{V}^{2/3} - gm\bar{V}}{g + \bar{e}}\,. \tag{A.2}$$

Eq. A.1 implies that

$$\bar{e} = \rho(V_{1\infty}/\bar{V})^{2/3} \tag{A.3}$$

and replacing Eq. A.3 and Eq. 2.7 (for m) in Eq. A.2, it follows that

$$\bar{V} = \frac{\nu\rho V_{1\infty}^{2/3}}{gm} = \rho V_{1\infty}\,. \tag{A.4}$$

Finally, from Eqs. A.4 and A.3, we obtain $\bar{e} = \rho^{1/3}$.

Proposition 2:
To study its asymptomatically stability, we have linearized the Sys. 2.11 in a neighborhood of the equilibrium point $P = (\bar{e}, \bar{V}) = (\rho^{1/3}, \rho V_{1\infty})$, computing the Jacobian matrix and evaluating it in P:

$$J_1 = \begin{bmatrix} \dfrac{-\nu}{\rho^{1/3}V_{1\infty}^{1/3}} & \dfrac{-2\nu}{3\rho V_{1\infty}^{4/3}} \\ \dfrac{\nu\rho^{2/3}V_{1\infty}^{2/3}}{g+\rho^{1/3}} & \dfrac{-\nu}{3V_{1\infty}^{1/3}(g+\rho^{1/3})} \end{bmatrix}.$$

Note that, for biologically relevant values of parameters ($\rho > 0$, $\nu > 0$, $g > 0$ and $V_{1\infty} > 0$), the trace of J_1 is always negative while its determinant always positive. Thus, the eigenvalues of J_1 are both negative and the equilibrium point P is asymptotically stable.

Proposition 3:
By zeroing the state derivative in the Sys. 2.23, it follows that the equilibrium points $(\bar{e}, \bar{V}, \bar{V}_u)$ have to satisfy the relationships:

$$0 = \frac{\nu}{\bar{V}^{1/3}}\left(\rho\left(\frac{V_{1\infty}}{\bar{V}+\bar{V}_u}\right)^{2/3} - \bar{e}\right) \tag{A.5}$$

$$0 = F_V(\bar{e}, \bar{V}, \bar{V}_u) \tag{A.6}$$

$$0 = F_{V_u}(\bar{e}, \bar{V}, \bar{V}_u)\,. \tag{A.7}$$

Eq. A.5 implies

$$\bar{e} = \rho\left(\frac{V_{1\infty}}{\bar{V}+\bar{V}_u}\right)^{2/3}. \tag{A.8}$$

Depending on $\bar{V}$ and $\bar{V}_u$, three cases are possible (Cases A, B and C).

Case A: From the Sys. 2.24, Eq. A.6 implies

$$\nu\bar{e}\bar{V}^{2/3} - gm\big(\mu_u\bar{V}_u + \bar{V}\big) = 0\,. \tag{A.9}$$

Replacing the expression of $\bar{e}$ (Eq. A.8), Eq. A.9 becomes

$$\bar{V} + \mu_u\bar{V}_u = \rho V_{1\infty}\left(\frac{\bar{V}}{\bar{V}_u + \bar{V}}\right)^{2/3}, \tag{A.10}$$

that in particular meets the equality in the conditions of Case A (Eq. 2.26).
From the Sys. 2.25, Eq. A.7 implies

$$\left[\frac{\big(\nu\bar{V}^{2/3} + m\bar{V}\big)g\bar{e}\mu_u}{gg_u\big(\mu_u\bar{V}_u + \bar{V}\big) + g_u\bar{e}\bar{V}} - m_u\right]\bar{V}_u = 0\,. \tag{A.11}$$

Now two cases are possible.
If $\bar{V}_u = 0$, Eq. A.11 is automatically satisfied and from Eqs. A.8 and A.10 it follows that $\bar{V} = \rho V_{1\infty}$ and $\bar{e} = \rho^{1/3}$.
If $\bar{V}_u \neq 0$, recalling the expression of $\bar{e}$ (Eq. A.8), the Eq. A.10 implies that $\mu_u\bar{V}_u + \bar{V} = \bar{V}^{2/3}V_{1\infty}^{1/3}\bar{e}$. Thus, replacing it in Eq. A.11 and recalling the expression of m (Eq. 2.7), the Eq. A.11 becomes

$$\frac{mg\mu_u}{g_u} - m_u = 0\,, \tag{A.12}$$

that is satisfied if and only if $\tilde{\lambda}_0 = 0$.

Case B: From the Sys. 2.24, again Eq. A.6 implies $\nu\bar{e}\bar{V}^{2/3} - gm(\mu_u\bar{V}_u + \bar{V}) = 0$ and replacing the expression of $\bar{e}$ (Eq. A.8), we refind Eq. A.10. Nevertheless, it does not satisfy the conditions of Case B (Eq. 2.27), thus there is not admissible solutions.

Case C: From the Sys. 2.24, Eq. A.6 becomes $-\delta_{V_{Max}} = 0$, that is never eligible from a biologically point of view.

In summary, if $\tilde{\lambda}_0 \neq 0$, the system admits a unique equilibrium point $(\bar{e}, \bar{V}, \bar{V}_u) = (\rho^{1/3}, \rho V_{1\infty}, 0)$; if $\tilde{\lambda}_0 = 0$ there are infinite equilibrium points that have to satisfy Eqs. A.8 and A.10.

Proposition 4:
Because in P_1 the conditions of Case A are satisfied, the system is characterized by the equations:

$$\begin{cases} \dfrac{de(t)}{dt} = \dfrac{\nu}{V^{1/3}(t)}\left(\rho\left(\dfrac{V_{1\infty}}{V_u(t)+V(t)}\right)^{2/3} - e(t)\right) \\ \dfrac{dV(t)}{dt} = \dfrac{V\left[\nu e(t)V(t)^{2/3} - gm(\mu_u V_u(t) + V(t))\right]}{g(\mu_u V_u(t) + V(t)) + e(t)V(t)} \\ \dfrac{dV_u(t)}{dt} = \left[\dfrac{\left(\nu V(t)^{2/3} + mV(t)\right)ge(t)\mu_u}{gg_u(\mu_u V_u(t) + V(t)) + g_u e(t)V(t)} - m_u\right]V_u(t) \end{cases} \tag{A.13}$$

Thus, to study its asymptomatically stability, we have linearized the Sys. A.13 in a neighborhood of the equilibrium point P_1, computing the Jacobian matrix and evaluating it in P_1:

$$J_2 = \begin{bmatrix} \dfrac{-\nu}{\rho^{1/3}V_{1\infty}^{1/3}} & \dfrac{-2\nu}{3\rho V_{1\infty}^{4/3}} & \dfrac{-2\nu}{3\rho V_{1\infty}^{4/3}} \\ \dfrac{\nu\rho^{2/3}V_{1\infty}^{2/3}}{g+\rho^{1/3}} & \dfrac{-\nu}{3V_{1\infty}^{1/3}(g+\rho^{1/3})} & \dfrac{-\mu_u\nu}{V_{1\infty}^{1/3}(g+\rho^{1/3})} \\ 0 & 0 & \dfrac{\nu\mu_u}{V_{1\infty}^{1/3}g_u} - m_u \end{bmatrix}.$$

Because the 2x2 principal sub-matrix of J_2 coincides with the matrix J_1 which eigenvalues are always negative (for biologically relevant values of parameters), the stability of P_1 is determined only by the value of $(\nu\mu_u)/(V_{1\infty}^{1/3}g_u) - m_u$ that, recalling Eq. 2.7, we can re-write as $\tilde{\lambda}_0$. Thus, P_1 is locally asymptotically stable if $\tilde{\lambda}_0 < 0$, unstable if $\tilde{\lambda}_0 > 0$.

Proposition 5:
By zeroing the state derivative in Sys. 2.35, it follows that the equilibrium points $(\bar{e}, \bar{V}, \bar{V}_{u1}, \bar{V}_{u2}, \bar{V}_{u3}, \bar{V}_{u4})$ have to satisfy the relationships:

$$\begin{aligned} 0 &= \frac{\nu}{\bar{V}^{1/3}}\left(\rho(\bar{c})\left(\frac{V_{1\infty}}{\bar{V}+\bar{V}_{u1}}\right)^{2/3} - \bar{e}\right) && \text{(A.14)} \\ 0 &= F_V(\bar{e}, \bar{V}, \bar{V}_{u1}) && \text{(A.15)} \\ 0 &= F_{V_u}(\bar{e}, \bar{V}, \bar{V}_{u1}) - k_2\bar{c}\bar{V}_{u1}\,. && \text{(A.16)} \\ 0 &= k_2\bar{c}\bar{V}_{u1} - k_1\bar{V}_{u2}\,. && \text{(A.17)} \\ 0 &= k_1(\bar{V}_{u2} - \bar{V}_{u3})\,. && \text{(A.18)} \\ 0 &= k_1(\bar{V}_{u3} - \bar{V}_{u4})\,. && \text{(A.19)} \end{aligned}$$

Eq. A.14 implies

$$\bar{e} = \rho(\bar{c})\left(\frac{V_{1\infty}}{\bar{V}+\bar{V}_{u1}}\right)^{2/3}. \qquad \text{(A.20)}$$

Eqs. A.17-A.19 imply

$$\bar{V}_{u2} = \bar{V}_{u3} = \bar{V}_{u4} = \frac{k_2\bar{c}}{k_1}\bar{V}_{u1}\,. \qquad \text{(A.21)}$$

Depending on $\bar{V}$ and $\bar{V}_u$, three cases are possible (Cases A, B and C).

Case A: From the Sys. 2.24, Eq. A.15 implies

$$\nu\bar{e}\bar{V}^{2/3} - gm\big(\mu_u\bar{V}_{u1} + \bar{V}\big) = 0\,. \qquad \text{(A.22)}$$

Replacing the expression of $\bar{e}$ (Eq. A.20), Eq. A.22 becomes

$$\bar{V} + \mu_u\bar{V}_{u1} = \rho(\bar{c})V_{1\infty}\left(\frac{\bar{V}}{\bar{V}_{u1}+\bar{V}}\right)^{2/3}, \qquad \text{(A.23)}$$

that in particular meets the equality in the conditions of Case A (Eq. 2.26).

From the Sys. 2.25, Eq. A.16 implies

$$\left[\frac{\left(\nu\bar{V}^{2/3}+m\bar{V}\right)g\bar{e}\mu_u}{gg_u\left(\mu_u\bar{V}_{u1}+\bar{V}\right)+g_u\bar{e}\bar{V}}-m_u\right]\bar{V}_{u1}=0\,. \tag{A.24}$$

Now two cases are possible.
If $\bar{V}_{u1}=0$, Eq. A.24 is automatically satisfied and from Eqs. A.20,A.21 and A.23 it follows that $\bar{e}=\rho^{1/3}$, $\bar{V}=\rho V_{1\infty}$ and $\bar{V}_{u2}=\bar{V}_{u3}=\bar{V}_{u4}=0$. If $\bar{V}_{u1}\neq 0$, recalling the expression of $\bar{e}$ (Eq. A.20), the Eq. A.23 implies that $\mu_u\bar{V}_{u1}+\bar{V}=\bar{V}^{2/3}V_{1\infty}^{1/3}\bar{e}$. Thus, replacing it in Eq. A.24 and recalling the expression of m (Eq. 2.7), it follows

$$\frac{mg\mu_u}{g_u}-m_u-k_2\bar{c}=\tilde{\lambda}_0-k_2\bar{c}=0\,, \tag{A.25}$$

that, because $\tilde{\lambda_0}>0$, is satisfied if and only if $\bar{c}=\tilde{\lambda}_0/k_2$.

Case B: From the Sys. 2.24, again Eq. A.15 implies $\nu\bar{e}\bar{V}^{2/3}-gm(\mu_u\bar{V}_{u1}+\bar{V})=0$ and replacing the expression of $\bar{e}$ (Eq. A.20), we refind Eq. A.23. Nevertheless, it does not satisfy the conditions of Case B (Eq. 2.27), thus there is not admissible solutions.

Case C: From the Sys. 2.24, Eq. A.15 becomes $-\delta_{V_{Max}}=0$, that is never eligible from a biologically point of view.

In summary, if $\bar{c}\neq\tilde{\lambda}_0/k_2$, the system admits a unique equilibrium point $(\bar{e},\bar{V},\bar{V}_{u1},\bar{V}_{u2},\bar{V}_{u3},\bar{V}_{u4})=(\rho(\bar{c})^{1/3},\rho(\bar{c})V_{1\infty},0,0,0,0)$; if $\bar{c}=\tilde{\lambda}_0/k_2$ there are infinite equilibrium points that have to satisfy Eqs. A.20, A.21 and A.23.

Proposition 6:
Because in $P_{c,1}$ the conditions of Case A are satisfied, the system is characterized by the equations:

$$\begin{cases} \dfrac{de(t)}{dt} = \dfrac{\nu}{V^{1/3}(t)}\left(\rho(\bar{c})\left(\dfrac{V_{1\infty}}{V_{u1}(t)+V(t)}\right)^{2/3} - e(t)\right) \\ \dfrac{dV(t)}{dt} = \dfrac{V\left[\nu e(t)V(t)^{2/3} - gm(\mu_u V_{u1}(t)+V(t))\right]}{g(\mu_u V_{u1}(t)+V(t)) + e(t)V(t)} \\ \dfrac{dV_{u1}(t)}{dt} = \left[\dfrac{\left(\nu V(t)^{2/3} + mV(t)\right)ge(t)\mu_u}{gg_u(\mu_u V_{u1}(t)+V(t)) + g_u e(t)V(t)} - m_u - k_2\bar{c}\right]V_{u1}(t) \\ \dfrac{dV_{u2}(t)}{dt} = k_2\bar{c}V_{u1}(t) - k_1 V_{u2}(t) \\ \dfrac{dV_{u3}(t)}{dt} = k_1 V_{u2}(t) - k_1 V_{u3}(t) \\ \dfrac{dV_{u4}(t)}{dt} = k_1 V_{u3}(t) - k_1 V_{u4}(t) \end{cases} \tag{A.26}$$

Thus, to study its asymptomatically stability, we have linearized the Sys. A.26 in a neighborhood of the equilibrium point $P_{c,1}$. The Jacobian matrix evaluated in $P_{c,1}$ is given by

$$J_3 = \begin{bmatrix} \dfrac{-\nu}{\rho(\bar{c})^{1/3}V_{1\infty}^{1/3}} & \dfrac{-2\nu}{3\rho(\bar{c})V_{1\infty}^{4/3}} & \dfrac{-2\nu}{3\rho(\bar{c})V_{1\infty}^{4/3}} & 0 & 0 & 0 \\ \dfrac{\nu\rho(\bar{c})^{2/3}V_{1\infty}^{2/3}}{g+\rho(\bar{c})^{1/3}} & \dfrac{-\nu}{3V_{1\infty}^{1/3}(g+\rho(\bar{c})^{1/3})} & \dfrac{-\mu_u\nu}{V_{1\infty}^{1/3}(g+\rho(\bar{c})^{1/3})} & 0 & 0 & 0 \\ 0 & 0 & \tilde{\lambda}_0 - k_2\bar{c} & 0 & 0 & 0 \\ 0 & 0 & k_2\bar{c} & -k_1 & 0 & 0 \\ 0 & 0 & 0 & 0 & -k_1 & 0 \\ 0 & 0 & 0 & 0 & 0 & -k_1 \end{bmatrix}.$$

Because the 2x2 principal sub-matrix of J_3 coincides with the matrix J_1 which eigenvalues are always negative (for biologically relevant values of parameters) and $k_1 > 0$, the stability of $P_{c,1}$ is determined

only by the sign of $\tilde{\lambda}_0 - k_2\bar{c}$. Thus, because $\tilde{\lambda_0} > 0$, $P_{c,1}$ is locally asymptotically stable if $\bar{c} < \tilde{\lambda}_0/k_2$, unstable if $\bar{c} > \tilde{\lambda}_0/k_2$.

Appendix B

Supplementary Material to Chapter 3

B.1 PK models of etoposide in Wistar rats

PK model of etoposide in W256 tumor-bearing Wistar rats

The four-compartment model reported in [76] was used to simulate the etoposide concentration-time profiles in plasma (C_{Plasma}) and in two tumor regions ($C_{T,Periphery}$ and $C_{T,Center}$) in the tumor-bearing animals. The model structure is reported in Fig. **??**. The system of equations describing the model is

$$
\begin{cases}
\dfrac{dA_1(t)}{dt} & = A_2k_{21} + A_3k_{31} + A_4k_{41} - A_1(k_{10} + k_{12}) + \\
 & \quad -\left(\dfrac{V_{max}A_1}{V_1k_m + A_1}\right) - \left(\dfrac{V_{max}A_1}{V_1k_m + A_1}\right) \\
\dfrac{dA_2(t)}{dt} & = A_1k_{12} - A_2k_{21} \\
\dfrac{dA_3(t)}{dt} & = \left(\dfrac{V_{max}A_1}{V_1k_m + A_1}\right) - A_3k_{31} \\
\dfrac{dA_4(t)}{dt} & = \left(\dfrac{V_{max}A_1}{V_1k_m + A_1}\right) - A_4k_{41} \\
C_{Plasma}(t) & = \dfrac{A_1(t)}{V_1} \\
C_{T,Periphery}(t) & = \dfrac{A_3(t)}{V_3} \\
C_{T,Center}(t) & = \left(\dfrac{A_3(t)}{V_3}F_p\right) + \left(\dfrac{A_4(t)}{V_4}(1 - F_p)\right)
\end{cases}
\tag{B.1}
$$

where A_1, A_2, A_3 and A_4 are the drug amounts in the central (plasma), peripheral (tissues other than the tumor), periphery of the tumor and center of the tumor compartments, respectively; k_{10} is the elimination micro-constant rate from the central compartment and k_{12}, k_{21}, k_{31} and k_{41} are the distribution micro-constant rates between compartments; V_1 represents the volume of the central compartment and V_3 and V_4 are the volume of the tumor periphery and tumor centre compartments, respectively; V_{max} is the maximum distribution rate; k_m is the Michaelis-Menten constant; F_p is the fraction of the centre region with viable cells similar to these of the periphery of the tumor.

A covariate model was included on V_1:

$$V_1 = 0.171\left(\frac{BW}{0.290}\right)^{0.581} \tag{B.2}$$

where 0.171 is the (population) volume of the central compartment estimated by the popPK model; 0.581 is the exponential scaling factor empirically estimated from data; BW is the animal individual body weight (kg); and 0.290 is the mean body weight (kg) of the PK group.

The simulated total plasma and free peripheral tumor drug concentration -time profiles are reported in Fig. **??**. A comparison of plasma and tumour concentration profiles after a single-bolus administration is shown Fig. **??**.

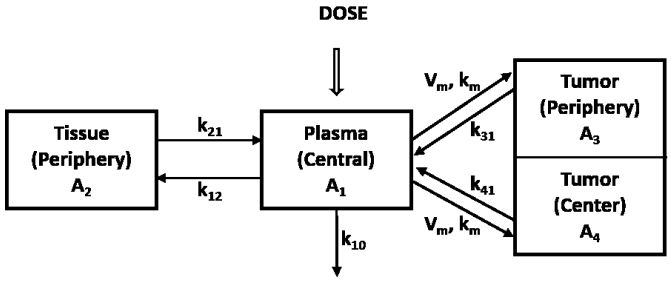

Schematic representation of the etoposide popPK model in W256 tumor-bearing Wistar rats as reportes [76].

PK model of Etoposide in tumor-free Wistar rats

A classical three-compartment model, identified on plasma etoposide concentration data collected in W256 tumor-bearing Wistar rats, was used to simulate etoposide plasma cocentration in tumor-free ani-

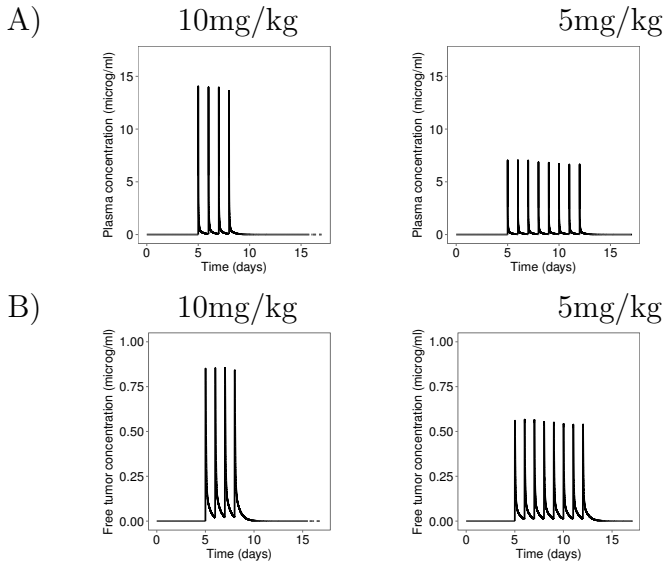

Simulated total plasma (panels A) and free peripheral tumor (panels B) drug concentration profiles in tumor-bearing rats.

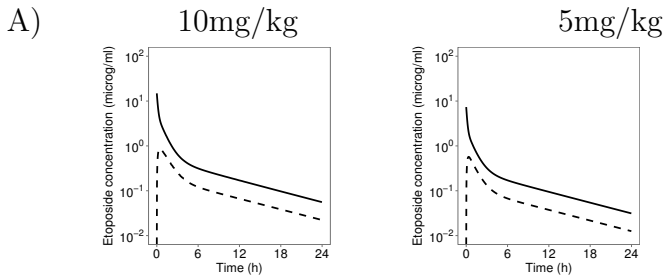

Simulated total plasma (solid line) and free peripheral tumor (dashed line) drug concentration profile after a single-bolus administration in tumor-bearing rats.

mals [1] . The volume of central (plasma) compartment (V) was modeled

[1]No ad-hoc PK studies were performed in healthy animals. However, the main etoposide plasma PK parameters (AUC, CL and t1/2) obtained for W256 tumor-

as a function of the animal body weight (BW) through the following covariate model:

$$V = V_1 \left(\frac{BW}{0.290} \right)^{\beta} \tag{B.3}$$

where V_1 is the (population) volume of the central compartment; β is the exponential scaling factor; BW is the animal individual body weight (kg); and 0.290 is the mean body weight (kg) of the PK group.

The simulated total plasma drug concentration-time profile is reported in Fig. **??**.

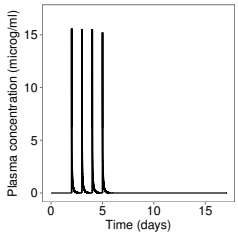

Simulated total plasma concentration-time profiles in the tumor-free rats.

bearing rats [76] were similar to those reported in the literature for healthy animals [78, 79].

Appendix C

Supplementary Material to Chapter 4

C.1 DEB-based model of data relative to tumor-free CD1 athymic Nu/nu mice

The following growth chart relative to CD1 athymic Nu/Nu mice, published by Harlan Laboratories Sprague Dawley, Inc. (HSD), was analyzed to obtain suitable values for the host-related parameters for Exp g. To this aim, the average body weight data of female mice from 3 to 12 weeks old were considered.

Following the identification strategy proposed in [61], the host-related parameters (ν, g, and $V_{1\infty}$) of the tumor-free individual model (Eq. 2.11) were estimated by fitting the tumor-free DEB-based model against average body weight data of female mice. Thus, the fraction of food consumption, ρ, was fixed to 1 according to indications of *ad libitum* food feeding [59]; the parameter m was derived by Eq. 2.7 and the specific weight of structural biomass d_V was fixed to 1 g/cm^3.

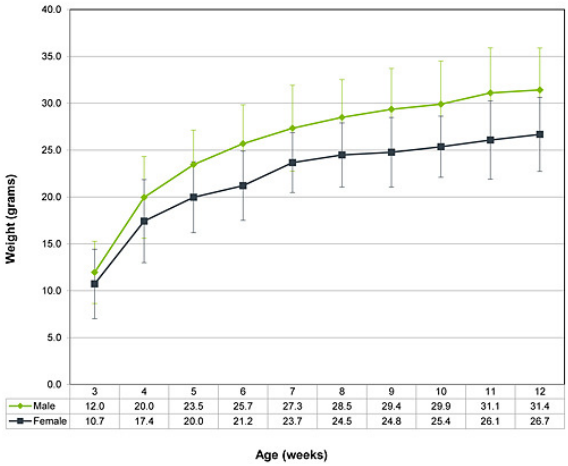

Growth chart of CD1 athymic Nu/Hu mice selected for the identification of the host-related parameters. Mean values (dots) and standard deviations (bars) are shown for male and female mice.

Assuming that the body fat reflects the energy reserves, the parameter ξ was approximated with the product of the fat density and the body fat percentage and fixed to 0.184. Finally, by choosing the mice birth as initial time, the initial value of mice weight (W_0) and of energy reserve (e_0) were fixed to 1 g and 0, respectively, while the initial volume of structural biomass (V_0) was calculated Eq. 2.10. The identification of the Tumor-free DEB-based model Sys.2.11 was performed by supposing a proportional (to predictive values) error model.

The obtained estimates for the model and the residual error parameter (denoted as b) as well as the body weight predictions together with the experimental data are reported in the following.

The value of the energy reserves at the inoculation day (e_0) was, determined by simulating the tumor-free DEB-based model: 1.354 was found for 7 week-old female mice.

Physiological parameter estimates (RSEs between brackets) of the Tumor-free DEB-based model identified on female CD1 mice.

g	ν	$V_{1\infty}$	b
-	$[cm/week]$	$[cm^3]$	-
15.4	7.27	27.1	0.0813
(7%)	(38%)	(17%)	(22%)

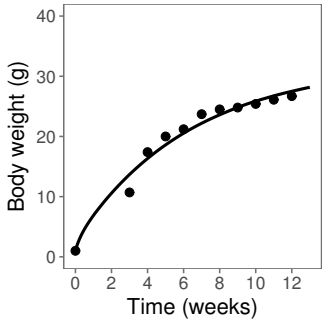

Body weight predictions, obtained by the tumor-free DEB-based model, are shown together with experimental data (mean values) relative to female CD1 mice.

C.2 Tables with parameter values

For each experiments, the tumor-in-host antiangiogenic DEB-TGI model was identified fixed the following host-related parameters.

Host-related parameter values

	g -	ν $[cm/day]$	$V_{1\infty}$ $[cm^3]$	ξ -	m $[1/day]$	e_0 -
Experiment a-h (male Bulb mice 6-week old)	15	1.260	31.2	0.212	0.027	1.345
Experiment b-c-d-e (male Bulb mice 7-week old)	15	1.260	31.2	0.212	0.027	1.267
Experiment f (male Bulb mice 8-week old)	15	1.260	31.2	0.212	0.027	1.22
Experiment g (female CD1 7-week old)	15.4	1.039	27.1	0.184	0.022	1.354

For each experiments, values of ρ_b and $\omega(\rho_b)$ were approximated from the following estimates of R_b and ω (R_b).

Estimates of typical values and sd for parameter R_b .

Parameter [Dimensions]	**Exp a** RSE%	**Exp b** RSE%	**Exp c** RSE%	**Exp d** RSE%	**Exp e** RSE%	**Exp f** RSE%	**Exp g** RSE%	**Exp h** RSE%
R_b	0.003	0.014	0.007	0.003	0.015	0.121	0.048	0.246
-	(> 100%)	(50%)	(73%)	(94%)	(68%)	(48%)	(46%)	(50%)
ω (R_b)	0.793	1.57	2.18	2.25	1.93	0.927	1.23	1.4
-	(51%)	(23%)	(23%)	(26%)	(25%)	(25%)	(26%)	(20%)

C.3 Plasma concentration profiles

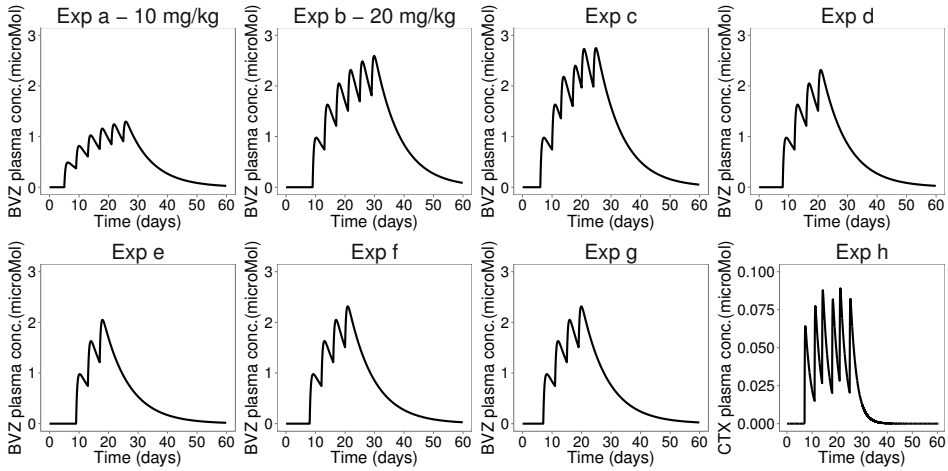

Plasma concentration profiles for Exps. a-h.

C.4 Diagnostic plots

Diagnostic plots for experiment a

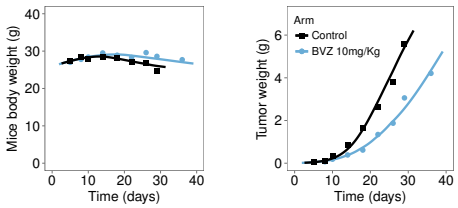

Average data: plots with average observed (symbols) and model-fitted (lines) mice body weight and tumor growth curves obtained in Exp. a for the placebo (light black) and 10 mg/kg bevacizumab (blue) arms.

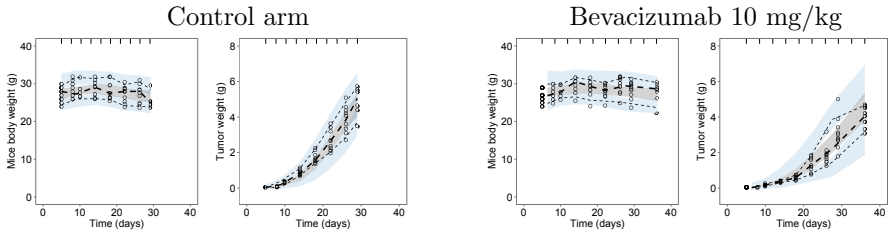

Individual data: VPC plots stratified by group (500 replicates of the dataset) relative to placebo and 10 mg/kg bevacizumab arms; dashed lines show the 10th, 50th and 90th percentiles of observed data, shaded areas represent the 90% confidence interval for the corresponding model predicted percentile, empty dots are individual observed data.

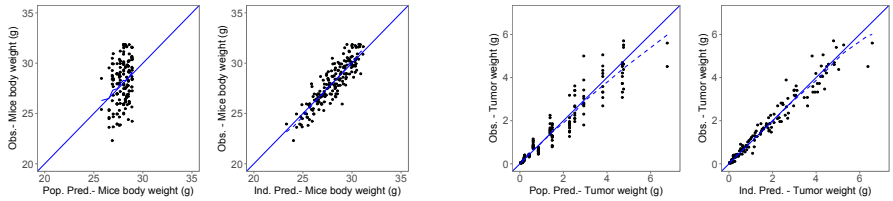

Individual data: GOF plots for mice body (left panels) and tumor weight (right panels) relative to placebo and 10 mg/kg BVZ arms; solid and dashed lines indicate identity line and linear regression fit, respectively.

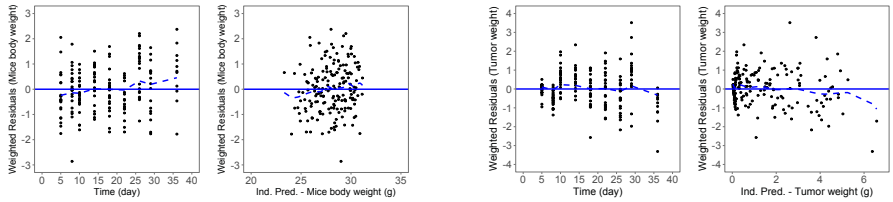

Individual data: residual plots for mice body (left panels) and tumor weight (right panels).

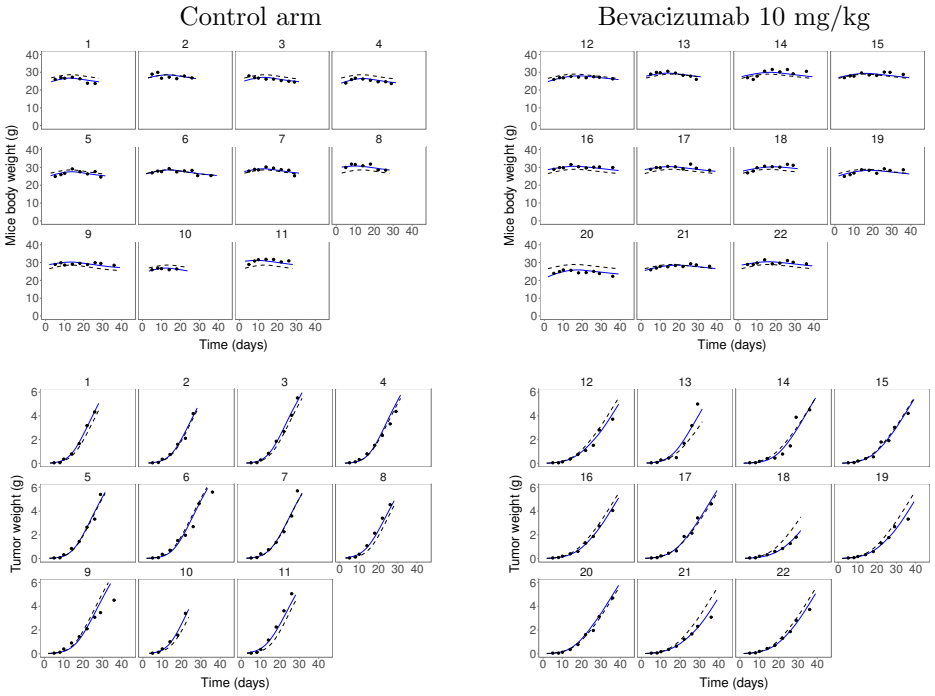

Individual data: individual fit plots for placebo (left panels) and 10 mg/kg bevacizumab treated (right panels) arms of Exp a; black dots represent observed data, solid and dashed lines individual and population model predictions, respectively.

Diagnostic plots for experiment b

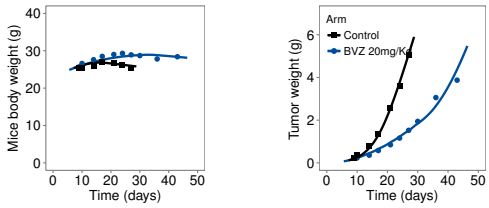

Average data: plots with average observed (symbols) and model-fitted (lines) mice body weight and tumor growth curves obtained in Exp b for the placebo (black) and bevacizumab (blue) arms.

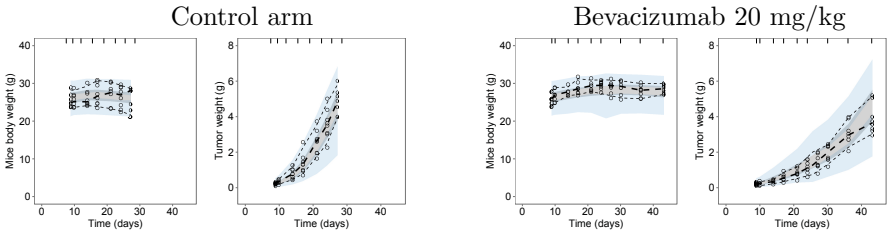

Individual data: VPC plots stratified by group (500 replicates of the dataset); dashed lines show the 10th, 50th and 90th percentiles of observed data, shaded areas represent the 90% confidence interval for the corresponding model predicted percentile, empty dots are individual observed data.

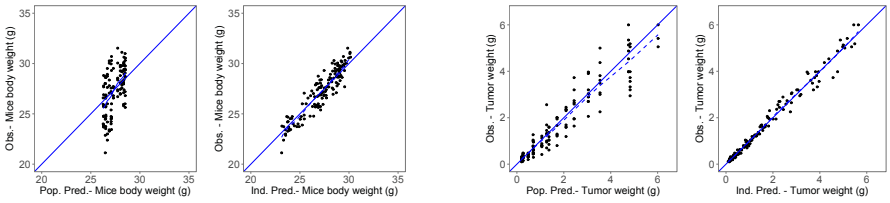

Individual data: goodness-of-fit plots for mice body (left panels) and tumor weight (right panels); solid and dashed lines indicate identity line and linear regression fit, respectively.

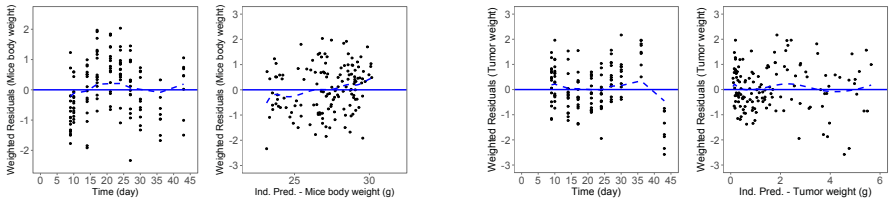

Individual data: residual plots for mice body (left panels) and tumor weight (right panels).

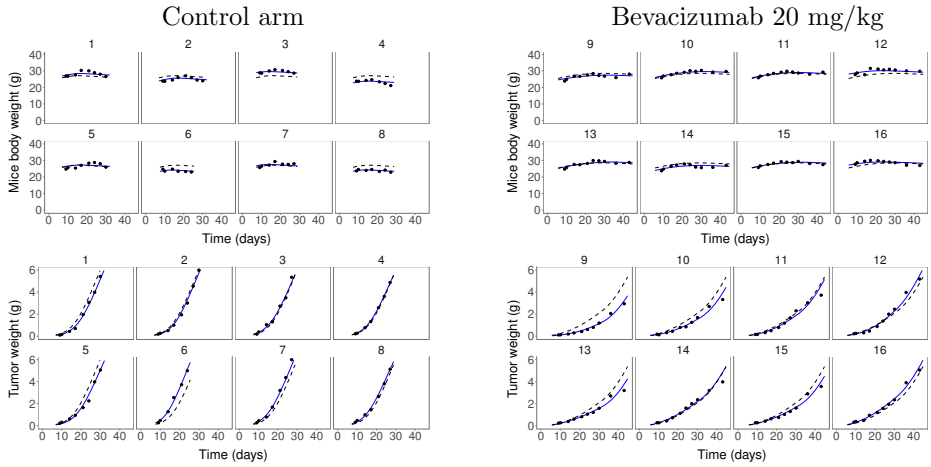

Individual data: individual fit plots for control (left panels) and treated (right panels) arm; black dots represent observed data, solid and dashed lines individual and population model predictions, respectively.

Diagnostic plots for experiment c

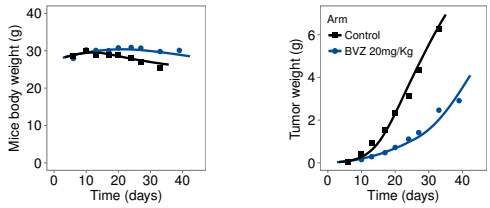

Average data: plots with average observed (symbols) and model-fitted (lines) mice body weight and tumor growth curves obtained in Exp c for the placebo (black) and bevacizumab (blue) arms.

Diagnostic plots for experiment d

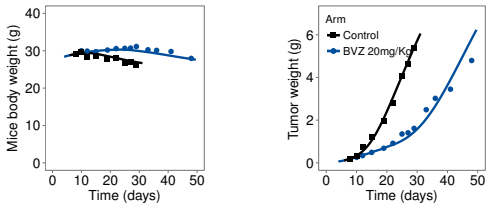

Average data: plots with average observed (symbols) and model-fitted (lines) mice body weight and tumor growth curves obtained in Exp d for the placebo (black) and bevacizumab (blue) arms.

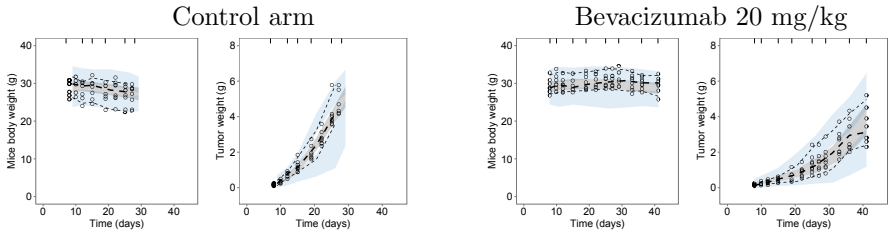

Individual data: VPC plots stratified by group (500 replicates of the dataset); dashed lines show the 10th, 50th and 90th percentiles of observed data, shaded areas represent the 90% confidence interval for the corresponding model predicted percentile, empty dots are individual observed data.

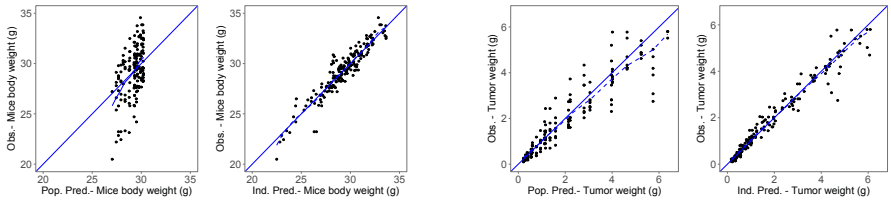

Individual data:goodness-of-fit plots for mice body (left panels) and tumor weight (right panels); solid and dashed lines indicate identity line and linear regression fit, respectively.

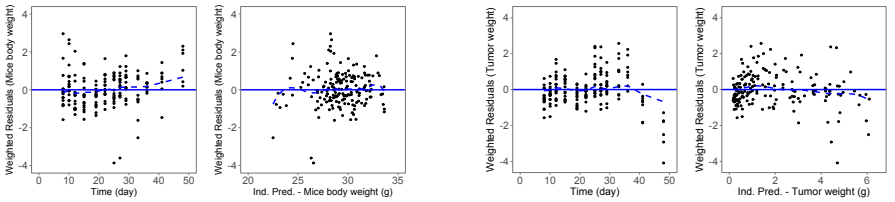

Individual data: residual plots for mice body (left panels) and tumor weight (right panels).

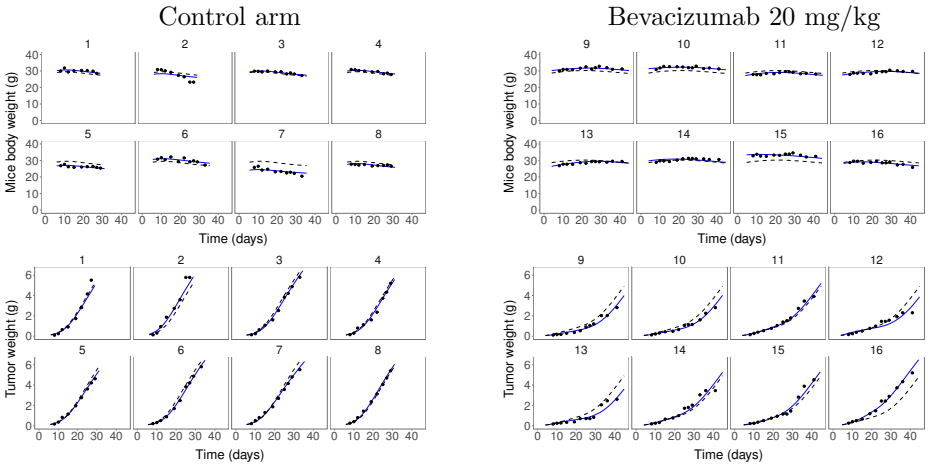

Individual data: individual fit plots for control (left panels) and treated (right panels) arm; black dots represent observed data, solid and dashed lines individual and population model predictions, respectively.

Diagnostic plots for experiment e

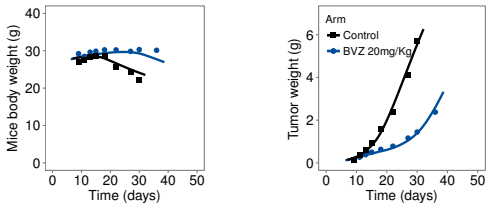

Average data: plots with average observed (symbols) and model-fitted (lines) mice body weight and tumor growth curves obtained in Exp e for the placebo (black) and bevacizumab (blue) arms.

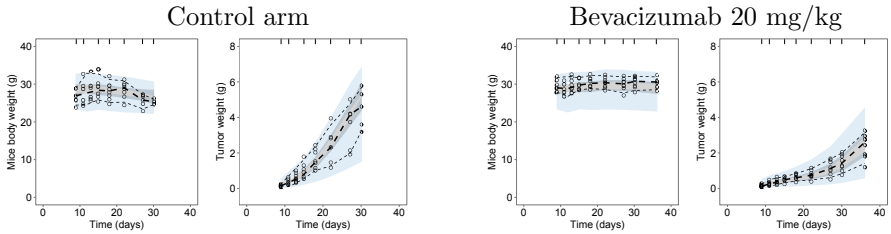

Individual data: VPC plots stratified by group (500 replicates of the dataset); dashed lines show the 10th, 50th and 90th percentiles of observed data, shaded areas represent the 90% confidence interval for the corresponding model predicted percentile, empty dots are individual observed data.

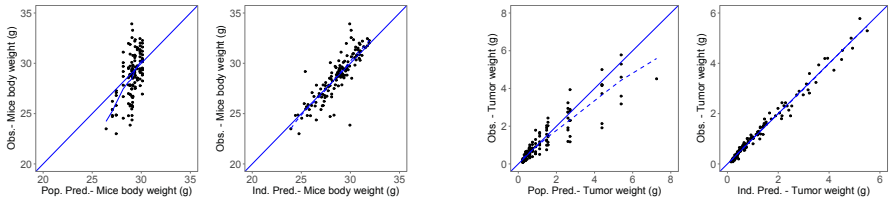

Individual data: goodness-of-fit plots for mice body (left panels) and tumor weight (right panels); solid and dashed lines indicate identity line and linear regression fit, respectively.

C.4. Diagnostic plots

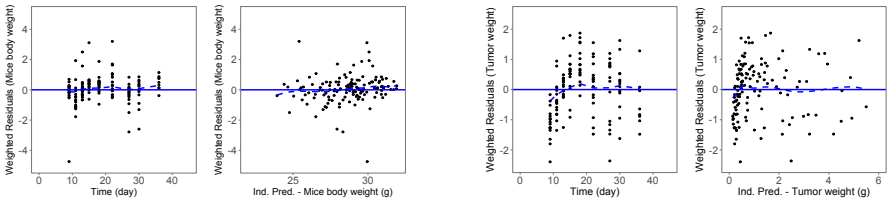

Individual data: residual plots for mice body (left panels) and tumor weight (right panels).

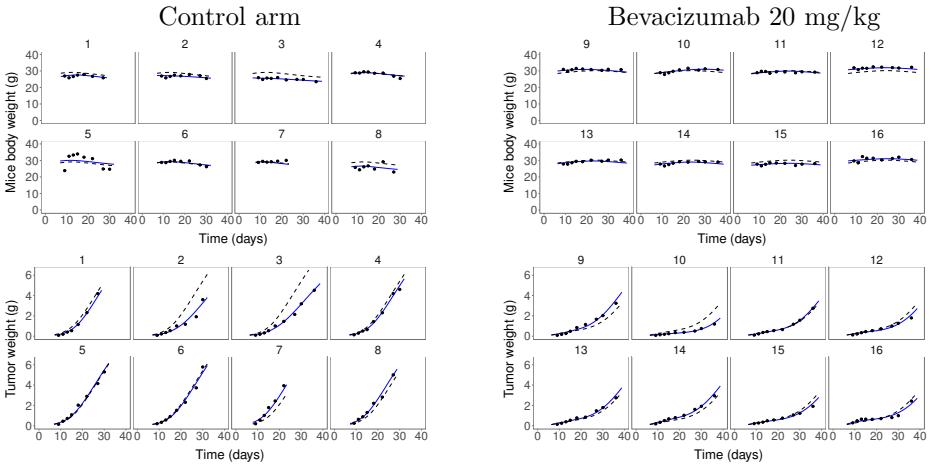

Individual data: individual fit plots for control (left panels) and treated (right panels) arm; black dots represent observed data, solid and dashed lines individual and population model predictions, respectively.

Diagnostic plots for experiment f

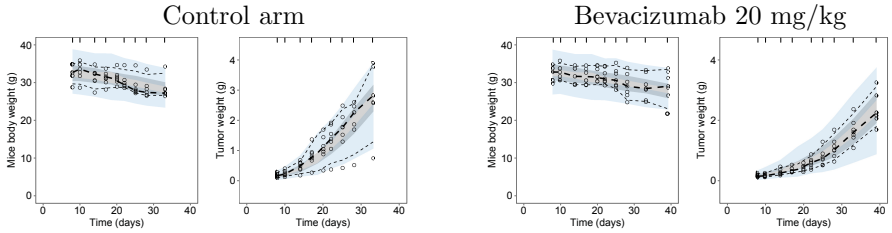

Individual data: VPC plots stratified by group (500 replicates of the dataset); dashed lines show the 10th, 50th and 90th percentiles of observed data, shaded areas represent the 90% confidence interval for the corresponding model predicted percentile, empty dots are individual observed data.

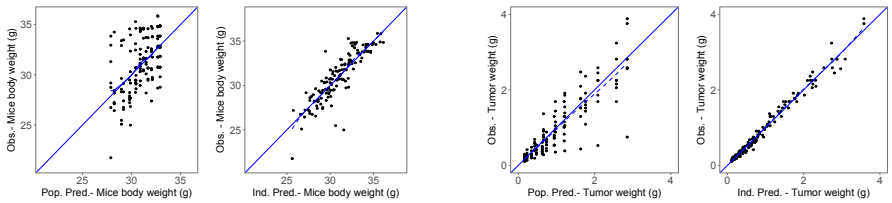

Individual data: goodness-of-fit plots for mice body (left panels) and tumor weight (right panels); solid and dashed lines indicate identity line and linear regression fit, respectively.

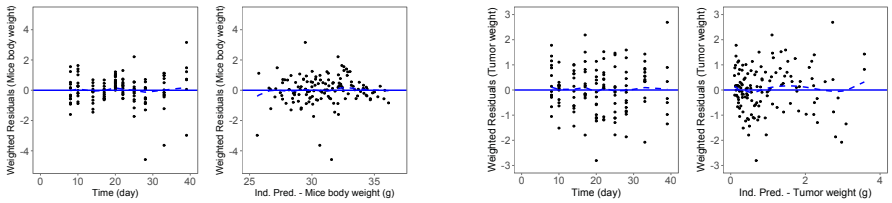

Individual data: residual plots for mice body (left panels) and tumor weight (right panels).

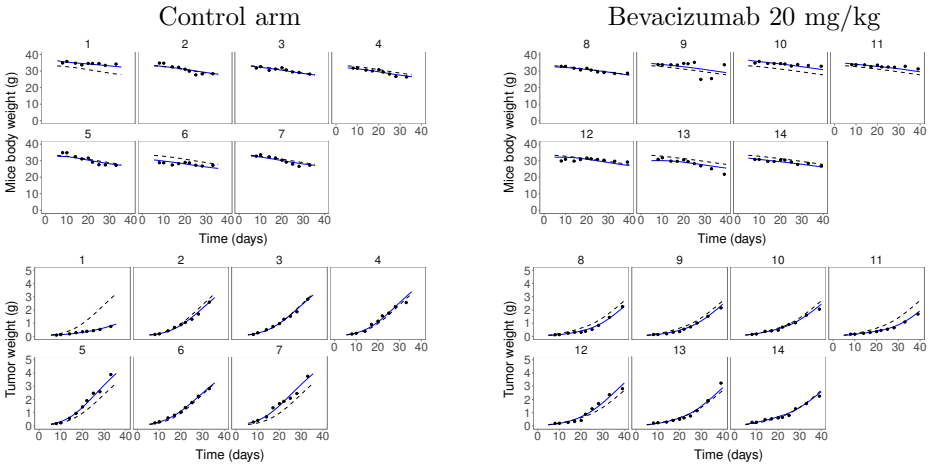

Individual data: individual fit plots for control (left panels) and treated (right panels) arm; black dots represent observed data, solid and dashed lines individual and population model predictions, respectively.

Diagnostic plots for experiment g

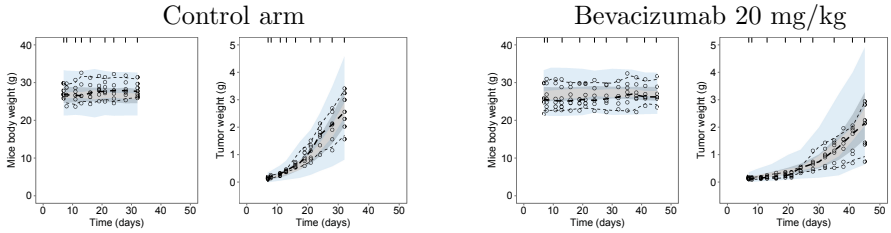

Individual data: VPC plots stratified by group (500 replicates of the dataset); dashed lines show the 10th, 50th and 90th percentiles of observed data, shaded areas represent the 90% confidence interval for the corresponding model predicted percentile, empty dots are individual observed data.

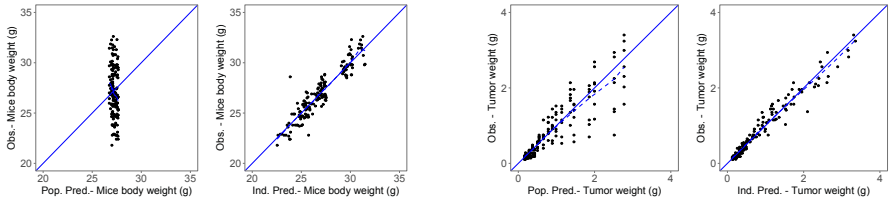

Individual data: goodness-of-fit plots for mice body (left panels) and tumor weight (right panels);solid and dashed lines indicate identity line and linear regression fit, respectively.

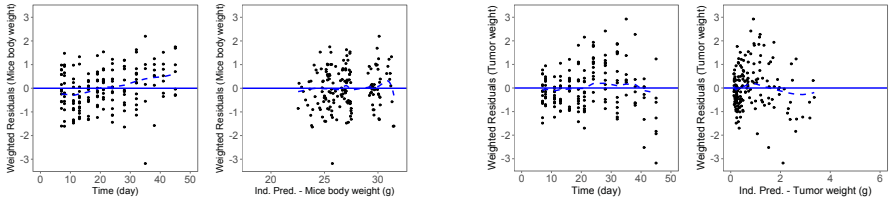

Individual data: residual plots for mice body (left panels) and tumor weight (right panels).

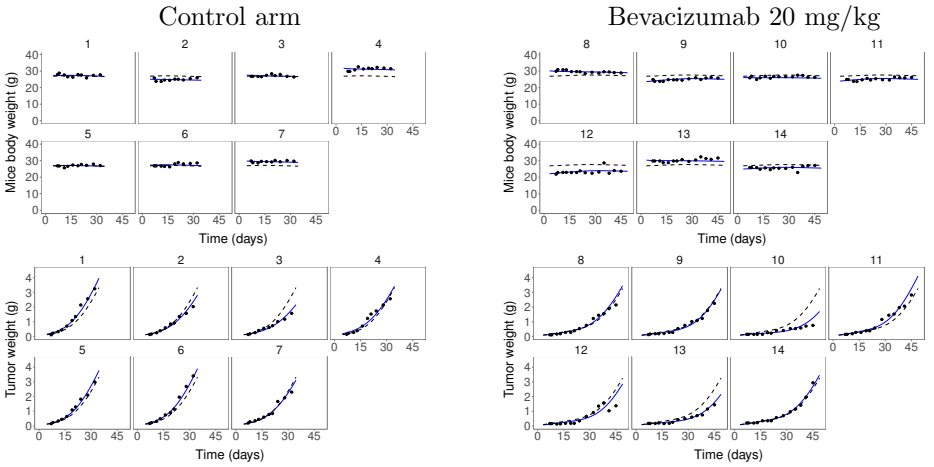

Individual data: individual fit plots for control (left panels) and treated (right panels) arm; black dots represent observed data, solid and dashed lines individual and population model predictions, respectively.

Diagnostic plots for experiment h

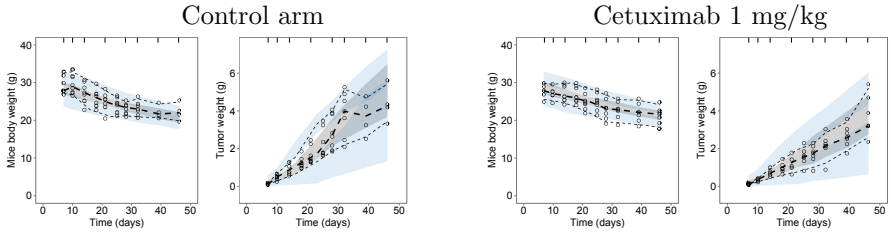

Individual data: VPC plots stratified by group (500 replicates of the dataset); dashed lines show the 10th, 50th and 90th percentiles of observed data, shaded areas represent the 90% confidence interval for the corresponding model predicted percentile, empty dots are individual observed data.

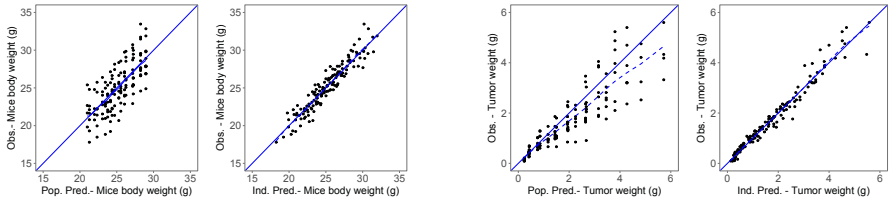

Individual data: goodness-of-fit plots for mice body (left panels) and tumor weight (right panels); solid and dashed lines indicate identity line and linear regression fit, respectively.

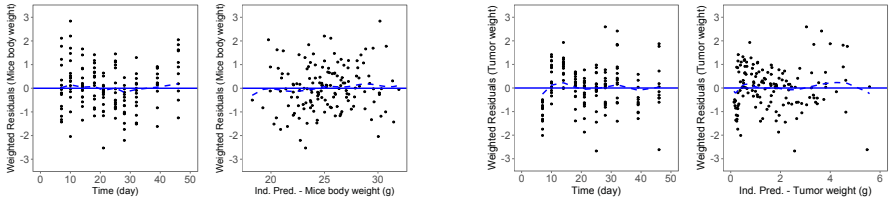

Individual data: residual plots for mice body (left panels) and tumor weight (right panels).

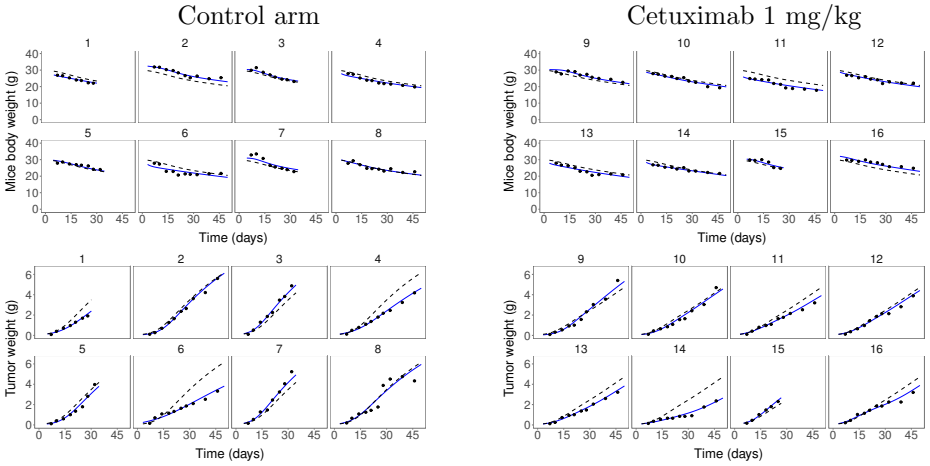

Individual data: individual fit plots for control (left panels) and treated (right panels) arm; black dots represent observed data, solid and dashed lines individual and population model predictions, respectively.

Hypoxia-triggered resistance model: effect of bevacizumab on tumor cell line DU145

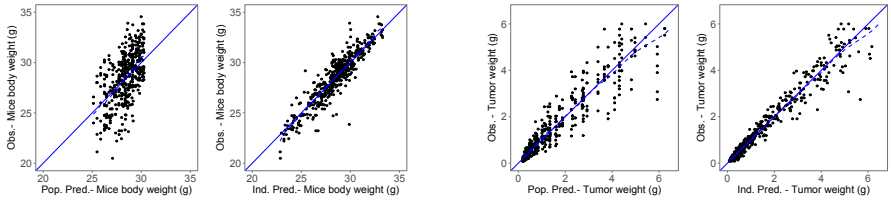

Individual data: goodness-of-fit plots for mice body (left panels) and tumor weight (right panels); solid and dashed lines indicate identity line and linear regression fit, respectively.

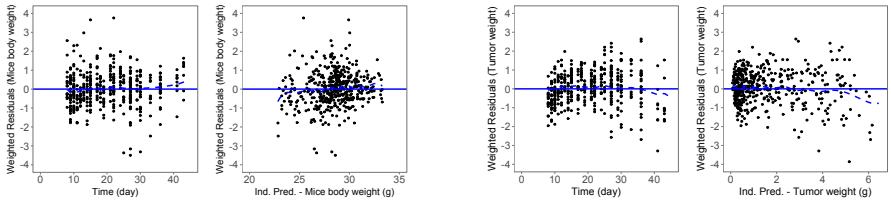

Individual data: residual plots for mice body (left panels) and tumor weight (right panels).

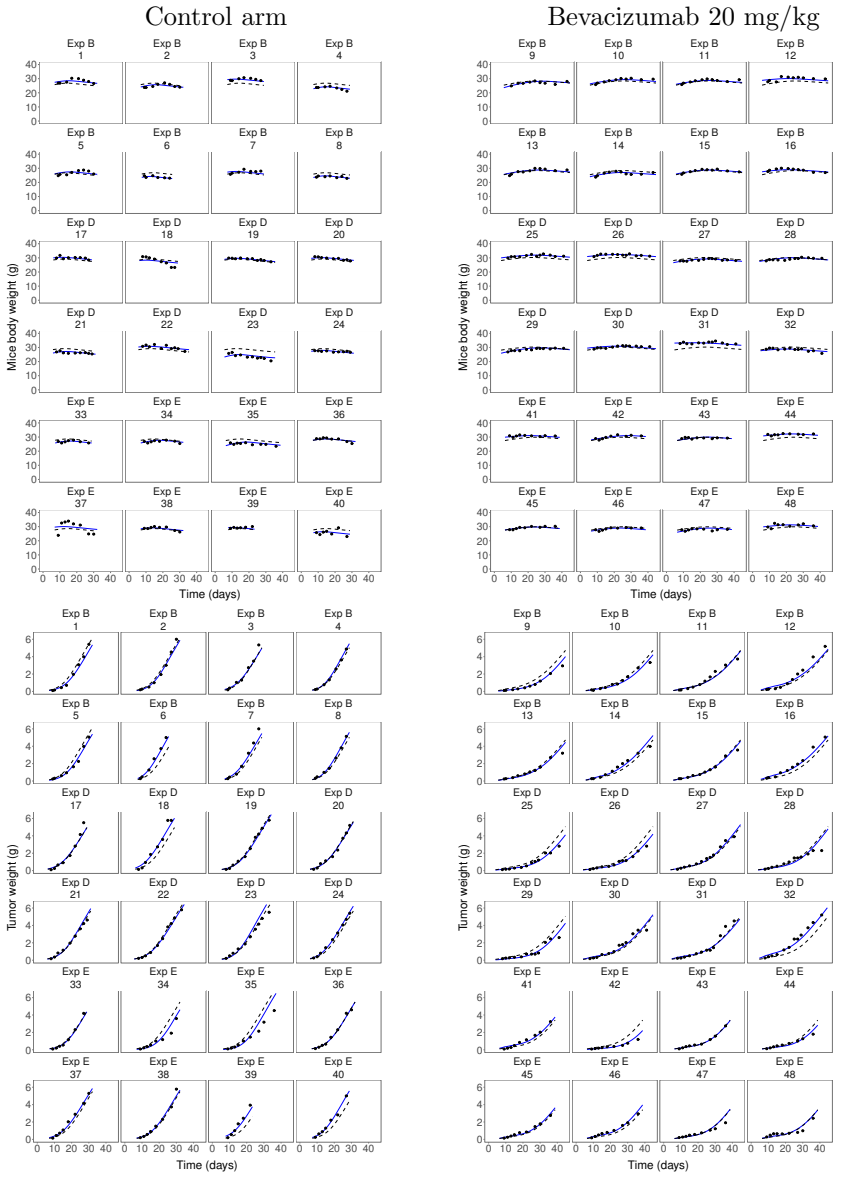

Individual data: individual fit plots for control (left panels) and treated (right panels) arms of Exps b, d and e; black dots are the observed data, solid and dashed lines the individual and population model predictions, respectively.

Hypoxia-triggered resistance model: effect of bevacizumab on tumor cell line CRC

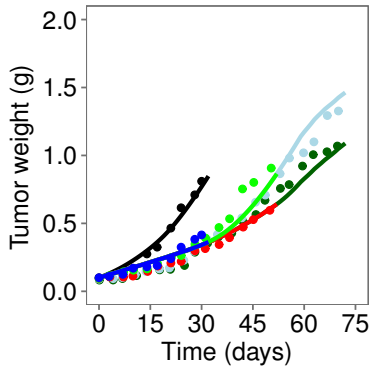

Observed and model predicted tumor weight relative to patient-derived CRC xenograft mice treated with placebo (black) or bevacizumab for 30 days (blue), 50 days (red), 30 days followed by 20 days-break (light green), 70 days (dark green) or 70 days with a 20 days-break between day 30 and 50 (grey).

Appendix D

Supplementary Material to Chapter 5

D.1 Plasma concentration profiles

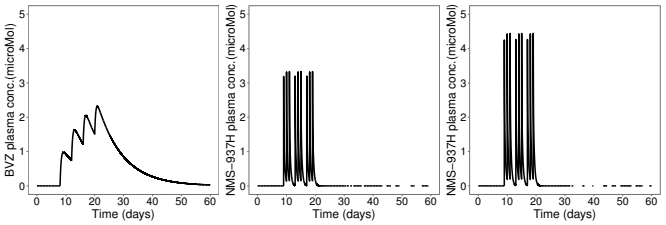

Single agent arms: Plasma concentration profiles in the treated arm a_1 relative to bevacizumab and a_2,a_3 relative to NMS-937H.

D.2 Diagnostic plots for single agent arms

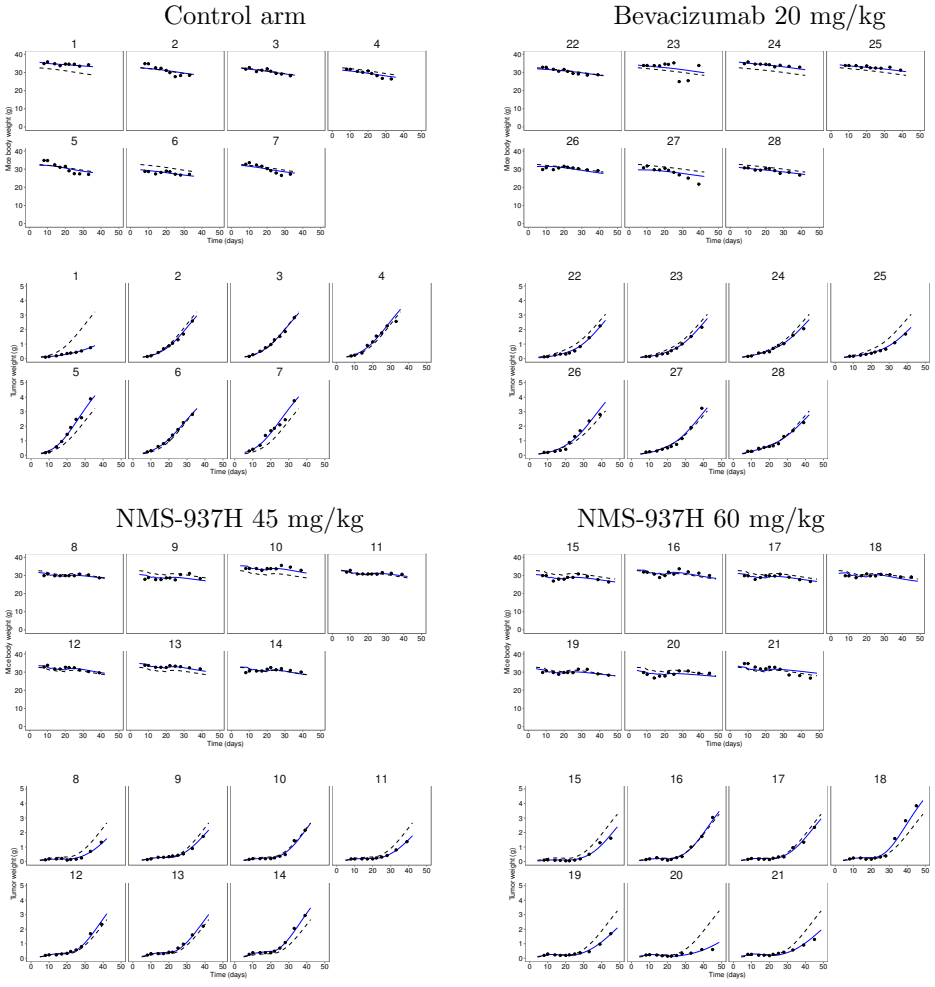

Single agent arms: individual fit plots for controls and single agent treated arms relative to bevacizumab end NMS-937H; black dots represent observed data, solid and dashed lines individual and population model predictions, respectively.

D.2. Diagnostic plots for single agent arms

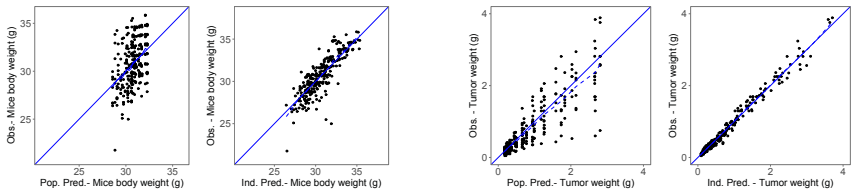

Single agent arms: GOF plots for mice body (left panels) and tumor weight (right panels) relative to controls and single agent treated arms; solid and dashed lines indicate identity line and linear regression fit, respectively.

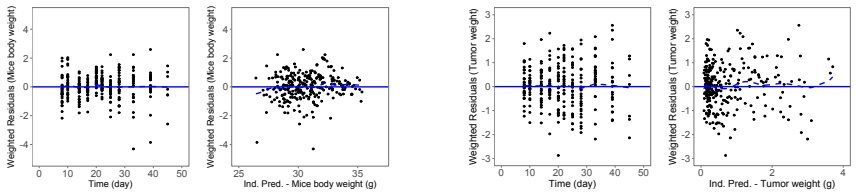

Single agent arms: residual plots for mice body (left panels) and tumor weight (right panels) relative to controls and single agent treated arms.

Appendix E

IVIVC model for the *in silico* bioequivalence of a long-acting release formulation of Progesterone

Health authorities carefully evaluate any change in the batch manufacturing process of a drug before and after regulatory approval. In absence of an adequate level A *in vitro-in vivo* correlation (IVIVC), an *in vivo* bioequivalence study is frequently required [126], increasing drug development costs and time to market.

This work proposes a population modeling approach to establish a level A IVIVC between the *in vitro* release of two batches of Progesterone Vaginal Rings (PVRs), a dosage form designed for the continuous delivery *in vivo*, and the corresponding serum profiles observed during clinical studies. Estimates of the expected *in vivo* relative bioavailability of two tested batches can also be obtained from the

model here proposed.

E.1 Experimental data

E.1.1 *In vitro* data

In vitro data included time courses from 24 hours up to 408 hours of the amount of released Progesterone *in vitro* for two batches of rings (reference batch A and test batch B) manufactured by Italfarmaco S.p.A.. In particular, data at 125, 375, 750, 1500 mg dose levels were available for batch A, only 375 mg data for batch B.

Individual *in vitro* profiles for each dose level of the batch A rings are plotted in Fig. E.1. As you can see, apart from the highest dose level where a minimal variability appears, at all the other doses, the individual profiles overlap almost perfectly.

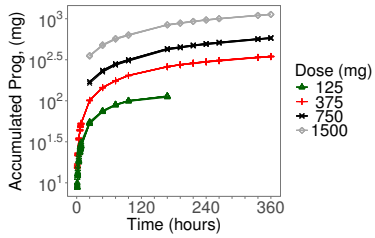

Figure E.1: Individual *in vitro* profiles of the accumulated released Progesterone for all dose levels of batch A rings.

E.1.2 *In vivo* data

In vivo serum level profiles of progesterone were collected during two clinical studies conducted on batch A (46 subjects).

In the first study (Study 1), 30 healthy volunteers were treated with leuprolin acetate (Ginecrin Depot 3.75 mg, AbbVie Spain), a

GnRH agonist, to suppress all endogenous progesterone and estradiol production. Endometrial proliferation was induced with B-estradiol patches (Estradot 75 μg/day, Novartis Farmaceutica) and, after that, PVRs charged with three different dose levels (375, 750, 1500 mg) were inserted to induce endometrial transformation (see Tab. E.1). For PK analysis, serum progesterone was measured at 0.5h, 1h, 2h, 3h, 4h, 6h, 8h, 12h, 18h, 24h, 36h, 48h, 72h, 96h, 120h, 144h, 168h, 216h, 264h, 312h, 380h and 408 hours post-dosing.

The second clinical study (Study 2), performed on PVRs charged with 125 or 375 mg of progesterone, involved other 16 healthy volunteers (see Tab. E.1). The experimental procedure and the sampling time schedule for the PK analysis were the same of Study I.

Table E.1: Information about the progesterone clinical studies.

Clinical study	**Dose level [mg]**	**N. of subject**
Study 1	375	10
Study 1	750	10
Study 1	1500	10
Study 2	125	8
Study 2	350	8

GnRH agonist treatment produces an almost complete suppression of endogenous production. Before ring insertion, median baseline progesterone serum concentration was 0.387 ng/ml (range 0 - 0.84 ng/ml). This compares with expected values of 5 - 50 ng/ml in women during mid-cycle. In order to more accurately assess the serum progesterone concentrations produced after ring insertion, all values were corrected by subtracting their respective baseline values.

For each subject, after ring removal the amount of progesterone still present in the rings was measured. By subtracting this quantity from the dose, the total amount of progesterone released within the observation period was assessed.

E.2 Model structure and identification

The model was developed and, subsequently, identified on individual *in vitro* and *in vivo* data of batch A rings.

E.2.1 *In vitro* release model

For all the doses (125, 375, 750, 1500 mg), *in vitro* progesterone profiles appeared be well described by an immediate release followed by two release phases (a faster and a slower one). Thus the following equation was used to represent the accumulated release profile of progesterone *in vitro* :

$$P_{Vitro}(t) = P_0 + A(1 - e^{-\alpha t}) + B(1 - e^{-\beta t}) \tag{E.1}$$

where the model parameters are P_0 [mg], A [mg], α [1/h], β [1/h], and B=DOSE-A-P_0 [mg]. As can be seen in Fig. E.1, the individual profiles overlaped almost perfectly resulting in a very low inter-individual variability (the average percent coefficient of variation, %CV, is less than 4% for each dose). For this reason, for each dose level, a unique curve was estimated using a pooled data approach. Parameter estimation was performed using the FOCE method in NONMEM. The release curves so obtained were able to accurately describe all profiles observed at the different doses with parameter Coefficient of Variation (CV) values always below 5% (see Tab. E.2). For doses 750 and 1500 mg, the lack of observations in the first 24 hours hampered the estimation of the immediate release parameter P_0, that was therefore kept fixed at the value 9.45 mg, estimated for the 375 mg dose. The fitted accumulated release data are plotted in Fig. E.2, while for each dose level, the GOF plots are reported in Fig. E.3

Table E.2: Parameter estimates for the *in vitro* progesterone release model.

Parameters	**1500 mg**	**750 mg**	**375 mg**	**125 mg**
	Estimate [CV%]	**Estimate [CV%]**	**Estimate [CV%]**	**Estimate [CV%]**
P_0	9.5 [fix]	9.5 [fix]	9.5 [2]	6.62 [5]
A	318 [1]	130 [1]	59.1 [1]	26.1 [3]
$B = \text{DOSE} - A - P_0$	1172.55 [-]	610.55 [-]	306.45 [-]	92.28 [-]
α	0.0656 [3]	0.0721 [1]	0.0846 [1]	0.0843 [4]
β	0.0033 [0]	0.00361 [1]	0.0059 [0]	0.013 [1]
Error (sd)	10.5 [5]	6.55 [10]	2.84 [2]	1.13 [16]

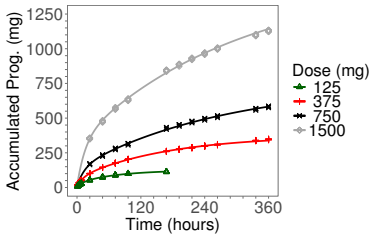

Figure E.2: Plot with the observed individual *in vitro* data and fitted accumulated release profiles for all the dose levels of batch A rings.

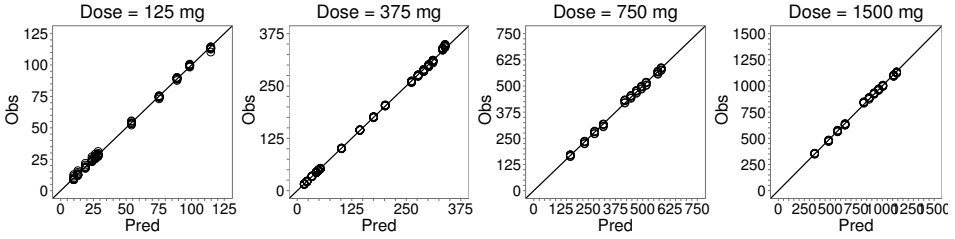

Figure E.3: GOF plots of the estimated P_{Vitro} model .

E.2.2 IVIVC Progesterone ring model

Differently from the *in vitro* situation where, within each experiment, the observed release curves of progesterone were almost superimposable, the *in vivo* serum profiles of progesterone showed a certain

degree of both intra- and inter-subject variability. Hence, the need for a population approach including these variabilities as part of the *in vivo* model. Since the number of subjects treated within each dose level was very limited (see Tab. E.1), instead of developing a single population model for any specific dose level, the *in vivo* data coming from all the dose levels were considered simultaneously.

A possible approach for building up a Level A IVIVC is model the relationship between *in vitro* dissolution and *in vivo* serum concentration. To this aim, one of the key questions to be addressed is the definition, if present, of a connection between the dynamics of the release processes *in vivo* and *in vitro*. For this reason, the *in vivo* model describing the release of progesterone from the rings into the vagina and the passage into the body should have as input function the output of the *in vitro* release model. This would allow predicting the entire *in vivo* time course of progesterone from the *in vitro* data and, in case of changes in the vitro release (including possible different formulation processes), permit to derive the corresponding alterations in the serum profile.

In vivo release model

From a first data analysis, it was evident that, although the observation times of the *in vivo* studies were slightly longer (three days more) compared to the *in vitro* experiments, the amount of progesterone released *in vivo* within the observation period of the studies was definitely smaller than that *in vitro* (see Tab. E.3 and Fig. E.4). For all the doses, the differences were considered possibly due to the the limited solubility of progesterone (approximately 12 ng/ml in water; 4 ng/ml in simulated vaginal fluid) in the finite volume of vaginal fluid (constant volume of 0.5-075 ml, [127]).

Comparing the *in vitro* release to the that observed *in vivo*, it appears that release undergoes an inhibition whose extent increases with

Table E.3: Information about the average progesterone released *in vitro* and *in vivo*.

Dose [mg]	**Average Progesterone released [mg]**	
	In vitro (15 days)	*In vivo* (18 days)
125 mg	114	84.8
375 mg	346.4	117.82
750 mg	582.04	119.3
1500 mg	1129.62	121

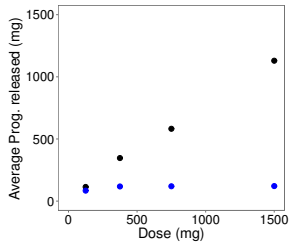

Figure E.4: Comparison of the amount of progesterone released *in vitro* (black dots) and *in vivo* (blue dots).

the dose, probably due to the limited solubility of progesterone in the finite volume of vaginal fluid. This effect can be taken into account introducing a dose dependent delay of the release rate in comparison to the *in vitro* situation. Thus, an inhibition function, a standard I_{max} inhibitory function, was added on rate terms of the *in vitro* accumulated release model P_{Vitro}:

$$P_{Vivo}(t) = P_0 + A(1 - e^{-\alpha t(1/(1+\gamma))}) + B(1 - e^{-\beta t(1/(1+\gamma))}) \qquad \text{(E.2)}$$

where P_0 [mg], A [mg], α [1/h], β [1/h], and B=DOSE-A-P_0 [mg] are the same of the *in vitro* model and the non-negative parameter $\gamma = \gamma(D)$ depends on the dose (D).

For each dose level, an estimate of γ was found imposing the following equality with the average amount of released progesterone mea-

sured at 408 hours (18 days):

$$P_{Vivo}(408h) = P_0 + A(1 - e^{-\alpha 408(1/(1+\gamma))}) + B(1 - e^{-\beta 408(1/(1+\gamma))}) \quad \text{(E.3)}$$

where the parameters are $P_{Vivo}(408h)$ is the sample mean of the *in vivo* accumulated release at 408 hours. The equation was solved using the uniroot() R-function. Estimated values for γ are reported in Tab. E.4 and displayed in Fig. 4.2.

Table E.4: Estimates for the γ parameter.

Dose [mg]	γ [-]
125 mg	5.437
375 mg	11.643
750 mg	29.219
1500 mg	77.601

In order to describe how γ depends on the dose, a second-order polynomial model was used:

$$\gamma(D) = c_0 + c_1 D + c_2 D^2 \quad \text{(E.4)}$$

whose parameters were estimated by ordinary least squares (sd between brackets): $c_0 = 2.1163(1.5829)$, $c_1 = 0.0204(5.1802\text{E-}5)$ and $c_2 = 2.0\text{E-}5(3.0089\text{E-}6)$.

IVIVC population model

The PK model for the serum concentration of progesterone is schematically represented in Fig. E.5, where the *in vivo* release rate $R_{Vivo}(t)$ is the derivative of the accumulated release $P_{Vivo}(t)$, that is:

$$R_{Vivo}(t) = A\alpha(1/(1+\gamma))e^{-\alpha t(1/(1+\gamma))} + B\beta(1/(1+\gamma))e^{-\beta t(1/(1+\gamma))}\,. \quad \text{(E.5)}$$

The serum concentration of progesterone and the amount of progesterone released *in vivo* were simultaneously modeled using a two-compartment model with two first-order absorptions rates (one for the immediate release P_0, K_{a,P_0}, and one for the two exponential phases, P_0, $K_{a,V}$) and a first-order elimination from the central compartment. The parameters of the model are reported in Tab. E.5.

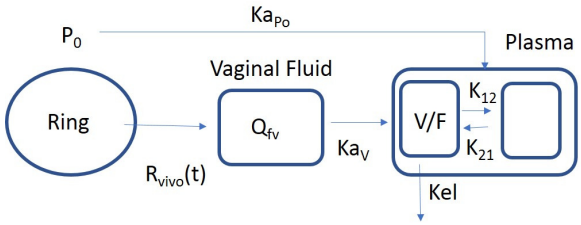

Figure E.5: Schematic representation of the IVIVC P-ring model

Table E.5: Structural parameters of the IVIVC P-ring model.

Parameter	Dimension	Description
P_0	mg	Immediate *in vitro* release
A	mg	Fraction of fast *in vitro* release
B	mg	Fraction of slow *in vitro* release
α	$1/h$	Fast *in vitro* release rate
β	$1/h$	Slow *in vitro* release rate
γ	$-$	*In vivo* inhibition factor, defined as $\gamma = c_0 + c_1 D + c_2 D^2$
$c_0\ c_1\ c_2$	$-$	Polynomial coefficient of the γ function
$K_{a,V}$	$1/h$	Absorption rate constant
K_{a,P_0}	$1/h$	Absorption rate constant for P_0
K_{el}	$1/h$	Elimination rate constant from the central compartment
V/F	L	Volume of distribution
K_{12}	$1/h$	Transfer rate constant from central to peripheral compartment
K_{21}	$1/h$	Transfer rate constant from peripheral to central compartment

Inter-individual variability in the model parameters was assumed to be log-normally distributed, e.g. for $K_{a,V} = POP_{K_{a,V}} e^{ETA_{K_{a,V}}}$ where $POP_{K_{a,V}}$ is the typical value for the population (mean value)

and $ETA_{K_{a,V}}$ is an inter-individual random effect that follows a zero-mean normal distribution with variance $OMEGA_{K_{a,V}}$. Random effects were first considered for all the PK model parameters. However, the high value of the CV for the parameter $OMEGA_{K_{a,V}}$ suggests that it may not be significantly different from zero. Furthermore, the individual estimates obtained for $K_{a,V}$ (not reported) showed a very small inter-subject variability with a CV less than 3%. So, it may be convenient to considered the alternative model where all individuals share the same $K_{a,V}$ ($OMEGA_{K_{a,V}} = 0$). Finally, the individual parameter γ was modeled as $\gamma = c_0 + c_1 D + c_2 D^2 e^{ETA_\gamma}$, where ETA_γ is normal distributed with mean 0 and variance $OMEGA_\gamma$.

Inter-study variability was not included in the model. Separate residual error models were used for the serum concentration and the amount of progesterone released *in vivo*; an additive error model was chosen for both the cases.

Data of serum concentration and amount of released progesterone from *in vivo* studies at dose levels 125, 375, 750 and 1500 mg were used to identify the typical values of the model parameters together with their variance. The estimation was performed using the SAEM method in NONMEM. For each dose level, the parameters P_0, A, B, α and β were kept fixed to the estimates obtained from the *in vitro data* (see Tab. E.2), while the coefficients c_0, c_1 and c_2 of the γ function were fixed to their least squares estimates (see Section E.2.2).

Limited values of CV assessed that population parameters were identified with good precision. In Figs. E.6 and E.7, the observed and model predicted serum concentration profiles of progesterone are plotted for dose level 125, 375, 750 and 1500 mg respectively while the correspondent GOF plots and residual error plots are displayed in Fig. Fig. E.8, stratified on dose level. Note that the individual and population predicted values are in good agreement with the observed serum concentrations, apart from a slight underestimation of higher observed serum concentrations during the first hours. Additionally,

Table E.6: Parameter estimates for the IVIVC P-ring model.

Population parameters		
Parameter [Dimensions]	**Typical values,** POP **[CV%]**	**Inter-individual variance,** $OMEGA$ **[CV%]**
γ [−]	-	0.0579 [12]
$K_{a,V}$ $[1/h]$	0.1990 [24]	-
K_{a,P_0} $[1/h]$	0.7180 [16]	0.2770 [17]
K_{el} $[1/h]$	0.0241 [5]	0.0092 [64]
V $[L]$	3450 [9]	0.0596 [22]
K_{12} $[1/h]$	0.0259 [19]	0.1570 [45]
K_{21} $[1/h]$	0.0264[59]	3.8600 [28]
Residual variability (Variance)		
VAR_{Y1}	0.2040 [2]	-
VAR_{Y2}	0.0002 [71]	-

Individual parameters are given by $P_i = POP_P \exp(ETA_{P,i})$ with POP_P the typical value and ETA_P a random effect normally distributed with zero mean and variance $OMEGA_P$.

residual error plots for serum concentration of progesterone show a symmetric distribution around zero and no systematic residual trends.

In Fig. E.9 the model predictions of the amount of released progesterone are reported together with the observations.

VPCs were used to assess the predictive performance of the *in vivo* model. For each dose 500 individuals were simulated using the model parameter estimates reported in Tab. E.6 with the $SIM ONLYSIMULATION option of NONMEM. The median, 5th and 95th percentiles were chosen for building up the 90% prediction intervals to compare with the observed data. See Fig. E.10 for serum concentrations of progesterone and Fig. E.11 for AUC(0-t).

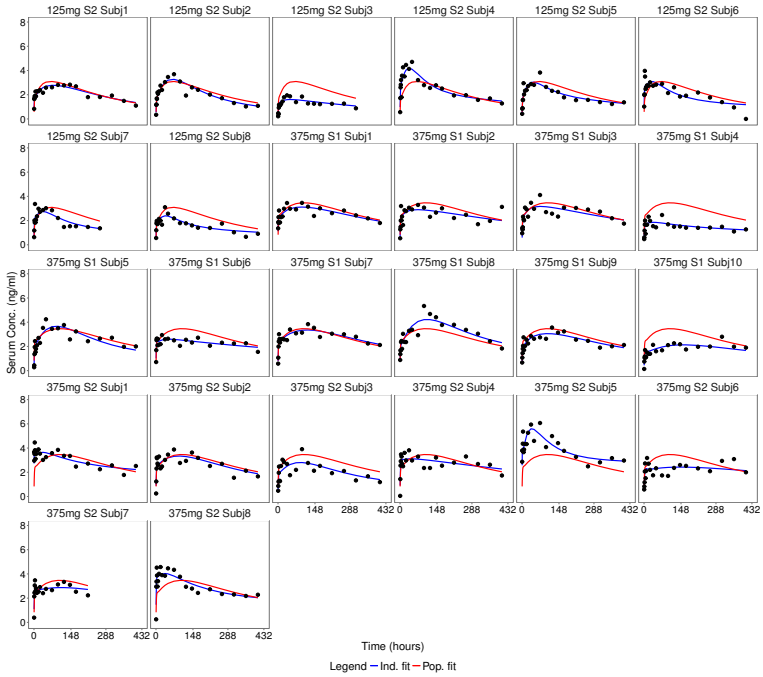

Figure E.6: Individual (blues lines) and population (red lines) fitted serum concentration profiles of progesterone at dose levels 125 and 375 mg together with observations (black dots).

E.3 Assessment of the Level A IVIVC

E.3.1 Internal predictability

To establish the validity of the Level A IVIVC, the predictive performance of the IVIVC P-ring model was assessed. As recommended in the FDA guideline [126], the internal predictability was evaluated considering the model predictions of the serum concentration of progesterone (see Section E.2) and the Prediction Errors (PE)c for AUC and Cmax. The average absolute percent prediction error (%PE) and the %PE for each dose are reported in Tab. E.7 for AUC(0-t) at various

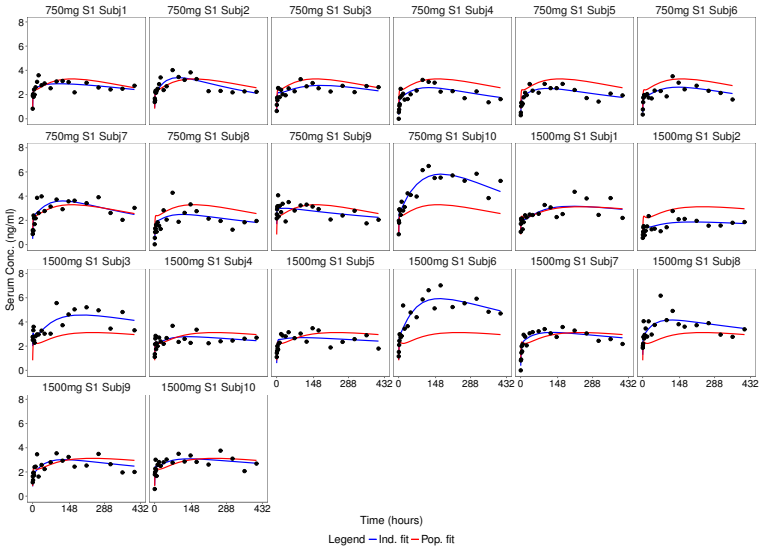

Figure E.7: Individual (blues lines) and population (red lines) fitted serum concentration profiles of progesterone at dose levels 750 and 1500 mg together with observations (black dots).

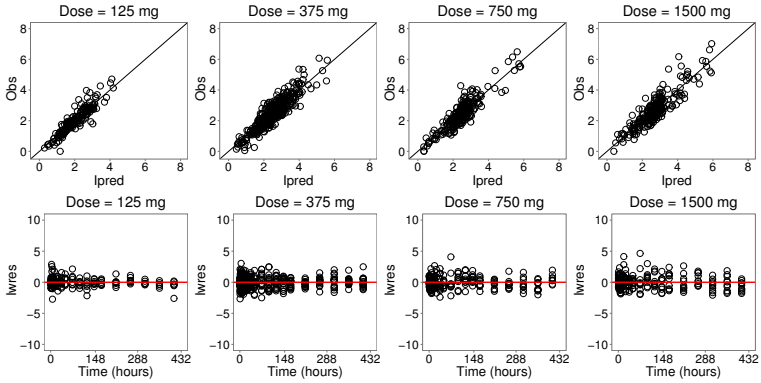

Figure E.8: Diagnostic plots for the progesterone serum concentration stratified on dose levels: the goodness of fit and the residual error plots are reported in the upper and lower panels, respectively.

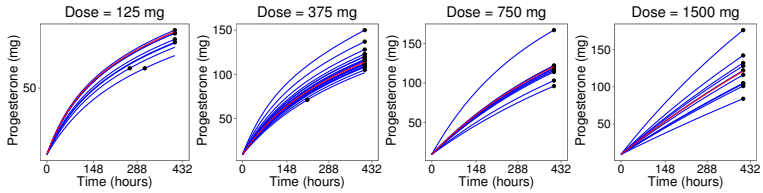

Figure E.9: Amount of progesterone released at the end of the observation period (black dots) together with the corresponding individual (blue lines) and population (red lines) values predicted by the model.

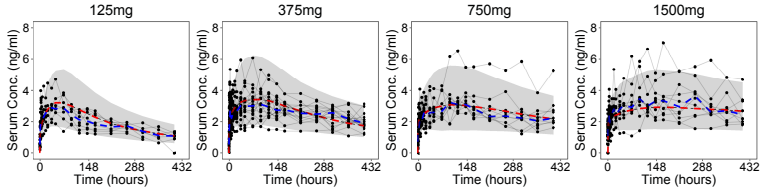

Figure E.10: VPC plots for the the progesterone serum concentration stratified on dose levels. Simulations of the IVIVC model with 90% confidence interval (grey areas) are shown together with progesterone serum concentration data (visual predictive check) for each considered dose levels. The dashed lines show the theoretical median (read) and the experimental median (blue).

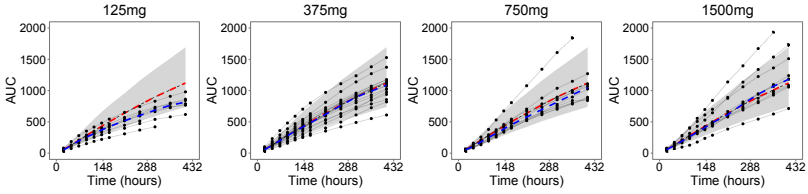

Figure E.11: VPC plots for the the progesterone serum concentration stratified on dose levels. Simulations of the IVIVC model with 90% confidence interval (grey areas) are shown together with progesterone serum concentration data (visual predictive check) for each considered dose levels. The dashed lines show the theoretical median (read) and the experimental median (blue).

sampling times and Cmax.

As one can see from Tab. E.7, the average %PE for AUC(0-408h) is less than 2% for each dose. Furthermore, the %PE for AUC(0-t) at various sampling times is always less than 7% with an average

Table E.7: %PE for AUC(0-t) and Cmax of Progesterone serum concentrations.

Average %PE													
Dose	**AUC(0-t)**												**Cmax**
[mg]	**24h**	**48h**	**72h**	**96h**	**120h**	**144h**	**168h**	**216h**	**264h**	**312h**	**360h**	**408h**	
125 mg	4.53	4.08	3.95	3.72	2.56	1.82	1.51	1.51	1.87	2.19	1.89	1.46	15.57
375 mg	4.54	3.28	4.26	4.39	3.14	2.19	2.02	1.96	1.80	1.61	2.10	1.89	4.56
750 mg	6.12	5.58	3.66	3.57	3.06	3.52	3.68	2.48	1.93	1.78	1.77	1.59	17.36
1500 mg	3.98	1.88	5.04	5.67	3.79	2.49	2.77	2.68	2.38	1.79	1.74	1.53	1.53
Mean	4.79	3.71	4.30	4.34	3.14	2.51	2.50	2.16	1.99	1.85	1.87	1.61	16.41

value under 5%. The average %PE for Cmax is less than 17%; in this case the higher errors are due to the variability of the data. Indeed, as can be calculated from the *in vivo* serum concentration data, the coefficient of variation for the observed Tmax is higher than 75%.

E.3.2 External predictability

Although the number of available cases was limited, in addition to the internal predictability, an attempt for assessing the external predictability of the model was performed. To this aim, the IVIVC P-ring model was identified only on the data relative to the doses 125mg, 750mg and 1500mg while data at 375mg were considered as external dataset. The estimates for coefficient of the γ function are $c_0 = 2.4846$, $c_1 = 0.0212$ and $c_2 = 2E-05$, while the other model parameters are reported Tab. E.8. The differences in the estimated values from the ones previous obtained (Fig. 4.1 and Table 4.5) are due to the reduced number of individuals including in the population on which the model has been identified (28 subjects compared to the previous 46 subjects).

VPC plots were used to assess the predictive performance of the model when confronted with the external dataset at dose 375mg. To this aim, 500 individuals were simulated using the model parameter estimates (Tab. E.8) with the $SIM ONLYSIMULATION option of

Table E.8: Parameter estimates for the IVIVC P-ring model on the internal dataset (125mg, 750mg and 1500mg dose levels).

Population parameters		
Parameter [Dimensions]	**Typical values,** POP **[CV%]**	**Inter-individual variance,** $OMEGA$ **[CV%]**
γ $[-]$	-	0.0592 [19]
$K_{a,V}$ $[1/h]$	0.4430[5]	-
K_{a,P_0} $[1/h]$	0.8370 [25]	0.2870 [28]
K_{el} $[1/h]$	0.0221 [10]	0.014 [84]
V $[L]$	3880[11]	0.0561 [28]
K_{12} $[1/h]$	0.195 [62]	0.2480 [95]
K_{21} $[1/h]$	0.0703[155]	6.7000 [66]
Residual variability (Variance)		
VAR_{Y1}	0.2140 [3]	-
VAR_{Y2}	0.000004 [3]	-

NONMEM. The median, 5th and 95th percentiles, to construct the 90% prediction interval for the simulated data, were plotted and compared to the observed serum concentrations of progesterone and to the observed AUC(0-t) Fig. E.12. The absolute %PE are reported in Tab. E.9 for the average AUC(0-t) at the latest four sampling times (264, 312, 360 and 408 hours) and for Cmax. As can be seen the %PE for AUC is always less than 10% and less than 3% at the end of the experiment. Furthermore, the %PE for the average Cmax is less than 6%.

Table E.9: %PE for average AUC(0-t) and Cmax of Progesterone serum concentrations.

Average %PE				
AUC(0-t)				**Cmax**
264h	**312h**	**360h**	**408h**	
7.36	3.75	3.75	2.95	5.52

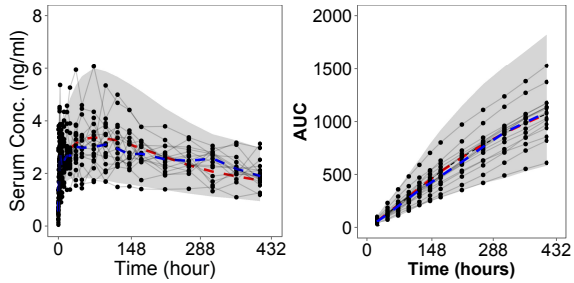

Figure E.12: External VPC plots. Simulations of progesterone serum concentrations (on the left) and amount of released progesterone (on the right) at dose level 375mg performed by the IVIVC P-ring model identified on data relative to doses 125, 750 and 1500mg. The 90% prediction intervals (grey areas), the theoretical median (red dashed line) and the experimental median (blue dashed line) are shown together with the experimental data.

E.4 Model based assessment of the *in vivo* bioequivalence

In addition to the standard Level A IVIVC procedure, the population approach here developed allows to perform simulation studies providing estimates of the relative *in vivo* bioavailability (F=AUCtest/ AUCref) of any new batch tested *in vitro* in comparison to a reference one.

The proposed *in silico* approach for the assessment of the *in vivo* bioequivalence is based on the following steps:

- Identification of the *in vitro* model on the *in vitro* data of the reference batch;
- Identification of the *in vitro* model on the *in vitro* data of the test batch;
- Identification of the IVIVC P-ring model on the *in vivo* data (serum concentration and amount of released progesterone) of the reference batch;

- Simulation of a 500 subject population using the IVIVC P-ring model for the reference batch;
- Simulation of 500 subject population using the IVIVC P-ring model for the test batch using the model parameters identified on reference batch data a part of the *in vitro* parameters identified on the *in vitro* data of the test batch;
- Comparison of the AUC and Cmax of the two batches using the 80-125% bioequivalence criteria.

Note that, In absence of specific information, the intra-individual variability is supposed to be equal to the inter-individual variability, simulating two different population for batch A and B. This is a conservative assumption because the intra-variability is in general expected to be lower than the inter-variability.

Batch A and B at 375 mg level dose were used as reference and test batch in order to illustrate the *in silico* approach proposed. In particular, a first 500 subject population (500 serum progesterone profiles) were generated with the IVIVC P-ring model previously identified on *in vivo* data of batch A (see Section BLABLA); then, an other subject population (500 serum progesterone profiles) were obtained for batch B using the same model parameters apart the *in vitro* parameters that were re-estimated from its *in vitro* release dataset (P_0=17.1mg, A=77.2mg, B=DOSE-A-P_0=280.7mg, α=0.0647 1/h and $\beta = 0.00515$ 1/h). The AUC values of the two populations were compared with the 80-125% criteria; in particular, the *in vivo* relative bioavailability was directly obtained, F=0.913 with 90%CI = [0.878, 0.948].

E.5 Discussion

The objective of this work was the development of a mathematical model able to establish an adequate level A IVIVC in agreement

with the FDA Guidance for Industry (see [1]). This guideline makes specific reference to "Extended Release (ER) Oral Dosage Forms"; although here the model is applied to vaginal rings ER formulations, in absence of IVIVC guidelines for ER forms other than oral, the general rules presented in this guideline were considered applicable also in this context. In particular, it is mentioned that "whatever the method used to establish a Level A IVIVC, the model should predict the entire *in vivo* time course from the *in vitro* data" and, in the following, it is stated that independently from the methodology adopted "A correlation should predict *in vivo* performance accurately and consistently. Once this relationship has been achieved, *in vitro* dissolution can be used confidently as a surrogate for *in vivo* bioequivalence of ER drug products in the situations described below [...]".

In this study different *in vitro* release rates obtained at 125, 375, 750 and 1500mg dose levels were considered. At each dose level the observed progesterone release profiles of the tested rings exhibited biexponential decays that overlapped almost perfectly. Hence, within each dose level all the *in vitro* release time courses were pooled together and fitted by a biexponential model without taking into account inter-individual variability. The curves so obtained were able to describe very well the cumulative release of the *in vitro* data with very precise parameter estimates (CV $< 5\%$). These release functions were then considered as *in vitro* input rates for the *in vivo* part of the model. Differently from the *in vitro* data, the serum progesterone levels showed different profiles among the subjects with a significant intra- and inter-individual variability, thus suggesting the use of a population approach. A comparison of the *in vitro* and the *in vivo* accumulated release at the end of the experiments gave evidence of a decreased release rate *in vivo* compared to that *in vitro*. The ratio of *in vivo* to *in vitro* accumulated release was dose-dependent and decreased with the dose. This non-linear behaviour was very well described by a suitable inhibition function characterized by a dose-

dependent parameter γ. By combining the *in vitro* release with the inhibition function, for any specific dose the appropriate *in vivo* input rate could be computed for the *in vivo* model. The *in vivo* model incorporates two absorption mechanisms, one (K_{a,P_0}) for the immediate progesterone release and the other ($K_{a,V}$) for the remaining part of the release. A two compartment model was assumed for progesterone kinetic in serum. The simultaneous fitting of the *in vivo* parameters yielded very satisfactory results at all doses in terms of both residuals and visual predictive checks. The goodness of fit observed comparing the predicted and observed curves and the very low %PE (percent prediction error) relative to the AUCs confirmed the validity of the model. At any sampling time the average (across all subjects and doses) %PE on AUC(0-t) was less than 5% (Table 4.6). At the latest times (t>144h) the %PE was less than 3% for each dose. A higher error was observed for Cmax whose percent error on average was 16.4%. This was somehow expected in view of the marked variability in the individual serum profiles, with observed Tmax values in the range 3-408 hours. Such a Cmax %PE below 20% was taken as satisfactory even if the guideline mentions a %PE in the 10-20% range as inconclusive. In fact, it has to be considered that this kind of formulation is somehow atypical with respect to guidelines for oral administration.

To further confirm the predictive capability of the model an external validation was set up. The data at dose 375mg were left apart as test dataset and the population *in vivo* model was reestimated using only data at doses 125, 750 and 1500mg. Then, using the *in vitro* model derived from the 375mg data to simulate the *in vitro* release rate, the obtained population model was used to simulate the serum profile of 500 distinct individuals. Validation was performed by means of visual predictive checks (VPCs), the error on the average AUC(0-t) and the error on the average Cmax. In particular, all the subjects fell within the 90% intervals of the VPCs and the %PE on AUCs and Cmax were all below 10%.

Finally, hypothesizing the validity of the Level A IVIVC, a model-based approach for the assessment of *in vivo* bioequivalence was proposed as an alternative to the standard procedure based on the *in vitro* dissolution.

Bibliography

[1] US. Food and Drug Administration. Innovation or stagnation: challenge and opportunity on the critical path to new medical products, 2004. Available online, http://www.fda.gov.

[2] EMA/EFPIA. Modeling and simulation workshop, 2011. Available online, http://www.ema.europa.eu.

[3] Ismail Kola and John Landis. Can the pharmaceutical industry reduce attrition rates? *Nature reviews Drug discovery*, 3(8):711, 2004.

[4] Michael J Waring, John Arrowsmith, Andrew R Leach, Paul D Leeson, Sam Mandrell, Robert M Owen, Garry Pairaudeau, William D Pennie, Stephen D Pickett, Jibo Wang, et al. An analysis of the attrition of drug candidates from four major pharmaceutical companies. *Nature reviews Drug discovery*, 14(7):475, 2015.

[5] John Arrowsmith. Trial watch: Phase II failures: 2008–2010, 2011.

[6] John Arrowsmith. Phase III and submission failures: 2007-2010. *Nature Reviews Drug Discovery*, 10(2):1–2, 2011.

[7] John Arrowsmith and Philip Miller. Trial watch: phase II and phase III attrition rates 2011–2012, 2013.

[8] Michael Hay, David W Thomas, John L Craighead, Celia Economides, and Jesse Rosenthal. Clinical development success rates for investigational drugs. *Nature biotechnology*, 32(1):40, 2014.

[9] Steven M Paul, Daniel S Mytelka, Christopher T Dunwiddie, Charles C Persinger, Bernard H Munos, Stacy R Lindborg, and Aaron L Schacht. How to improve r&d productivity: the pharmaceutical industry's grand challenge. *Nature reviews Drug discovery*, 9(3):203, 2010.

[10] Joseph A DiMasi, Henry G Grabowski, and Ronald W Hansen. Innovation in the pharmaceutical industry: new estimates of R&D costs. *Journal of health economics*, 47:20–33, 2016.

[11] Lawrence J Lesko, Malcolm Rowland, Carl C Peck, and Terrence F Blaschke. Optimizing the science of drug development: opportunities for better candidate selection and accelerated evaluation in humans. *The Journal of Clinical Pharmacology*, 40(8):803–814, 2000.

[12] Ene I Ette and Paul J Williams. *Pharmacometrics: the science of quantitative pharmacology*. John Wiley & Sons, 2013.

[13] SAG Visser, E Manolis, M Danhof, and T Kerbusch. Modeling and simulation at the interface of nonclinical and early clinical drug development. *CPT: pharmacometrics & systems pharmacology*, 2(2):1–3, 2013.

[14] SF Marshall, R Hemmings, F Josephson, MO Karlsson, M Posch, and J-L Steimer. Modeling and simulation to optimize the design and analysis of confirmatory trials, characterize risk–benefit, and support label claims. *CPT: pharmacometrics & systems pharmacology*, 2(2):1–3, 2013.

[15] L Harnisch, T Shepard, G Pons, and O Della Pasqua. Modeling and simulation as a tool to bridge efficacy and safety data in special populations. *CPT: pharmacometrics & systems pharmacology*, 2(2):1–4, 2013.

[16] A Staab, E Rook, M Maliepaard, L Aarons, and C Benson. Modeling and simulation in clinical pharmacology and dose finding. *CPT: pharmacometrics & systems pharmacology*, 2(2):1–3, 2013.

[17] Carl C Peck, William H Barr, Leslie Z Benet, Jerry Collins, Robert E Desjardins, Daniel E Furst, John G Harter, Gerhard Levy, Thomas Ludden, John H Rodman, et al. Opportunities for integration of pharmacokinetics, pharmacodynamics, and toxicokinetics in rational drug development. *Journal of pharmaceutical sciences*, 81(6):605–610, 1992.

[18] Lewis B Sheiner. Learning versus confirming in clinical drug development. *Clinical Pharmacology & Therapeutics*, 61(3):275–291, 1997.

[19] RL Lalonde, KG Kowalski, MM Hutmacher, W Ewy, DJ Nichols, PA Milligan, BW Corrigan, PA Lockwood, SA Marshall, LJ Benincosa, et al. Model-based drug development. *Clinical Pharmacology & Therapeutics*, 82(1):21–32, 2007.

[20] Ji Zhang and Betty HC Cheng. Model-based development of dynamically adaptive software. In *Proceedings of the 28th in-*

ternational conference on Software engineering, pages 371–380. ACM, 2006.

[21] Carl-Fredrik Burman, Bengt Hamrén, and Per Olsson. Modelling and simulation to improve decision-making in clinical development. *Pharmaceutical Statistics*, 4(1):47–58, 2005.

[22] Bruno G Reigner, Peter EO Williams, Indra H Patel, Jean-Louis Steimer, Carl Peck, and Peter van Brummelen. An evaluation of the integration of pharmacokinetic and pharmacodynamic principles in clinical drug development. *Clinical pharmacokinetics*, 33(2):142–152, 1997.

[23] Jenny Y Chien, Stuart Friedrich, Michael A Heathman, Dinesh P de Alwis, and Vikram Sinha. Pharmacokinetics/pharmacodynamics and the stages of drug development: role of modeling and simulation. *The AAPS journal*, 7(3):E544–E559, 2005.

[24] PA Milligan, MJ Brown, B Marchant, SW Martin, PH Van Der Graaf, N Benson, G Nucci, DJ Nichols, RA Boyd, JW Mandema, et al. Model-based drug development: a rational approach to efficiently accelerate drug development. *Clinical Pharmacology & Therapeutics*, 93(6):502–514, 2013.

[25] SAG Visser, DP De Alwis, T Kerbusch, JA Stone, and SRB Allerheiligen. Implementation of quantitative and systems pharmacology in large pharma. *CPT: pharmacometrics & systems pharmacology*, 3(10):1–10, 2014.

[26] Lucas Moreno and Andrew DJ Pearson. How can attrition rates be reduced in cancer drug discovery?, 2013.

[27] Stephen E Gould, Melissa R Junttila, and Frederic J de Sauvage. Translational value of mouse models in oncology drug development. *Nature medicine*, 21(5):431, 2015.

[28] DL Woodhouse. Chemotherapy investigations in cancer. with reference to the influence of certain organic dibasic acids, diamino compounds and nitro compounds on tumors in mice. *Cancer research*, 7(6):398–401, 1947.

[29] Ming Liu and Daniel Hicklin. Human tumor xenograft efficacy models. In *Tumor models in cancer research*, pages 99–124. Springer, 2011.

[30] LR Kelland. "of mice and men": values and liabilities of the athymic nude mouse model in anticancer drug development. *European Journal of Cancer*, 40(6):827–836, 2004.

[31] Melinda G Hollingshead. Antitumor efficacy testing in rodents. *JNCI: Journal of the National Cancer Institute*, 100(21):1500–1510, 2008.

[32] Joohee Jung. Human tumor xenograft models for preclinical assessment of anticancer drug development. *Toxicological research*, 30(1):1, 2014.

[33] Monica Simeoni, Giuseppe De Nicolao, Paolo Magni, Maurizio Rocchetti, and Italo Poggesi. Modeling of human tumor xenografts and dose rationale in oncology. *Drug Discovery Today: Technologies*, 10(3):e365–e372, 2013.

[34] Edward A Sausville and Angelika M Burger. Contributions of human tumor xenografts to anticancer drug development. *Cancer research*, 66(7):3351–3354, 2006.

[35] Letizia Carrara, Silvia Maria Lavezzi, Elisa Borella, Giuseppe De Nicolao, Paolo Magni, and Italo Poggesi. Current mathematical models for cancer drug discovery. *Expert opinion on drug discovery*, 12(8):785–799, 2017.

[36] Apexa Bernard, Holly Kimko, Dinesh Mital, and Italo Poggesi. Mathematical modeling of tumor growth and tumor growth inhibition in oncology drug development. *Expert opinion on drug metabolism & toxicology*, 8(9):1057–1069, 2012.

[37] B Ribba, Nick H Holford, P Magni, I Trocóniz, I Gueorguieva, P Girard, C Sarr, M Elishmereni, C Kloft, and Lena E Friberg. A review of mixed-effects models of tumor growth and effects of anticancer drug treatment used in population analysis. *CPT: pharmacometrics & systems pharmacology*, 3(5):1–10, 2014.

[38] Sébastien Benzekry, Clare Lamont, Afshin Beheshti, Amanda Tracz, John ML Ebos, Lynn Hlatky, and Philip Hahnfeldt. Classical mathematical models for description and prediction of experimental tumor growth. *PLoS computational biology*, 10(8):e1003800, 2014.

[39] Peter L Bonate. Modeling tumor growth in oncology. In *Pharmacokinetics in drug development*, pages 1–19. Springer, 2011.

[40] Monica Simeoni, Paolo Magni, Cristiano Cammia, Giuseppe De Nicolao, Valter Croci, Enrico Pesenti, Massimiliano Germani, Italo Poggesi, and Maurizio Rocchetti. Predictive pharmacokinetic-pharmacodynamic modeling of tumor growth kinetics in xenograft models after administration of anticancer agents. *Cancer research*, 64(3):1094–1101, 2004.

[41] M Rocchetti, M Simeoni, E Pesenti, G De Nicolao, and I Poggesi. Predicting the active doses in humans from animal stud-

ies: a novel approach in oncology. *European Journal of Cancer*, 43(12):1862–1868, 2007.

[42] Evelyn D Lobo and Joseph P Balthasar. Pharmacodynamic modeling of chemotherapeutic effects: application of a transit compartment model to characterize methotrexate effects in vitro. *AAPs PharmSci*, 4(4):212–222, 2002.

[43] Kim Stuyckens, Juan Jose Perez Ruixo, An Vermeulen, and Eugene Cox. Modeling drug effects and resistance development on tumor growth dynamics. *Population Approach Group in Europe (PAGE), Kobenhavn, Denmark*, 2007.

[44] Maiara Cássia Pigatto, Renatha Menti Roman, Letizia Carrara, Andréia Buffon, Paolo Magni, and Teresa Dalla Costa. Pharmacokinetic/pharmacodynamic modeling of etoposide tumor growth inhibitory effect in walker-256 tumor-bearing rat model using free intratumoral drug concentrations. *European Journal of Pharmaceutical Sciences*, 97:70–78, 2017.

[45] A Ouerdani, H Struemper, AB Suttle, D Ouellet, and B Ribba. Preclinical modeling of tumor growth and angiogenesis inhibition to describe pazopanib clinical effects in renal cell carcinoma. *CPT: pharmacometrics & systems pharmacology*, 4(11):660–668, 2015.

[46] S Wilson, M Tod, A Ouerdani, A Emde, Y Yarden, A Adda Berkane, S Kassour, MX Wei, G Freyer, B You, et al. Modeling and predicting optimal treatment scheduling between the antiangiogenic drug sunitinib and irinotecan in preclinical settings. *CPT: Pharmacometrics & Systems Pharmacology*, 4(12):720–727, 2015.

[47] Benjamin Ribba, Emmanuel Watkin, Michel Tod, Pascal Girard, Emmanuel Grenier, Benoît You, Enrico Giraudo, and Gilles Freyer. A model of vascular tumour growth in mice combining longitudinal tumour size data with histological biomarkers. *European Journal of Cancer*, 47(3):479–490, 2011.

[48] Maurizio Rocchetti, Massimiliano Germani, Francesca Del Bene, Italo Poggesi, Paolo Magni, Enrico Pesenti, and Giuseppe De Nicolao. Predictive pharmacokinetic–pharmacodynamic modeling of tumor growth after administration of an anti-angiogenic agent, bevacizumab, as single-agent and combination therapy in tumor xenografts. *Cancer chemotherapy and pharmacology*, 71(5):1147–1157, 2013.

[49] Gilbert Koch, Antje Walz, Gezim Lahu, and Johannes Schropp. Modeling of tumor growth and anticancer effects of combination therapy. *Journal of pharmacokinetics and pharmacodynamics*, 36(2):179–197, 2009.

[50] Mengyao Li, Hanqing Li, Xiaoliang Cheng, Xipei Wang, Liang Li, Tianyan Zhou, and Wei Lu. Preclinical pharmacokinetic/pharmacodynamic models to predict schedule-dependent interaction between erlotinib and gemcitabine. *Pharmaceutical research*, 30(5):1400–1408, 2013.

[51] M Rocchetti, F Del Bene, M Germani, F Fiorentini, I Poggesi, E Pesenti, P Magni, and G De Nicolao. Testing additivity of anticancer agents in pre-clinical studies: a pk/pd modelling approach. *European Journal of Cancer*, 45(18):3336–3346, 2009.

[52] Nadia Terranova, Massimiliano Germani, Francesca Del Bene, and Paolo Magni. A predictive pharmacokinetic–pharmacodynamic model of tumor growth kinetics in xenograft

mice after administration of anticancer agents given in combination. *Cancer chemotherapy and pharmacology*, 72(2):471–482, 2013.

[53] Lance A Liotta. *Influence of tumor development on the host*, volume 3. Springer Science & Business Media, 2012.

[54] Tomoyoshi Aoyagi, Krista P Terracina, Ali Raza, Hisahiro Matsubara, and Kazuaki Takabe. Cancer cachexia, mechanism and treatment. *World journal of gastrointestinal oncology*, 7(4):17, 2015.

[55] Kenneth Fearon, Jann Arends, and Vickie Baracos. Understanding the mechanisms and treatment options in cancer cachexia. *Nature reviews Clinical oncology*, 10(2):90, 2013.

[56] Vickie E Baracos, Lisa Martin, Murray Korc, Denis C Guttridge, and Kenneth CH Fearon. Cancer-associated cachexia. *Nature Reviews Disease Primers*, 4:17105, 2018.

[57] Vickie E Baracos. Bridging the gap: are animal models consistent with clinical cancer cachexia? *Nature reviews. Clinical oncology*, 15(4):197, 2018.

[58] IMM Van Leeuwen, FDL Kelpin, and SALM Kooijman. A mathematical model that accounts for the effects of caloric restriction on body weight and longevity. *Biogerontology*, 3(6):373–381, 2002.

[59] IMM Van Leeuwen, C Zonneveld, and SALM Kooijman. The embedded tumour: host physiology is important for the evaluation of tumour growth. *British journal of cancer*, 89(12):2254, 2003.

[60] P Workman, EO Aboagye, F Balkwill, A Balmain, Gail Bruder, DJ Chaplin, JA Double, J Everitt, DAH Farningham, MJ Glennie, et al. Guidelines for the welfare and use of animals in cancer research. *British journal of cancer*, 102(11):1555, 2010.

[61] Nadia Terranova, Elena Maria Tosca, Enrico Pesenti, Maurizio Rocchetti, and Paolo Magni. Modeling tumor growth inhibition and toxicity outcome afteradministration of anticancer agents in xenograft mice: a dynamic energy budget (deb) approach. *Journal of Theoretical Biology*, 450:1–14, 2018.

[62] SALM Kooijman. *Dynamic energy budgets in biological systems*. Cambridge University Press, 1993.

[63] S.A.L. M. Kooijman. *Dynamic energy and mass budgets in biological systems*. Cambridge university press, 2000.

[64] SS.A.L. M. Kooijman. Quantitative aspects of metabolic organization: a discussion of concepts. *Philosophical Transactions of the Royal Society of London B: Biological Sciences*, 356(1407):331–349, 2001.

[65] P Magni, M Simeoni, I Poggesi, M Rocchetti, and G De Nicolao. A mathematical model to study the effects of drugs administration on tumor growth dynamics. *Mathematical biosciences*, 200(2):127–151, 2006.

[66] Alberto d'Onofrio and Alberto Gandolfi. Tumour eradication by antiangiogenic therapy: analysis and extensions of the model by hahnfeldt et al. (1999). *Mathematical Biosciences*, 191(2):159 – 184, 2004.

[67] Sten Friberg and Stefan Mattson. On the growth rates of human malignant tumors: implications for medical decision making. *Journal of surgical oncology*, 65(4):284–297, 1997.

[68] Silvio Garattini. Pharmacokinetics in cancer chemotherapy. *European Journal of Cancer*, 43(2):271–282, 2007.

[69] Olivier Trédan, Carlos M Galmarini, Krupa Patel, and Ian F Tannock. Drug resistance and the solid tumor microenvironment. *Journal of the National Cancer Institute*, 99(19):1441–1454, 2007.

[70] Rama Grantab, Shankar Sivananthan, and Ian F Tannock. The penetration of anticancer drugs through tumor tissue as a function of cellular adhesion and packing density of tumor cells. *Cancer research*, 66(2):1033–1039, 2006.

[71] Sanjeev Kaul, Linus N Igwemezie, David J Stewart, Scott Z Fields, Michael Kosty, Nathan Levithan, Ronald Bukowski, David Gandara, Glenwood Goss, and Peter O'Dwyer. Pharmacokinetics and bioequivalence of etoposide following intravenous administration of etoposide phosphate and etoposide in patients with solid tumors. *Journal of clinical oncology*, 13(11):2835–2841, 1995.

[72] Giuseppe Toffoli, Giuseppe Corona, Roberto Sorio, Isabelle Robieux, Barbara Basso, Anna Maria Colussi, and Mauro Boiocchi. Population pharmacokinetics and pharmacodynamics of oral etoposide. *British journal of clinical pharmacology*, 52(5):511–519, 2001.

[73] Brazil. Lei 11.794/2008: Procedimentos para uso cientifico de animais. Diario Oficial da Uniao, Secao 1 de 9 de outubro de 2008, 2008. CXLV, 196, 1-2.

[74] Brazil. Ministerio de ciencia, tecnologia e inovacao conselho nacional de controle de experimentacao animal. - CONCEA. Dire-

triz Brasileira para o cuidado e a utilizacao de animais para fins cientificos e didaticos- DBCA. Brasilia - DF, 2013.

[75] NCI. 2012 frederick ACUC guidelines involving experimental neoplasia proposals in mice and rats. https://es.scribd.com/document/139069470/ACUC14(accessed 0.10.3.14).

[76] Maiara Cássia Pigatto, Bibiana Verlindo de Araujo, Bruna Gaelzer Silva Torres, Stephan Schmidt, Paolo Magni, and Teresa Dalla Costa. Population pharmacokinetic modeling of etoposide free concentrations in solid tumor. *Pharmaceutical research*, 33(7):1657–1670, 2016.

[77] Tove Tuntland, Brian Ethell, Takatoshi Kosaka, Francesca Blasco, Richard Xu Zang, Monish Jain, Ty Gould, and Keith Hoffmaster. Implementation of pharmacokinetic and pharmacodynamic strategies in early research phases of drug discovery and development at novartis institute of biomedical research. *Frontiers in pharmacology*, 5:174, 2014.

[78] Xiuguo Li, Jae-Kyung Yun, and Jun-Shik Choi. Effects of morin on the pharmacokinetics of etoposide in rats. *Biopharmaceutics & drug disposition*, 28(3):151–156, 2007.

[79] Chong-Ki Lee, Sung-Hwan Ki, and Jun-Shik Choi. Effects of oral curcumin on the pharmacokinetics of intravenous and oral etoposide in rats: possible role of intestinal cyp3a and p-gp inhibition by curcumin. *Biopharmaceutics & drug disposition*, 32(4):245–251, 2011.

[80] Lixoft. Monolix version 2016r. http://lixoft.com/products/monolix/.

[81] Marc Lavielle. *Mixed effects models for the population approach: models, tasks, methods and tools*. CRC press, 2014.

[82] Ian F Tannock, Carol M Lee, Jonathon K Tunggal, David SM Cowan, and Merrill J Egorin. Limited penetration of anticancer drugs through tumor tissue: a potential cause of resistance of solid tumors to chemotherapy. *Clinical cancer research*, 8(3):878–884, 2002.

[83] Judah Folkman. Role of angiogenesis in tumor growth and metastasis. In *Seminars in oncology*, volume 29, pages 15–18. Elsevier, 2002.

[84] Michael Papetti and Ira M Herman. Mechanisms of normal and tumor-derived angiogenesis. *American Journal of Physiology-Cell Physiology*, 282(5):C947–C970, 2002.

[85] Judah Folkman. Tumor angiogenesis: therapeutic implications. *New england journal of medicine*, 285(21):1182–1186, 1971.

[86] Judah Folkman and Michael Klagsbrun. Angiogenic factors. *Science*, 235(4787):442–447, 1987.

[87] Napoleone Ferrara. VEGF and the quest for tumour angiogenesis factors. *Nature Reviews Cancer*, 2(10):795, 2002.

[88] Napoleone Ferrara, Kenneth J Hillan, Hans-Peter Gerber, and William Novotny. Discovery and development of bevacizumab, an anti-vegf antibody for treating cancer. *Nature reviews Drug discovery*, 3(5):391, 2004.

[89] Napoleone Ferrara, Kenneth J Hillan, and William Novotny. Bevacizumab (avastin), a humanized anti-vegf monoclonal antibody for cancer therapy. *Biochemical and biophysical research communications*, 333(2):328–335, 2005.

[90] Vicki L Goodman, Edwin P Rock, Ramzi Dagher, Roshni P Ramchandani, Sophia Abraham, Jogarao VS Gobburu, Brian P Booth, S Leigh Verbois, David E Morse, Cheng Yi Liang, et al. Approval summary: sunitinib for the treatment of imatinib refractory or intolerant gastrointestinal stromal tumors and advanced renal cell carcinoma. *Clinical Cancer Research*, 13(5):1367–1373, 2007.

[91] Robert C Kane, Ann T Farrell, Haleh Saber, Shenghui Tang, Gene Williams, Josephine M Jee, Chengyi Liang, Brian Booth, Nallaperumal Chidambaram, David Morse, et al. Sorafenib for the treatment of advanced renal cell carcinoma. *Clinical Cancer Research*, 12(24):7271–7278, 2006.

[92] Alexander RA Anderson and MAJ Chaplain. Continuous and discrete mathematical models of tumor-induced angiogenesis. *Bulletin of mathematical biology*, 60(5):857–899, 1998.

[93] A D'Onofrio, A Gandolfi, and A Rocca. The dynamics of tumour–vasculature interaction suggests low-dose, time-dense anti-angiogenic schedulings. *Cell proliferation*, 42(3):317–329, 2009.

[94] Philip Hahnfeldt, Dipak Panigrahy, Judah Folkman, and Lynn Hlatky. Tumor development under angiogenic signaling: a dynamical theory of tumor growth, treatment response, and postvascular dormancy. *Cancer research*, 59(19):4770–4775, 1999.

[95] Floriane Lignet, Sébastien Benzekry, Shelby Wilson, Frédérique Billy, Olivier Saut, Michel Tod, Benoit You, A Adda Berkane, S Kassour, MX Wei, et al. Theoretical investigation of the efficacy of antiangiogenic drugs combined to chemotherapy in xenografted mice. *Journal of theoretical biology*, 320:86–99, 2013.

[96] Andrey V Kolobov, Vladimir V Gubernov, and Maxim B Kuznetsov. The study of antitumor efficacy of bevacizumab antiangiogenic therapy using a mathematical model. *Russian Journal of Numerical Analysis and Mathematical Modelling*, 30(5):289–298, 2015.

[97] AVASTIN: EPAR Scientific discussion. European Medicine Agency.

[98] Yvonne S Lin, Cindy Nguyen, Jose-Luis Mendoza, Enrique Escandon, David Fei, Y Gloria Meng, and Nishit B Modi. Preclinical pharmacokinetics, interspecies scaling, and tissue distribution of a humanized monoclonal antibody against vascular endothelial growth factor. *Journal of Pharmacology and Experimental Therapeutics*, 288(1):371–378, 1999.

[99] Feng R Luo, Zheng Yang, Huijin Dong, Amy Camuso, Kelly McGlinchey, Krista Fager, Christine Flefleh, David Kan, Ivan Inigo, Stephen Castaneda, et al. Prediction of active drug plasma concentrations achieved in cancer patients by pharmacodynamic biomarkers identified from the geo human colon carcinoma xenograft model. *Clinical cancer research*, 11(15):5558–5565, 2005.

[100] JD Sato, T Kawamoto, AD Le, J Mendelsohn, J Polikoff, and GH Sato. Biological effects in vitro of monoclonal antibodies to human epidermal growth factor receptors. *Molecular biology & medicine*, 1(5):511–529, 1983.

[101] Anne M Ryan, Dorothy Bates Eppler, Kelly E Hagler, Richard H Bruner, Peter J Thomford, Robert L Hall, George M Shopp, and Charles A O'neill. Preclinical safety evaluation of rhumabvegf, an antiangiogenic humanized monoclonal antibody. *Toxicologic pathology*, 27(1):78–86, 1999.

[102] Gabriele Bergers and Douglas Hanahan. Modes of resistance to anti-angiogenic therapy. *Nature Reviews Cancer*, 8(8):592, 2008.

[103] Han Shen and Kerrie L McDonald. The complexities of resistance to bevacizumab. *Journal of Cancer Therapy*, 3(05):491, 2012.

[104] Kathy D Miller, Christopher J Sweeney, and George W Sledge. Can tumor angiogenesis be inhibited without resistance? In *Mechanisms of angiogenesis*, pages 95–112. Springer, 2005.

[105] KD Miller, CJ Sweeney, and GW Sledge. The snark is a boojum: the continuing problem of drug resistance in the antiangiogenic era. *Annals of Oncology*, 14(1):20–28, 2003.

[106] Robert S Kerbel, Joanne Yu, Jennifer Tran, Shan Man, Alicia Viloria-Petit, Giannoula Klement, Brenda L Coomber, and Janusz Rak. Possible mechanisms of acquired resistance to anti-angiogenic drugs: implications for the use of combination therapy approaches. *Cancer and Metastasis Reviews*, 20(1-2):79–86, 2001.

[107] Yoshiro Itatani, Kenji Kawada, Takamasa Yamamoto, and Yoshiharu Sakai. Resistance to antiangiogenic therapy in cancer alterations to anti VEGF pathway. *International journal of molecular sciences*, 19(4):1232, 2018.

[108] Selma Becherirat, Fatemeh Valamanesh, Mojgan Karimi, Anne-Marie Faussat, Jean-Marie Launay, Cynthia Pimpie, Amu Therwath, and Marc Pocard. Discontinuous schedule of bevacizumab in colorectal cancer induces accelerated tumor growth and phenotypic changes. *Translational oncology*, 11(2):406–415, 2018.

[109] Signe R Michaelsen, Mikkel Staberg, Henriette Pedersen, Kamilla E Jensen, Wiktor Majewski, Helle Broholm, Mette K Nedergaard, Christopher Meulengracht, Thomas Urup, Mette Villingshøj, et al. VEGF-C sustains VEGFR2 activation under bevacizumab therapy and promotes glioblastoma maintenance. *Neuro-oncology*, 2018.

[110] Oriol Casanovas, Daniel J Hicklin, Gabriele Bergers, and Douglas Hanahan. Drug resistance by evasion of antiangiogenic targeting of vegf signaling in late-stage pancreatic islet tumors. *Cancer cell*, 8(4):299–309, 2005.

[111] Giannoula Klement, Sylvain Baruchel, Janusz Rak, Shan Man, Katherine Clark, Daniel J Hicklin, Peter Bohlen, and Robert S Kerbel. Continuous low-dose therapy with vinblastine and vegf receptor-2 antibody induces sustained tumor regression without overt toxicity. *The Journal of clinical investigation*, 105(8):R15–R24, 2000.

[112] Julia Glade Bender, Erin M Cooney, Jessica J Kandel, and Darrell J Yamashiro. Vascular remodeling and clinical resistance to antiangiogenic cancer therapy. *Drug Resistance Updates*, 7(4-5):289–300, 2004.

[113] Christopher W Pugh and Peter J Ratcliffe. Regulation of angiogenesis by hypoxia: role of the hif system. *Nature medicine*, 9(6):677, 2003.

[114] Farbod Shojaei and Napoleone Ferrara. Antiangiogenic therapy for cancer: an update. *The Cancer Journal*, 13(6):345–348, 2007.

[115] Ilaria Fuso Nerini, Marta Cesca, Francesca Bizzaro, and Raffaella Giavazzi. Combination therapy in cancer: effects of an-

giogenesis inhibitors on drug pharmacokinetics and pharmacodynamics. *Chinese journal of cancer*, 35(1):61, 2016.

[116] Rakesh K Jain. Normalizing tumor vasculature with anti-angiogenic therapy: a new paradigm for combination therapy. *Nature medicine*, 7(9):987, 2001.

[117] Ian Kasman, Anil Bagri, Judy Mak, Franklin Peale, Rick Carano, Jed Ross, Leanne Berry, Young Shin, Patrick Rudewicz, Cary Austin, et al. Mechanistic evaluation of the combination effect of anti-vegf and chemotherapy, 2008.

[118] Jie Ma and David J Waxman. Combination of antiangiogenesis with chemotherapy for more effective cancer treatment. *Molecular cancer therapeutics*, 7(12):3670–3684, 2008.

[119] Tim Cardilin, Joachim Almquist, Mats Jirstrand, Alexandre Sostelly, Christiane Amendt, Samer El Bawab, and Johan Gabrielsson. Tumor static concentration curves in combination therapy. *The AAPS journal*, 19(2):456–467, 2017.

[120] MB Kuznetsov and AV Kolobov. Optimization of combined antitumor chemotherapy with bevacizumab by means of mathematical modeling. In *Trends in Biomathematics: Modeling, Optimization and Computational Problems*, pages 347–363. Springer, 2018.

[121] Karl Brendel, Emmanuelle Comets, Céline Laffont, and France Mentré. Evaluation of different tests based on observations for external model evaluation of population analyses. *Journal of pharmacokinetics and pharmacodynamics*, 37(1):49–65, 2010.

[122] Emmanuelle Comets, Karl Brendel, and France Mentré. Model evaluation in nonlinear mixed effect models, with applications to

pharmacokinetics. *Journal de la Société Française de Statistique*, 151(1):106–128, 2010.

[123] THT Nguyen, M-S Mouksassi, Nicholas Holford, N Al-Huniti, I Freedman, Andrew C Hooker, J John, Mats O Karlsson, DR Mould, JJ Pérez Ruixo, et al. Model evaluation of continuous data pharmacometric models: metrics and graphics. *CPT: pharmacometrics & systems pharmacology*, 6(2):87–109, 2017.

[124] Emmanuelle Comets, Karl Brendel, and France Mentré. Computing normalised prediction distribution errors to evaluate nonlinear mixed-effect models: the npde add-on package for R. *Computer methods and programs in biomedicine*, 90(2):154–166, 2008.

[125] Barbara Valsasina, Italo Beria, Cristina Alli, Rachele Alzani, Nilla Avanzi, Dario Ballinari, Paolo Cappella, Michele Caruso, Alessia Casolaro, Antonella Ciavolella, et al. NMS-P937, an orally available, specific, small molecule polo-like kinase 1 inhibitor with antitumor activity in solid and haematological malignancies. *Molecular cancer therapeutics*, pages molcanther–0765, 2012.

[126] US. Food and Drug Administration. Guidance for industry. extended release oral dosage forms: development, evaluation and application of in vitro in vivo correlationsinnovation or stagnation: challenge and opportunity on the critical path to new medical products, 1997. Available online, http://www.fda.gov.

[127] Andreas Bernkop-Schnürch and Margit Hornof. Intravaginal drug delivery systems. *American Journal of Drug Delivery*, 1(4):241–254, 2003.

List of publications

Articles in peer reviewed journals

- N. Terranova, **E.M. Tosca**, E. Pesenti, M. Rocchetti, P. Magni. *Modeling tumor growth inhibition and toxicity outcome after administration of anticancer agents in xenograft mice: A Dynamic Energy Budget (DEB) approach.*, Journal of Theoretical Biology

- **E.M. Tosca**, M. C. Pigatto, T. Dalla Costa, P. Magni *A population Dynamic Energy Budget-based tumor growth inhibition model for etoposide effects on Wistar rats.*, Pharmaceutical Research

Articles submitted for publication

- **E.M. Tosca**, E. Pesenti, M. Rocchetti, P. Magni. *A population DEB-based model for tumor-in-host growth modulation following anti-angiogenic therapy.*, (Ready to submit)

Contributions to conference proceedings

- **E.M. Tosca**, M. Rocchetti, E. Pesenti, P.Magni, *Modeling resistance development to Bevacizumab in xenograft experiments by coupling hypoxia-mediated mechanism and a Dynamic Energy Budget (DEB) based tumor-in-host model.*, Abstract at ACopP9 2018 (San Diego (CA))

- **E.M. Tosca**, G. De Nicolao, M. Rocchetti, P.Magni, E. Perez, C. Nieto, P. Bettica, J. Moscoso del Prado, *In vitro-in vivo correlation (IVIVC) population modeling for the in silico bioequivalence of a long-acting release formulation of rogesterone.*, PAGE 27 (2018) Abstr 8581 [www.page-meeting.org/?abstract=8581]

- R. Bartolucci, S. M. Lavezzi, **E. M. Tosca**, N. Melillo, S. Grandoni, E. Borella, L. Pasotti, G. De Nicolao, P. Magni. *Evaluation of software tools for Bayesian estimation on population models: an update based on current software versions.*, PAGE 27 (2018) Abstr 8690 [www.page-meeting.org/?abstract=8690]

- **E.M. Tosca**, M. Rocchetti, P. Magni, *A PK/PD model for tumor-in-host growth kinetics following administration of an antiangiogenic agent given alone or in combination regimens.*, PAGE 25 (2017) PAGE 27 (2017) Abstr 7168 [www.page-meeting.org /?abstract=7168]

- **E.M. Tosca**, E. Borella, N. Terranova, M. Rocchetti, P. Magni, *Evaluation of a PK/PD DEB-based model for tumor-in-host growth kinetics under anticancer treatment.*, PAGE 25 (2016) Abstr 5875 [www.page-meeting.org/?abstract=5875]

- E. Borella, L. Carrara, S.M. Lavezzi, I. Massaiu, E. Sauta, **E.M. Tosca**, F. Vitali, S. Zucca, L. Pasotti, G. De Nicolao , P. Magni,

Methods and tools for multiscale modelling in Systems Pharmacology: a review., PAGE 25 (2016) Abstr 5793 [www.page-meeting.org/?abstract=5793]

- **E.M. Tosca**, E. Borella, N. Terranova, M. Rocchetti, P. Magni, *Evaluation of a tumor growth inhibition (TGI) model integrating dynamic energy budget (DEB) theory.*, GNB2016, June 20th-22nd 2016, Naples, Italy

Acknowledgements

My first sincere acknowledgement goes to my advisor, Prof. Paolo Magni, tireless and sleepless worker who hides, behind his joking and unconventional attitude, a rare humanness and extraordinary attention to people. Thanks for the passionate commitment, professionalism and engaging enthusiasm with whom he carries out his everyday work but specially because, trusting in the skills of young people, encourages them to do their best, build self-confidence and overcome their limits.

A very special gratitude goes also to Prof. Giuseppe Denicolao with whom I was lucky enough to work during my PhD. Thanks for all his insightful suggestions, for having always demonstrated a sincere interest in my work, and for always finding time for an advice or a joke.

Further, a special mention to Dr. Maurizio Rocchetti whose creativity and attitude of questioning everything provided the input for all my research activities. Thanks for sharing his wealth of experience always through an on par dialogue and because the 'odi et amo' raised after his endless phone calls enlivened the last three years.

Thanks to all the colleagues and friends of the BMS group: the warmth of shared experiences made our inhospitable lab a place from

that is difficult to leave. In particular, a special mention to the ex and current girls of the death row and to who shared days of different low light.

Finally, I would like to express my infinite gratitude to all my family for their support and encouragement that allowed me to reach this achievement. A special thanks to my parents, Corrado e Giuseppina: with their example they taught me that the way to reach own goals is not based on exceptional capabilities but involves hands, efforts and the concrete commitment in the everyday work.